Investigation on the Electrochemical Performance of the Silicon and Germanium Based Lithium-ion Batteries

硅基与锗基锂离子电池的电化学性能研究

A Thesis Submitted to

University of Liverpool

in Partial Fulfillment of the Requirements for

the Degree of Doctor of Philosophy

in the Department of Electrical Engineering and Electronics

by

Chenguang LIU

BEng Electrical and Electronic Engineering

Xi’an Jiaotong-Liverpool University

& University of Liverpool, 2020

Abstract

Lithium ion batteries (LIBs) have currently dominated the commercial market owing to the environmental benignity, suitable energy density, and long cycle lifetime. The commercial LIBs are commonly using graphite as anode materials, however, it has become clear that the theoretical capacity (~372 mAh g^{-1}) of graphite has nearly reached the bottlenecks with little room for further exploration, and also the energy density and rate performance of existing LIBs are not sufficient for some advanced electronics equipment such as smart watch, and micro implantable biosensor system. With increasing demand and market potential, the worldwide academia researches and industrial community have been focused on investigating anode materials to achieve desirable power density, high rate performance, and long-term stability energy storage system, generating further impetus on flexible electrochemical applications, such as wearable devices, portable electronic devices especially for implant biological equipment. Alternative anode materials such as metal (Si, Ge and Sn) and metal oxide (Co_3O_4, SnO_2 and GeO_2) have been considered. Among them, the Si and germanium oxide have the highest theoretical gravimetric capacity in the elementary substance and oxide-based anode material respectively, which have been proposed as the best candidates for rechargeable battery anode. However, some challenges for these anode materials are also obvious due to the low conductivity and large volume expansion (> 300%) during the usage of LIBs. This expansion problem causes the pulverization of active materials and the repeated formation of the solid electrolyte interface (SEI) on that, resulting in the loss of interparticle electrical contact, and consequently deteriorating the battery cycle lifetime and capacity performance.

In this work, we firstly demonstrated a facile method to fabricate a flexible alloyed copper/silicon core-shell nanoflowers structure anchored on the three-dimensional graphene foam as a current collector. In electrochemical testing, the resulting copper/silicon core-shell nanoflowered electrode demonstrates a high initial capacity of 1869 mAh g^{-1} at 1.6 A g^{-1}, with a high retention rate of 66.6 % after 500 cycles. More importantly, at a high current density of 10 A g^{-1}, this anode remains a high capacity retention > 63% (compared with the highest capacity 679 mAh g^{-1}), offering enormous potential for energy storage applications.

Secondly, we introduced a facile method to synthesize an amorphous GeO_x-coated MXene nanosheet structure as the anode in lithium-ion batteries. For electrochemical performance, this GeO_x/MXene nanosheet exhibited a reversible capacity of 950 mA h g^{-1} at 0.5 A g^{-1} after 100 cycles. It is indicated that the GeO_x/MXene nanosheet structure can significantly improve the stability during the lithiation/delithiation prosses, with the enhanced capacity by the improvement of processes' kinetics.

Thirdly, we built up a facile equipment to measure the high frequency capacitance change of silicon composite electrode. As this high frequency situation, the hypothesis circuit of the coin cell could be seemed as a combination of geometrical capacitance and resistance. For the alloy anodes which exhibited huge volume expanse during the lithiation/delithiation processes, the change of geometrical capacitance could be ascribed to the stress evolution and pulverization effect. Thereby the variation trend of the stress and pulverization could be determined by the change geometrical capacitance change.

To conclude, this project mainly focused on the pulverization and stress effect of the anode materials with alloying lithiation type. The strategies of first and second work were using the nanostructure engineering and 2D materials to release the stress and prevent the pulverization in the electrode. The results from these electrodes exhibited a stable electrochemical performance. Meanwhile, the rate performance of these electrodes was also improved by the additive of highly conductivity materials (e.g., copper, graphene, and MXene). To further investigate the consequence of severe volume expansion, we also built a high-frequency capacitance characterization system to perform the in-situ measurement of stress evolution and pulverization in coin cell with composite Si anode. That demonstrated the expected behavior corresponding to the electrode in the different states of charging.

Key words: Lithium-ion batteries; Silicon anode; Germanium oxide anode; Characterization technique;

摘要：

锂离子电池（LIB）由于其环境友好性，较高的能量密度和稳定的循环寿命，在现今的商业市场中占据主导地位。对于商业的锂离子电池，其通常使用石墨作为负极材料。但是，由于石墨的理论容量（~372 mAh g^{-1}）较低，以石墨做为负极材料的锂离子电池的能量密度已达到瓶颈，几乎没有进一步探索的余地。并且现有的商业锂离子电池性能不足以用于某些先进的电子设备，例如智能手表和微型植入式生物传感器系统。因此世界各地的学术和工业界研究者一直致力于研究新型的负极材料以得到具有理想的功率密度，优秀的倍率性能以及长循环稳定性的电池系统，以进一步推动新型储能系统，特别是柔性电池的发展。最终应用于可穿戴设备，尤其是用于植入生物设备的便携式电子设备。研究者们已经对多种负极材料进行了研究，例如金属（Si，Ge 和 Sn）和金属氧化物（Co_3O_4，SnO_2和 GeO_2）。其中，Si 和氧化锗分别在单质和基于氧化物的负极材料中具有最高的理论重量，被认为是锂离子电池负极的最佳候选材料。然而，因为在嵌锂过程中这些材料会展现出巨大的体积膨胀（> 300%），如何应用这些负极材料也面临一些挑战。巨大的体积膨胀问题会导致活性物质的粉碎，并在表面形成无法嵌锂的固体电解质界面（SEI），进而导致颗粒间电导率的下降，最终造成电池循环寿命和容量性能的下降。

在本文中，我们首先展现了一种简便的方法来制造锚固在三维石墨烯泡沫集流器上的合金化铜/硅核-壳纳米花结构。在电化学测试中，所得的铜/硅核-壳纳米花电极在 1.6 A g^{-1} 的电流密度下达到了 1869 mAh g^{-1} 的高初始容量，并在 500 次循环后仍具有 66.6%的高保持率。更重要的是，在 10 A g^{-1} 的高电流密度下，该负

极仍保持> 63%的高容量保持率，展现了硅基负极应用在锂电池中的巨大潜力。

其次，我们介绍了一种简便的方法来合成无定形 GeOx 附着在 MXene 纳米片上的结构作为锂离子电池的负极。此 GeOx/MXene 纳米片在 0.5 A g^{-1} 的电流密度下，经过 100 次循环后仍显示出 950 mAh g^{-1}的可逆容量。该研究表明，GeOx/MXene 纳米片结构可以显著地改善氧化锗材料在锂化和去锂化过程中的稳定性，最终提高了该负极材料的电化学稳定性。

最后，我们通过搭建一个简便的设备测量了硅复合电极的高频电容变化。在高频情况下，纽扣电池的等效电路可以看作是一个电容和电阻的串联。对于在锂化/脱锂过程中体积变化巨大的负极材料，其几何电容的变化可归因于电极应力的增加和粉化的作用。因此，通过测量电池几何电容的变化，该设备可以被用来确定电极中应力和粉碎的变化趋势。

总而言之，该项目的研究方向主要集中于合金锂化型负极材料的粉碎和应力效应。其中第一和第二项工作的策略是使用纳米结构工程和新型二维材料释放在电极循环中由于体积膨胀造成的应力并防止电极粉化。最终的结果证实这些电极显示出稳定的电化学性能。 同时，通过添加具有高电导率的材料（例如铜，石墨烯和 MXene），进一步改善了这些电极的倍率性能。并且，为了进一步研究体积膨胀带来的严重后果，我们还建立了高频电容表征系统，以对纽扣电池中复合硅电极的应力变化和粉化粉碎状况进行原位测量。其结果成果展示了不同充电状态下纽扣电池中电极的应力和粉碎状况。

关键词：锂离子电池；硅负极；氧化锗负极；表征技术

Acknowledgments

With the four years of Ph.D. study, this is the time to finalize this stage of my life. There has been a number of people who provide the generous help in my project. Without their continuous support and patient guidance, the work demonstrated here would not have been possible.

First of all, I would like to offer my sincere thanks to my supervisor Prof. Ce Zhou Zhao and Dr. Li Yang for their continuous guidance in my doctoral researches. They provided me with so many supports to let me immersed in my research work without any influence. I truly appreciate their advice to my experiment, which gave me a lot of inspiration. Moreover, both of them played a role of mentor in my daily life to giving the advices on my career and future life. It is a great pleasure to work with them.

Also, I would like to thank my other supervisors Dr. Ivona Z. Mitrovic, Prof. Stephen Taylor, and Prof. Paul R. Chalker for their patient instructions when I was an exchange student in the University of Liverpool.

I also appreciated Dr. Sang Lam, Dr. Chun Zhao for sharing their knowledge in my research work, which gave me many ideas to solve the problem in the Ph.D. studies. Moreover, I want to give many thanks to Dr. Yifei Mu, Dr. Qifeng Lu, Dr. Jingjin Wu, and Dr. Ruize Sun for their lots of help and advice in my experiments.

In addition, I would like to thanks to my colleagues: Ms. Yinchao Zhao, Mr. Ruowei Yi, Ms. Yi Sun, Ms. Honghui Yao, Mr. Zitan Chen, Mr. Minxue Gu, Mr. Lingxuan Kong, Ms. Miao Cui, Mr. Yutao Cai, Ms. Yang Wang, Ms. Yanfei Qi, Mr. Jun Liu, Mr. Yuxiao Fang, Mr. Xiangfei Lin, Mr. Xianwei Geng, Mr. Zongjie Shen, Mr. Qihan Liu and Mr. Tianshi Zhao. Their support and assistance gave a lot of happiness to me in these years. It is a great honor to work and life together with them.

Finally, I want offer my profound thanks and my love to my family and my lover Alice for their patience, understand and support.

Chenguang Liu

Jan. 2020

List of Publications

JOURNAL ARTICLES

[1] **Chenguang Liu**, Yinchao Zhao, Ruowei Yi, Yi Sun, Yinqing Li, Li Yang, Ivona Mitrovic, Stephen Taylor, Paul Chalker, and Cezhou Zhao. "Alloyed Cu/Si Core-Shell Nanoflowers on the Three-Dimensional Graphene Foam as an Anode for Lithium-Ion Batteries." *Electrochimica Acta* 306: 45-53 (2019)

[2] **Chenguang Liu**, Yinchao Zhao, Ruowei Yi, Hao Wu, Wenbin Yang, Yinqing Li, Ivona Mitrovic, Stephen Taylor, Paul Chalker, , Li Yang and Cezhou Zhao. "Enhanced Electrochemical Performance by GeOx-Coated MXene Nanosheet Anode with Hydrophilia Lithium Polyacrylate Binder in Lithium-ion Batteries" Electrochimica Acta, Under review.

[3] Yinchao Zhao, **Chenguang Liu**, Ruowei Yi, Ziqian Li, Yanbing Chen, Yinqing Li, Ivona Mitroviz, Stephen Taylor, Paul Chalker, Li Yang, and Cezhou Zhao. "Facile Preparation of Co3O4 Nanoparticles Incorporating with Highly Conductive MXene Nanosheets as High-Performance Anodes for Lithium-Ion Batteries." Electrochimica Acta,345: 136203 (2020)

[4] Yinchao Zhao, **Chenguang Liu**, Yi Sun, Ruowei Yi, Yutao Cai, Yinqing Li, Ivona Mitrovic, Stephen Taylor, Paul Chalker, Li Yang, and Cezhou Zhao. "3D-Structured Multi-Walled Carbon Nanotubes/Copper Nanowires Composite as a Porous Current Collector for the Enhanced Silicon-Based Anode." *Journal of Alloys and Compounds*

803: 505-13 (2019)

[5] Ruowei Yi, **Chenguang Liu**, Yinchao Zhao, Laurence J. Hardwick, Yinqing Li, Xianwei Geng, Qian Zhang, Li Yang, and Cezhou Zhao. "A Light-Weight Free-Standing Graphene Foam-Based Interlayer Towards Improved Li-S Cells." *Electrochimica Acta* 299: 479-88 (2019)

[6] Qian Zhang, **Chenguang Liu**, Shuhui Tao, Ruowei Yi, Weitao Su, Cezhou Zhao, Chun Zhao, Yannick J Dappe, Richard J Nichols, and Li Yang. "Fast and Straightforward Analysis Approach of Charge Transport Data in Single Molecule Junctions." *Nanotechnology* 29: 325701 (2018)

[7] Qi, Yanfei, Ce Zhou Zhao, **Chenguang Liu**, Yuxiao Fang, Jiahuan He, Tian Luo, Li Yang, and Chun Zhao. "Comparisons of Switching Characteristics between Ti/Al_2O_3/Pt and Tin/Al_2O_3/Pt Rram Devices with Various Compliance Currents." *Semiconductor science and technology* 33:45003 (2018).

[8] Yi, Ruowei, Xiangfei Lin, Yinchao Zhao, **Chenguang Liu**, Yinqing Li, Laurence J. Hardwick, Li Yang, Cezhou Zhao, Xianwei Geng, and Qian Zhang. "Fabrication of a Light-Weight Dual-Function Modified Separator Towards High-Performance Lithium-Sulfur Batteries." *ChemElectroChem* 6: 3648-56 (2019)

[9] Geng, Xianwei, Ruowei Yi, Zhiming Yu, Cezhou Zhao, Yinqing Li, Qiuping Wei, **Chenguang Liu**, Yinchao Zhao, Bing Lu, and Li Yang. "Isothermal Sulfur Condensation into Carbon Nanotube/Nitrogen-Doped Graphene Composite for High Performance Lithium–Sulfur Batteries." *Journal of Materials Science: Materials in*

Electronics 29: 10071-81 (2018)

[10] Lu, Qifeng, Yanfei Qi, Ce Zhou Zhao, **Chenguang Liu**, Chun Zhao, Stephen Taylor, and Paul R. Chalker. "Investigation of Anomalous Hysteresis in Mos Devices with ZrO_2 gate Dielectrics." *IEEE Transactions on Device and Materials Reliability* 17, no. 3: 526-30 (2017)

CONFERENCE PROCEEDINGS

[1] **Chenguang Liu**, Yinchao Zhao, Ran Shi, Ruowei Yi, Yi Sun, Li Yang, and CeZhou Zhao. "In-situ measurement of stress evolution and pulverization in a composite silicon electrode by high frequency capacitance characterization (HFCC)" *2nd International Conference on Green Energy and Environment Engineering (CGEEE)*, JUL 02-05, 2019, Okinawa, Japan

[2] Yinchao Zhao, **Chenguang Liu**, Ruowei Yi, Yi Sun, Li Yang, and Ce Zhou Zhao. "3D Copper Sponges-Supported Si Hollow Nanowires as Advanced Anode Materials for Lithium-Ion Battery" *2nd International Conference on Green Energy and Environment Engineering (CGEEE)*, JUL 02-05, 2019, Okinawa, Japan

[3] Yi Sun, **Chenguang Liu**, Yinchao Zhao, Ruowei Yi, Li Yang, and Ce Zhou Zhao. "Graphene oxides mixed in hierarchical porous polyacrylonitrile-based carbons for supercapacitor electrodes" *2nd International Conference on Green Energy and Environment Engineering (CGEEE)*, JUL 02-05, 2019, Okinawa, Japan

[4] Ruowei Yia, Xiangfei Lin, Yinchao Zhao, **Chenguang Liu**, Yinqing Li, Laurence J.

Hardwick, Li Yang, Cezhou Zhao, Xianwei Gengc, and Qian Zhang “A Light-weight Dual-functional Modified Separator via Facile Fabrication towards High Performance Li-S Batteries” *2nd International Conference on Green Energy and Environment Engineering (CGEEE)*, JUL 02-05, 2019, Okinawa, Japan

[5] Yanfei Qi, Chun Zhao, Yuxiao Fang, Qifeng Lu, **Chenguang Liu**, Li Yang, Cezhou Zhao. “Compliance Current Effect on Switching Behavior of Hafnium Oxide based RRAM” *IEEE 24TH INTERNATIONAL SYMPOSIUM ON THE PHYSICAL AND FAILURE ANALYSIS OF INTEGRATED CIRCUITS (IPFA)* JUL 04-07, 2017*,* Chengdu, China

[6] Yanfei Qi, Yuxiao Fang, Chun Zhao, Qifeng Lu, **Chenguang Liu**, Li Yang, Cezhou Zhao. “Influence of HfAlO Composition on Resistance Ratio of RRAM with Ti electrode” *IEEE 24TH INTERNATIONAL SYMPOSIUM ON THE PHYSICAL AND FAILURE ANALYSIS OF INTEGRATED CIRCUITS (IPFA)* JUL 04-07, 2017*,* Chengdu, China

PATENTS

[1] **Chenguang Liu**, Yinchao Zhao, Ruowei Yi, Li Yang, and Ce Zhou Zhao, “Graphene-based nanoflower-shaped silicon-copper alloy electrode material, and preparation method and application”, Patent Application No.: CN 109599534 A

[2] **Chenguang Liu**, Yinchao Zhao, Ruowei Yi, Li Yang, and Ce Zhou Zhao, “Lithium ion battery electrode stress in-situ measurement system”, Patent Application No.: CN

109671996 A

[3] **Chenguang Liu**, Minxue Gu, Yinchao Zhao, Ruowei Yi, Li Yang, and Ce Zhou Zhao, "Self-assembly-based graphene-silicon composite electrode material and preparation method", Patent Application No.: CN 108023070 A

[4] Yinchao Zhao, **Chenguang Liu**, Liquan Pi, Ruowei Yi, Li Yang, and Ce Zhou Zhao, "Preparation method for copper-silicon compound cathode piece, and application", Patent Application No.: CN 109560256 A

[5] Yinchao Zhao, **Chenguang Liu**, Haowei Song, Ruowei Yi, Li Yang, and Ce Zhou Zhao, "Preparation method and application of copper carbon silicon composite negative electrode plate", Patent Application No.: CN 109638224 A

[6] Yinchao Zhao, Zitan Chen, **Chenguang Liu**, Ruowei Yi, Li Yang, and Ce Zhou Zhao, "Wrapped silicon negative electrode material and preparation method", Patent Application No.: CN 108039461 A

[7] Ruowei Yi, Li Yang, Ce Zhou Zhao, Yinchao Zhao, **Chenguang Liu**, and Xianwei Geng, "Three-dimensional dendritic nitrogen-doped graphene nanotube and preparation method", Patent Application No.:CN 108039460 A

[8] Yudan Yuan, Ruowei Yi, Jiaqi Li, Yi Sun, Yinchao Zhao, **Chenguang Liu**, Wei Sun, Chun Zhao, Li Yang, and Ce Zhou Zhao, "Preparation method of polyacrylonitrile/molybdenum disulfide composite material applied to super capacitor", Patent Application No.: CN 108305789 A

[9] Li Yang, Ce Zhou Zhao, Ruowei Yi, **Chenguang Liu**, Yinchao Zhao, and Xianwei

Geng, “Positive electrode material of one-dimensional sulfur-conductive high polymer lithium-sulfur battery and preparation method”, Patent Application No.: CN 107863523 A

[10] Ruowei Yi, Li Yang, Ce Zhou Zhao, **Chenguang Liu**, Yinchao Zhao, and Xianwei Geng, “Lithium-sulfur battery taking nitrogen-doped foamy graphene sheet as middle layer, and preparation method”, Patent Application No.: CN 107887557 A

[11] Ruowei Yi, Li Yang, Ce Zhou Zhao, **Chenguang Liu**, Yinchao Zhao, and Xianwei Geng, “Method for manufacturing intermediate layer of conductive high polymer compound for lithium-sulfur batteries”, Patent Application No.: CN 108039462 A

[12] Ruowei Yi, Li Yang, Ce Zhou Zhao, Yudan Yuan, **Chenguang Liu**, Yinchao Zhao, and Xiangfei Lin, “Composite cathode sheet for lithium-sulfur battery and preparation method, and application”, Patent Application No.: CN 109671907 A

[13] Ruowei Yi, Li Yang, Ce Zhou Zhao, Yudan Yuan, **Chenguang Liu**, Yinchao Zhao, Xianwei Geng, and Xiangfei Lin, “Composite diaphragm for lithium-sulfur battery and preparation method and application”, Patent Application No.: CN 109686902 A

List of Figure

List of Tables

List of Acronyms

Term	**Initial components of the term**
LIBs	Li-ion batteries
Ni-Cd	Nickel-cadmium
Ni-MH	Nickel-metal hybrid
EVs	Electric vehicles
HEV	Hybrid electric vehicles
LCO	$LiCoO_2$
NMC	$LiNi_xMn_yCo_zO_2$,
NCA	$LiNi_{1-y-z}Co_yAl_zO_2$
LMO	$LiMn_2O_4$
EC	Ethylene carbonate
SEI	Solid electrolyte interface
XRD	X-ray diffraction
MPs	Microparticles
NPs	Nanoparticles
NWs	Nanowires
a-Si	Amorphous Si
NCs	Nanocones
ICPCVD	Inductively coupled plasma
RGO	Reduce graphene oxide
PS	Polystyrene
CVD	Chemical vapor deposition

2D	Two-dimensional
SEM	Scanning electron microscopy
TEM	Transmission electron microscopy
NMR	Nuclear magnetic resonance
AFM	Atomic-force microscopy
SE	Secondary electrons
BSE	backscattered electrons
AES	Auger electron spectroscopy
EDAX	Energy dispersive analysis of X-ray
OM	Optical microscope
3DGF	Three-dimensional Graphene Foam
APCVD	Ambient-pressure chemical vapor deposition
3D	Three-dimensional
FWHM	Full width at half maximum
NFs	Nanoflowers
PECVD	Plasma enhanced chemical vapor deposition
DMC	Dimethyl carbonate
CV	Cyclic voltammetry
EDS	Energy Dispersive Spectrometer
PVDF	Polyvinylidene fluoride
Li-PAA	Lithium polyacrylate
DI	De-ionized
NMP	N-methyl pyrrolidinone

PVP	Polyvinyl Pyrrolidone
XPS	X-ray photoelectron spectroscopy
TG	Thermogravimetric
SSA	Specific surface area
BET	Brunauer–Emmett–Telle
HFCC	High frequency capacitance characterization
PP	Polypropylene
PE	Polyethylene
CMC	Carboxymethylcellulose
SBR	Styrene butadiene rubber
BTS	Battery test system

Table of Contents

Chapter 1: Literature Review

1.1 Lithium-ion Batteries

Since the first battery (Volta's cell) was invented in 1800, the electrical storage devices have been widely investigated with the development of electrical and electronics technologies. As time goes on, many different types of batteries were invented and applied to fast and safety storage the electrical energy, include lead-acid, nickel-cadmium (Ni-Cd), nickel-metal hybrid (Ni-MH), Li metal, and Li-ion batteries (LIBs). The lead-acid battery is the first practical rechargeable battery (secondary battery), which has been widely used in many fields in last decades. Moreover, the lead-acid batteries are still extensively used for electrical storage in the 12V automotive electrical system. But the energy density of lead-acid battery is too low to be used in the portable electrical devices. **Figure 1.1** displays the structure of the lead-acid battery.

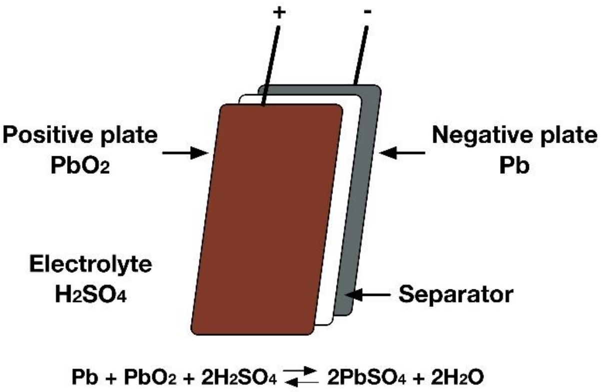

Figure 1.1 Schematic diagram of a lead-acid battery.

Therefore, after the invention of lead-acid batteries, there are more advanced secondary battery have been development and application, such as nickel-cadmium battery (1899) and NiMH battery (mid-1980s).[1] These batteries have been widely used in most of consumer devices, especially for portable electrical equipment, such as electric shavers, personal stereo, etc., because these batteries exhibit higher energy density (compare with lead-acid batteries). However, there are also many drawbacks for these two types of batteries. For Ni-Cd batteries, firstly, the toxicity of cadmium cannot be ignored when it extensively applied in the electrical devices. Secondly, the unstable cycle life and memory effect of Ni-Cd battery cannot sustain the life span of electrical devices. Ni-MH battery solved the memory effect and cycle life problem to some extent, but it did not achieve a remarkable energy density. The structure schematic diagram of Ni-Cd and Ni-MH battery was shown in **Figure 1.2**.

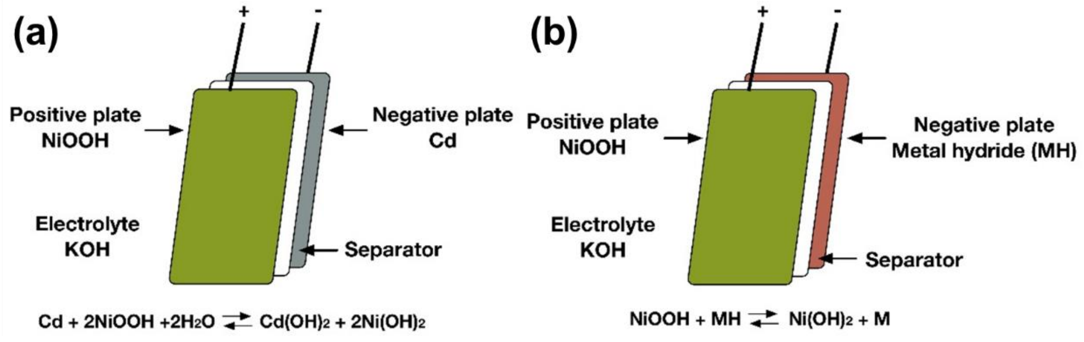

Figure 1.2 (a) Schematic diagram of a Ni-Cd battery. (b) Schematic diagram representation of a Ni-MH battery.

With the advent of electrical technology, peoples need the battery can exhibit high energy density and long cycle life to satisfy the power requirement of advanced electric equipment. The researches of lithium battery have begun from 1950s, these preliminary works confirmed that Li-metal could be stable in a series of nonaqueous electrolytes such as liquid SO_2, fused salts, and organic solution.[2] In 1970s, the researchers in Stanford University investigated the modification of electrical conductivity for materials by using different intercalating ions.[3] This work intended to improve the conductivity especially superconductivity of materials by a simple intercalation of electrons into the lattice. However, this research also discovered the intercalation reaction could absorb considerable energy, which is a potential role for energy storage. Based on these work, the research and development of lithium batteries has been witnessing rapid development after 1970s.[4, 5] In 1991, Sony marketed the first commercial LIBs, which used the transition metal oxides such as CoO_2, NiO_2, and MnO_2 as cathode. The anode consists of various carbon-based materials such as graphite.[6] The two electrodes were separated by a microporous polyolefin separator, which could make the Li-ion safety intercalated and deintercalated between cathode and anode.[7] This Li-ion battery finally demonstrated high energy density, stability cycle life and unparalleled security. Moreover, these intercalation reactions are still used at both electrodes for most of commercial secondary lithium batteries until today. **Figure 1.3** demonstrated the structure of the LIBs with the $LiCoO_2$ cathode and graphite anode.

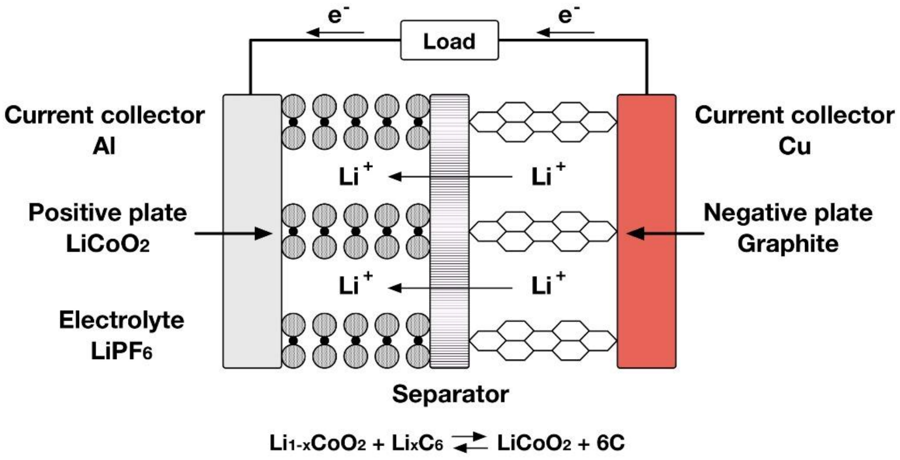

Figure 1.3 Schematic of lithium-ion battery (LIBs). Anode (graphite) and Cathode ($LiCoO_2$) were separated by a polymer separator in a non-aqueous liquid electrolyte.

From the first commercialization of LIBs, this technology has become the dominant electric power source for portable and mobile devices (e.g., music player, cell phone, digital cameras, laptops, etc.), which is because of the high capacity density of LIBs. Compared with conventional batteries, the LIBs could store more than three times of energy per unit weight and volume. **Figure 1.4** display the comparison of the different battery technologies versus gravimetric and volumetric energy density.

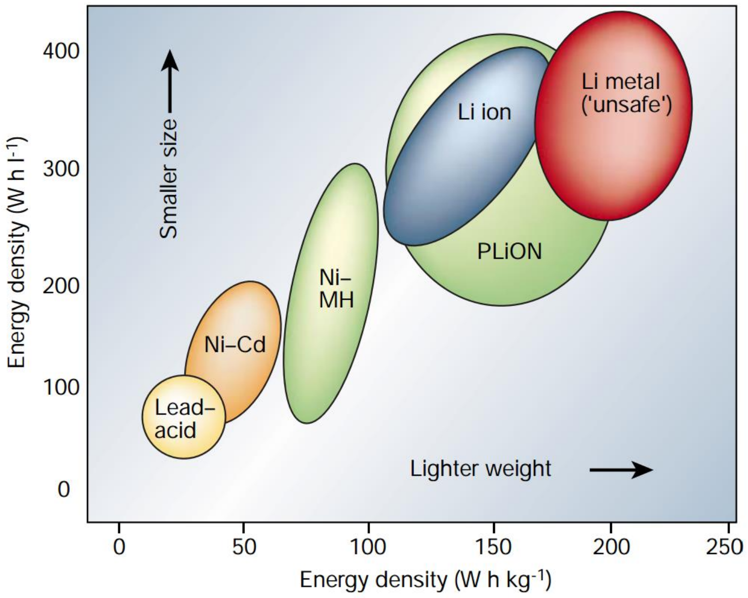

Figure 1.4 Comparison of the different battery technologies versus gravimetric and volumetric energy density.[8]

The LIBs have led to the growth of the market of the energy storage system due to its high capability to store the energy. **Figure 1.5** shown the tendency of the LIBs sale in the consumer market. It shows the market of LIBs has an enormous growth in recent 20 years. The first explosive growth of LIBs was between 2005 and 2015, which is because of the rapid development of portable electric devices, such as cell phones, laptops, music players and others. From 2010, the rapid growth of the market and technologies of electric vehicles (EVs) have been started. Because the power requirements of EVs are much larger than the portable devices, the manufacturers need to provide more LIBs to satisfy these requirements. Moreover, the improvements of energy density and other performance for current commercial LIBs are also urgent.

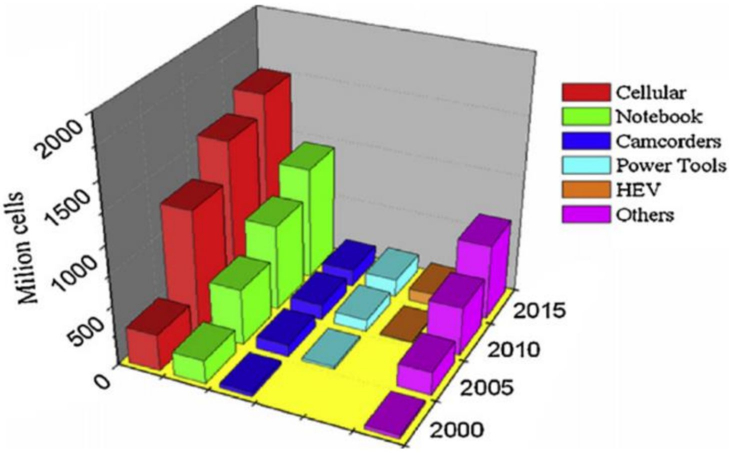

Figure 1.5 Tendency of the LIBs sale in the consumer electronic and hybrid electric vehicles (HEV) market.[9]

1.1.1 Cathode Materials

As an indispensable part in Li-ion batteries, the cathode materials have been widely investigated over 40 years. Based on the intercalation complexes research at Stanford University in 1971,[3] Whittingham confirm the lithium could be intercalated in TiS_2 for high-energy batteries by using the TiS_2 as the cathode in 1976.[4, 10] Following his research, Goodenough et al. established a new transition metal oxide $LiCoO_2$ cathode for batteries with high energy density.[11] The Li-ion demonstrated stable and fast intercalation and deintercalation in this material. After that, his discovery was followed by Sony that marketed the first lithium-ion batteries. Moreover, these researches have excited a broad investigation to find the novel cathode materials for high voltage batteries.[12, 13] These cathode materials mainly consist of two categories, which are cathode materials with two-dimensional structure and three-dimensional structure (**Table 1.1** and **Table 1.2**).[14]

Table 1.1 The electrochemical properties of cathode materials with two-dimensional structure. [14]

Compound	First discharge capacity (mAh g^{-1})	Average voltage (V vs. Li)	Li uptake	Energy density (Wh kg^{-1})
$Li_xV_2O_5$	420	2.25	3.0	923
$Li_{1+x}V_3O_8$	308	2.50	4.0	770
Li_xMoO_3	250	2.30	1.5	575
$Li_{1-x}CoO_2$	140	3.70	0.5	520
$Li_{1-x}NiO_2$	160	3.80	0.5	530
$Li_{1-x}Ni_{0.70}Co_{0.30}O_2$	180	3.75	0.6	675
$Li_{1-x}Ni_{0.80}Co_{0.15}Al_{0.05}O_2$	120	3.60	0.8	400
$Li_{1-x}Ni_{1/3}Mn_{1/3}Co_{1/3}O_2$	170	3.30	1.0	560
$Li_{1.2}Ni_{0.2}Mn_{0.6}O_2$	178	3.50	1.0	623
$Li_{1.17}Mn_{0.33}Co_{0.5}O_2$	254	3.50	1.0	889
$Li_{1.17}Ni_{0.125}Mn_{0.33}Co_{0.375}O_2$	265	3.50	1.0	927

Table 1.2 The electrochemical properties of cathode materials with three-dimensional structure. [14]

Compound	Practical capacity (mAh g^{-1})	Average voltage (V vs. Li)	Reversible Li$^+$ per M atom	Energy density (Wh kg^{-1})
Li_xVO_2	290	2.6	0.9	750
$Li_{1-x}Mn_2O_4$	120	3.8	0.4	455
$Li_xNa_yMnO_zI_\eta$ (amorphous)	275	2.6	1.5	715
$Li_{1-x}CoO_2$	140	3.7	0.5	520
$Li_{1-x}MnCoO_2$	125	4.8	0.4	600
$Li_{1-x}NiO_2$	140	3.8	0.5	675
$Li_{1-x}Ni_{0.85}Co_{0.15}O_2$	180	3.75	0.6	675
$Li_{1-x}Fe_2(SO_4)$	110	3.6	0.8	400
Li_xFePO_4	170	3.3	1.0	560

In these cathode materials, the nickel-based compounds $Li_{1-x}MnCoO_2$ (NMC) and $LiNi_{1-x}Co_yAl_zO_2$ (NCA), lithium cobalt oxide, lithium iron phosphate, and lithium manganate have been chosen for most potential materials for commercial Li-ion batteries. The energy, safety, cost, life, and power performance of these materials was plotted in **Figure 1.6**.

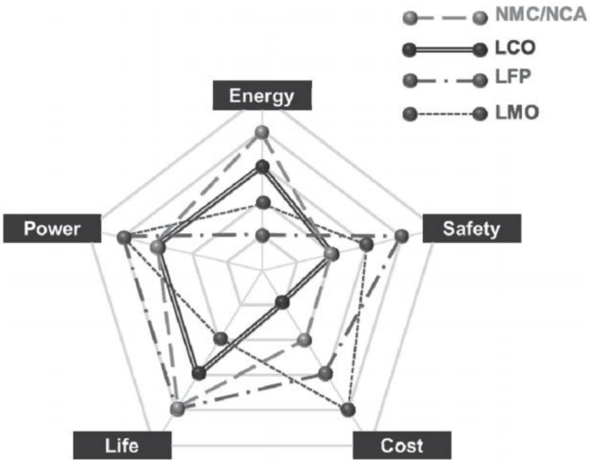

Figure 1.6 Five performance as measures to evaluate cathode materials. LCO= $LiCoO_2$, layered, NMC= $LiNi_xMn_yCo_zO_2$, layered, NCA= $LiNi_{1-y-z}Co_yAl_zO_2$, layered, LMO= $LiMn_2O_4$, spinel. LFP=$LiFePO_4$, olivine.[15]

1.1.2 Anode Materials

In 1970s, the researches had started the investigation of lithium intercalation in graphite and other carbons, which confirmed the graphite could be lithiated to LiC_6.[16] However, because of the strong reaction of lithium with the electrolyte, the early attempts to use the graphite as anode materials for Li-ion intercalation and deintercalation failed.[17, 18] In 1983, Yazami et al. were successfully achieved a reversible graphite negative electrode for lithium intercalation, but it needs to be performed with solid organ electrolyte (polyethylene oxide with lithium perchlorate) and high temperature (120 deg).[19] After the claim from Sony, the researchers confirmed the crystalline carbon materials could be stable intercalation and deintercalation by using the suitable solvent of electrolyte which is mainly based on the ethylene carbonate (EC).[20-22] Finally, in 1991, Sony market the rechargeable Li-ion batteries by using the graphite as anode. Which could make the Li-ion safety intercalated and deintercalated between $LiCoO_2$ cathode and graphite anode.

The ideal anode materials in LIBs should satisfy the following requirements, (1) this material need to store the Li-ion as much as possible with the low volume density to increase the gravimetric capacity density; (2) the ion and electrical conductivity of this materials need be large to motivate the fast transfer of Li-ion and electron; (3) the redox potential versus Li^+ of it need to be small for any number of Li insertion, which is because the overall voltage of LIBs is the subtract this potential from the redox potential of cathode material, so the smaller redox potential of anode material means the larger overall energy density of LIBs; (4) this material must not react with lithium salt and not soluble in the electrolyte; (5) the quantity of this material element need to large with environmentally friendly; (6) the reaction between this material with Li-ion must be safe without any unstable phenomenon such as thermal runaway of the battery. There are many anode materials have been discussed for LIBs, include elementary substance (e.g., Li, Si, Ge, Sn, Sb, Al, Mg, Bi, etc.) and oxide-based materials (e.g., TiO_2, $Li_4Ti_5O_{12}$, SiO_2, GeO_2, SnO_2, CuO, MnO, Co_3O_4, etc.).

For the elementary substance anode materials (**Table 1.3**), the silicon has been chosen for most potential anode material, which is the second most abundant element in the earth's crust and the eight most comment elements in the earth by mass. Moreover, it owns the highest gravimetric capacity (9786 mAh cm^{-3}) and low Li-insertion potential (0.4V), thus the energy density of that is very large when to use it as anode materials in LIBs. However, there are still many challenges need to be solved for silicon anode. Firstly, the electron and ion conductivity of silicon are relatively low, leading to the low practical capacity, especially when using high current density for charging and discharging in LIBs. Secondly, the huge volume change (320%) from Si to $Li_{4.4}Si$ could cause the severe pulverization of silicon during the lithiation. This pulverization not only reduces the interconnected of silicon particles but also leads to the continuous generation of solid electrolyte interface (SEI) film that cannot contribute the capacity in further lithiation, finally leads to the rapid capacity fading in the cycles of LIBs. Thirdly, the elemental silicon is too stable to modify its morphology and structure except oxidation or other combination, which makes the modification and optimization of silicon hard, but the silicon also improves the stability of the electrode in electrolyte. It likes a double-edged sword for LIBs. Hence, the researchers need to investigate the modification of silicon anode to improve the performance of that in LIBs, but they also need to retain the stability of the silicon in the electrolyte.

Table 1.3 The electrochemical properties of elementary substance anode materials.

Materials	Li	C	Si	Ge	Sn	Sb	Al	Mg	Bi
Density(gcm^{-3})	0.53	2.25	2.33	5.35	7.29	6.7	2.7	1.3	9.78
Lithiated phase	Li	LiC_6	$Li_{4.4}Si$	$Li_{4.4}Ge$	$Li_{4.4}Sn$	Li_3Sb	LiAl	Li_3Mg	Li_3Bi
Theoretical specific capacity (mAhg^{-1})	3862	372	4200	1600	994	660	993	3350	385
Theoretical gravimetric capacity (mAh cm^{-3})	2047	837	9786	7367	7246	4422	2681	4355	3765
Volume change (%)	100	12	320	>300	260	200	96	100	215
Potential vs. Li(~V)	0	0.05	0.4	0.35	0.6	0.9	0.3	0.1	0.8

For the oxide-based materials (**Table 1.4**), germanium oxide exhibits the highest gravimetric capacity (6975 mAh cm^{-3}), which is based on the reversible capacity of Ge to $Li_{4.2}Ge$. The lithiation of the germanium oxide could be described by two steps reaction [7]:

$$GeO_2 + 4Li^+ + 4e^- \rightarrow Ge + Li_2O \tag{1.1}$$

$$Ge + 4.2Li + 4.2e^- \longleftrightarrow Li_{4.2}Ge \tag{1.2}$$

Because of the low electrical and ion conductivity, the production of Li_2O in first reaction step is hardly reversible, therefore, just the second step could be considered as the reversible reaction in the cycles of LIBs. However, in this situation, the second step could still contribute the reversible specific capacity of 1125 mAh g^{-1}, which shows the potential of the germanium oxide material. Unfortunately, same as silicon, the germanium also has a huge volume expanse when it is lithiated from Ge to $Li_{4.2}Ge$, which could cause the severe pulverization, finally leading to the rapid fading of capacity during the cycling in LIBs. Therefore, the solution of the problem in germanium oxide anode material is mainly focused on the nano-engineering of the structure for germanium oxide materials. A well-designed nanostructure not only effectively preventsthe pulverization of materials, but also increases the reversible capacity of the whole germanium oxide-based anode.

Table 1.4 The electrochemical properties of oxide-based anode materials.

Materials	**TiO_2**	**$Li_4Ti_5O_{12}$**	**SiO_2**	**GeO_2**	**SnO_2**	**CuO**	**MnO**	**Co_3O_4**
Density(gcm^{-3})	4.2	3.5	2.6	6.2	6.4	6.6	5.4	6.1
Reaction type	Intercalation/ Deintercalation		Alloying/De-alloying			Conversion		
Theoretical specific capacity (mAh g^{-1})	335	175	1961	1125	875	375	755	890
Theoretical gravimetric capacity ($mAhcm^{-3}$)	1407	613	5099	6975	5600	2475	4077	5429
Volume change	Small		Large			Large		

1.2 Alloyed Anode Materials

As shown in **Table 1.3** and **Table 1.4**, the Si and GeO_2 demonstrate highest theoretical gravimetric capacity in the elementary substance and oxide-based anode materials, respectively. However, both materials exhibit large volume change (>300%) due to the alloying reaction during the lithiation. The huge volume expanse leads to the severe pulverization of the materials, which breaks the interconnection between each particle in electrode. Finally, the rapid capacity fading would occur during the cycling of batteries. The pulverization effect is a critical problem in these anode materials. Therefore, the approaches to determinate and relieve this effect would be discussed and investigated in the following section.

1.2.1 Silicon Based Materials

The lithiation of Si materials have been investigated from 1980s. [23-26] These researches have shown the lithiation of Si at specific temperatures follow the binary phase diagram of equilibrium Li-Si alloy, which consists of a series intermetallic compounds such as $Li_{12}Si_7$, Li_7Si_3, $Li_{13}Si_4$, and $Li_{22}Si_5$. This lithiation process demonstrates the distinct plateau of voltage for each Li-Si alloy phase. However, for the Si anode in LIBs at room temperature, the firstly discharge plateau is contrary to the equilibrium phase diagram at high temperature, which only demonstrates one plateau around 0.1V corresponding to the phase change of Si. This is because the phase change of crystalline Si in the first lithiation is different from further lithiation processed. Typical discharge and charge curves of the microparticles Si anodes at room temperature was shown in **Figure 1.7**. The mechanism of electrochemical lithiation of Si at room temperature was investigated in 2004.[27, 28] The ex situ and in situ X-ray diffraction of the Si in different lithiation state demonstrated the reaction mechanism of Si as follows.[27-29]

Lithiation:

$$\text{Si (crystalline)} + x\text{Li}^+ + x\text{e}^- \rightarrow \text{Li}_x\text{Si (amorphous)} + (3.75 - x)\text{Li}^+ + (3.75 - x)\text{e}^- \tag{1.3}$$

$$\text{Li}_{15}\text{Si}_4\text{(crystalline)} \tag{1.4}$$

Delithiation:

$$\text{Li}_{15}\text{Si}_4\text{(crystalline)} \rightarrow \text{Si (amorphous)} + y\text{Li}^+ + y\text{e}^- + \text{Li}_{15}\text{Si}_4\text{(residual)} \tag{1.5}$$

In this reaction, the pristine crystalline Si transfers to the amorphous Li-Si alloy and finally form the crystalline $Li_{15}Si_4$ (1.3) at room temperature. For the delithiation of Si, the final product is the amorphous Si for two-phase transfer (1.4). The generated amorphous Si is different from the pristine crystalline Si, which causes the change of plateau in the further lithiation processes. The residual $Li_{15}Si_4$ is due to the electrical disconnection of Si when the volume expanse of that, and this residual $Li_{15}Si_4$ finally leads to the large capacity fading in the further cycling. After the first lithiation and delithiation of Si, the reaction (1.4) and (1.5) are repeated with the fading of reversible capacity.

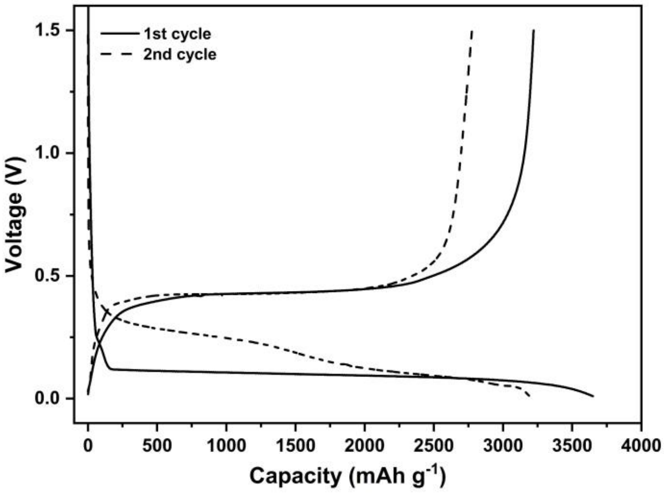

Figure 1.7 The discharge and charge curves of microparticles Si powder anode for the 1st and 2nd cycles.

For the capacity fading of Si anode in LIBs, the researchers investigated the failure mechanism in the cycling of Si microparticles anode[30]. This fading of reversible capacity is mainly caused by the decrease of the connection between carbon conductive additive with Si particles, which significantly increases the internal resistance of whole electrode. The loss of connection is due to the huge volume change during the Li-Si alloying processes that lead to the severe pulverization of Si microparticles. The researchers also demonstrated this problem could be relieved by increasing the amount of conductive additive materials or applying the pressure of whole electrode, but it is still a serious problem of Si anode. Moreover, the cracked Si particles also lead to the formation of more SEI films, which cannot be insertion by lithium ions, which finally leads to further loss of capacity. **Figure 1.8** shown the failure mechanism of Si anode.

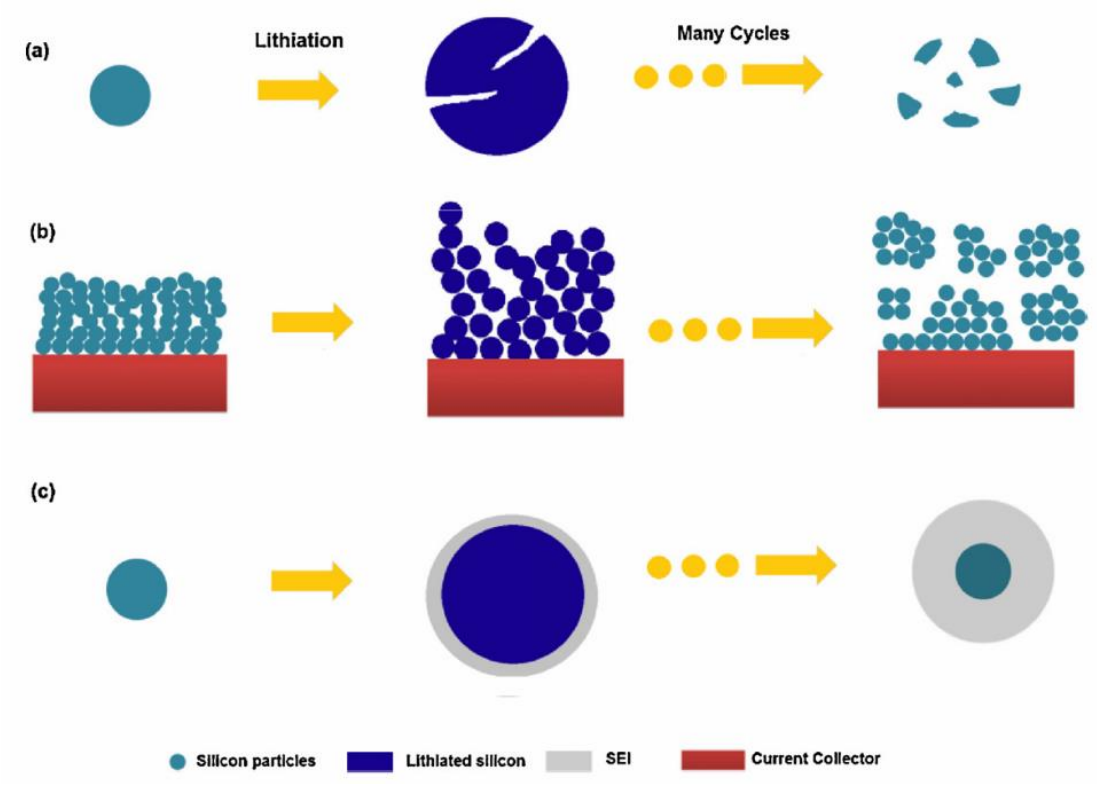

Figure 1.8 Si electrode failure mechanisms: (a) material pulverization. (b) Morphology and volume change of the entire Si electrode. (c) Continuous SEI growth.[31]

To tackle these problems, numerous researches have been focused on the novel design of electrode structures including thin films [32], microparticles (MPs)[33], nanoparticles (NPs) [34-37], nanowires (NWs) [38-40], and other composite structures [41-43]. Among them, depositing Si thin film on nanowires or nanoparticles substrates to form the hollow core-shell structure has been reported to be an effective way to release the strain caused by volume change during the lithiation [44-47]. Wang et al. used the highly cross-linked Cu NWs foams as templates, coated with a high quality amorphous Si (a-Si) thin film to achieve Cu/a-Si core-shell NWs, demonstrating an extremely electrical conductivity for the whole electrode and revealing ultra-long cycle life and high performance rate when used in LIBs [44]. Li et al. reported a scalable method to obtain the crystalline Ni_3Si_2 nanocones (NCs) and NWs on nickel foam as a template. a-Si was then in situ coated on this template via an inductively coupled plasma (ICPCVD). The achieved electrode demonstrated good electrical conductivity and mechanical stability of this combination of the metallic core with the a-Si shell [48]. These examples confirmed the nanostructure metallic supporting core can provide a mechanically stable anchoring basis for Si film, which is helpful for the improvement of cycling performance.

1.2.2 Germanium Oxide-based Materials

In recent years, research efforts have significantly expanded the choices of anode materials other than the current commercial graphite due to theoretical capacity of 372 mAh g^{-1} hardly satisfies the requirements of advanced high-performance LIBs[49]. The germanium oxide has been considered as a promising candidate for the novel anode materials[50].

However, germanium oxide behaves similar to tin and silicon, suffering the tremendous volume expansion (370% for the full lithiation of Ge) and low conductivity during the discharge and charge of LIBs[51]. These problems cause the pulverization of Ge-based anode and the formation of the SEI on the material surface, subsequently leading to the rapid capacity fading and the loss of interparticle electrical contact.

To date, various of approaches have been reported to tackle these issues, consisting of mainly improved morphologies design (nanoparticles[52], nanowires[53], nanoribbons[54], nanotubes[55] and porous structures[56]), metal doped germanium oxide[57-60], two-dimensional (2D) materials enhanced germanium oxide[61-63], GeO_X nanoparticle[64] and GeO_X-based composite[65, 66]. In particular, the GeO_X-based composite and 2D materials have demonstrated enormous potential and resulted in an increase of the rate performance and cycling stability in LIBs. Wang et al. was first synthesized the hierarchical porous GeOx as the anode, using GeO_3^{2-} as the precursor, $NaBH_4$ as the reducing agent, and demonstrated outstanding cycling stability when used in LIBs.[64] After that, this GeO_X was combined with reduced graphene oxide (RGO) by Lv et al., demonstrateing another method to improve the electrical conductivity and rate performance for LIBs.[65] Based on these researches, Choi et al. applied the polystyrene (PS) nanobeads as sacrificial templates and fabricated a sandwich structure of GeO_X coated on RGO balls for LIBs, with the hope to provide the short pathway for Li-ion diffusion, resulting in excellent long-term cycling performance with high reversible capacities.[66] These examples confirmed that the composition of GeOx materials with 2D materials such as RGO is a feasible pathway to achieve stable electrochemical properties and exceptional rate performance in LIBs.

1.3 Objectives of Thesis

In the previous section, the approaches to relieve the pulverization and stress effect in the alloy anode materials have been discussed, which demonstrated a variety of methods to improve the electrochemical performance of anode materials in LIBs. Based on these researches, three approaches have been inspired to relieve and determinate the stress and pulverization effect of alloy anode in the LIBs. The realization of these ideas was the objectives of this project, which would be further discussed in following section.

1.3.1 The Application of Graphene in the Silicon Anode

As a single atomic layer of carbon hexagons, graphene has been widely explored owing to its unique structure and fascinating properties. Due to its large specific surface area (2630 m^2 g^{-1})[67], excellent electric conductivity (~15000 cm^2 $V^{-1}S^{-1}$ at 300K)[68], high thermal conductivity (~3000 W Mk^{-1}, room temperature)[69], and planar sp^2-hybridized carbon hexagons framework, graphene is a potential choice as a matrix to support active materials. Moreover, graphene itself exhibits a high capacity with initial discharge and charge capacities of 1059 mAh g^{-1} and 732 mAh g^{-1}[70], which is more than 2 times of theoretical capacity of commercial graphite. However, its theoretical energy capacity is still less than silicon (4200 $mAhg^{-1}$). So, it should act as a capsule or support framework in silicon anode to fix the main problem (Large volume change) of silicon.

There are some preliminary investigation about graphene-containing nanomaterials showing long cycle life, great electrical conductivity, and low columbic efficiency[71]. In general, the structures supported by graphene can be classified into six different models as summarized by Raccichini et al.[71] (**Figure 1.9**).

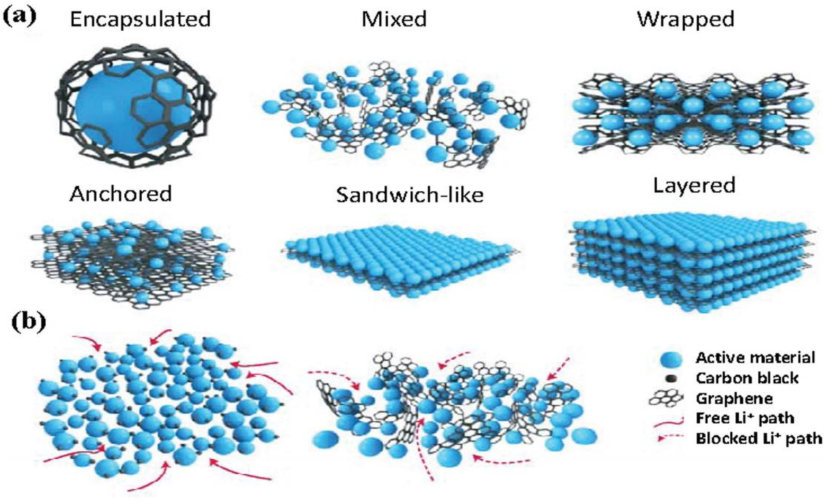

Figure 1.9 Structural models and a possible drawback of graphene composites.[71]

In these structural models, graphene acts as a support for electroactive nanomaterials. It also protects nanomaterials from stacking, because the van dew Waals interactions between the graphene layers is low. Moreover, the excellent electrical and mechanical properties of graphene could improve the electrical conductivity of the whole electrode and retard the volume expansion of electrode materials during cycling.

More recently, a graphene-based flexible current collector has been considered as an alternative for the current collector [72, 73]. The unique structural and electronic characteristics of graphene make it attractive for LIBs applications, offering the fast electron and ion transport path for the whole electrode in the energy storage system.

Such 3D graphene interconnected network can be synthesized with a template of metallic foam by the hydrothermal method, layer-by-layer assembly, or chemical vapor deposition (CVD) method [74-77]. For instance, Chen et al. deposited a 3D flexible and conductive interconnected graphene foam by CVD method in which the nickel foam and methane (CH_4) act as a template and carbon source [77]. The monolayer graphene produced by the CVD method has excellent quality and conductivity rather than other chemical methods. Following this work, many researches have been reported to use the 3D graphene foam as the current collector to develop flexible electrode with excellent conductivity for advanced energy storage systems such as LIBs, supercapacitors, and fuel cell [78-80]. Li et al. directly deposited the Si films on the flexible free-standing graphene foam and used that as high capacity anodes for LIBs [81]. Their results showed that this flexible structure could relax the strain of the Si during the volume expansion.

Therefore, in Chapter 3, an alloyed Cu/Si core-shell nanoflowers on the three-dimensional graphene foam was developed, which demonstrates the outstanding electrochemical performance by employed the graphene foam as the current collector.

1.3.2 Enhanced the Electrochemical Performance of GeOx Anode by MXene Nanosheet

As a novel member of 2D materials family, MXene combined the advantage of highly electrical conductivity of graphene and extremely hydrophilia of graphene oxide.[82, 83] It could be considered as a potential candidate to be applied in GeO_X anode. The MXene $Ti_3C_2T_X$ (T indexed to the terminal groups such as -OH, -O, and -F) could be facilely achieved with the two-dimension (2D) layered structure by using LiF + HCl to exfoliate layered carbides with MAX phases.[84, 85]. During the Li-ions interaction/de-interaction process, the MXene shows the ignorable volume change and low Li-ion diffusion barrier.[86, 87] It provides a stable mechanical capacity and convenient interaction channel to support the electrochemical stability when combining with other materials. Thus, the MXene has been used in many energy storage fields such as LIBs and supercapacitors[88-90]. However, the use of joint MXene and the GeOx as the LIBs anode has not yet found in the literature. Thereby, Chapter 4 introduced an amorphous GeO_x-coated MXene nanosheet structure as the anode, which demonstrated an excellent rate performance and a stable cycling capacity in LIBs.

1.3.3 Stress Evolution and Pulverization in the Silicon Anode

Si is one of potential anode materials for next-generation Li-ion batteries, which has highest theoretical specific capacity with maximum value of 4200mAh g^{-1} (corresponding to $Li_{4.4}Si$). Meanwhile, the silicon is the second most abundant element in the earth resulting to incomparable environmental friendliness. However, Si would lead to much larger volumetric expansion upon fully lithiation (300% for Si, ~12% for graphite), which could cause the significant stress inside anode, resulting in the pulverization of Si then loss of interparticle electrical contact. Moreover, this problem would make the cracked Si expose to electrolyte again and regeneration of new SEI film on Si, finally reduce the lifetime of batteries. Hence, observation and measurement of stress effect and mechanical properties change of Si-base electrodes during electrochemical cycling are effective ways to investigate and understand of electrodes for future LIB applications.

The common strategies to observe these dynamic changes in the electrode are to introduce various in-situ measurement techniques for electrode characterization, including optical microscopy,[91] scanning electron microscopy (SEM),[92] transmission electron microscopy (TEM),[93] X-ray diffraction (XRD),[94, 95] Raman spectroscopy,[96] nuclear magnetic resonance (NMR)[97] and atomic-force microscopy (AFM).[98] These measurement techniques usually use high-precision instruments with a novel method to capture the atomic level dynamic changes during the electrochemical cycling. For example, Jian Yu Huang and co-workers [93](In situ atomic-scale imaging of electrochemical lithiation in silicon) first used in situ TEM to understand the Li-Si alloying reaction at the nanoscale. Then this method has been developed by many researchers, which reveals many features during the alloying reaction, including phase change, atomic level expansion, pulverization behavior, and the stress effect on the mechanical of the electrode. These studies inspired the more fundamental investigation of the dynamic lithiation process. Moreover, there are few researchers focusing on the measurement of the composite silicon electrode. Dawei et al. reported a novel method by capturing the change in the radius of curvature of the composite electrode/copper foil cantilever. This method was used to obtain real-time stress measurement on silicon composite electrode with the stress at the electrode around 0.015Gpa at a capacity of 1080 $mAhg^{-1}$.[99]

However, these measurement techniques usually need some ultra-stable measurement setup with the specialized modules to satisfy the sample and characterization equipment. These complex structures lead to the expensive cost and complicated operation process. Hence, a high-frequency capacitance characterization system was built in Chapter 5, which could directly measure the pulverization and stress effect in the coin cell with the composite silicon electrode, without any complex preparation of the samples.

1.4 References

[1] M. S. Whittingham, "History, Evolution, and Future Status of Energy Storage," *Proceedings of the IEEE,* vol. 100, no. Special Centennial Issue, pp. 1518-1534, 2012, doi: 10.1109/jproc.2012.2190170.

[2] R. Jasinski, *High-Energy Batteries*. New York: Plenum Press, 1967.

[3] F. R. Gamble, J. H. Osiecki, M. Cais, R. Pisharody, F. J. Disalvo, and T. H. Geballe, "Intercalation complexes of lewis bases and layered sulfides: a large class of new superconductors," *Science,* vol. 174, no. 4008, pp. 493-7, Oct 29 1971, doi: 10.1126/science.174.4008.493.

[4] M. S. Whittingham, "Electrical energy storage and intercalation chemistry," *Science,* vol. 192, no. 4244, pp. 1126-7, Jun 11 1976, doi: 10.1126/science.192.4244.1126.

[5] J. O. Besenhard and G. Eichinger, "High energy density lithium cells," *Journal of Electroanalytical Chemistry and Interfacial Electrochemistry,* vol. 68, no. 1, pp. 1-18, 1976, doi: 10.1016/s0022-0728(76)80298-7.

[6] K. Brandt, "Historical development of secondary lithium batteries," *Solid State Ionics,* vol. 69, no. 3-4, pp. 173-183, 1994, doi: 10.1016/0167-2738(94)90408-1.

[7] J. Broadhead and A. Butherus, "Rechargable nonaqueous battery," United States Patent Appl. 3,791,867, 1974.

[8] J. M. Tarascon and M. Armand, "Issues and challenges facing rechargeable

lithium batteries," *Nature,* vol. 414, no. 6861, pp. 359-367, 2001, doi: 10.1038/35104644.

[9] B. Scrosati and J. Garche, "Lithium batteries: Status, prospects and future," *Journal of Power Sources,* vol. 195, no. 9, pp. 2419-2430, 2010, doi: 10.1016/j.jpowsour.2009.11.048.

[10] M. S. Whittingham, "The Role of Ternary Phases in Cathode Reactions," *Journal of The Electrochemical Society,* vol. 123, no. 3, 1976, doi: 10.1149/1.2132817.

[11] K. Mizushima, P. C. Jones, P. J. Wiseman, and J. B. Goodenough, "LixCoO2 (0<x<-1): A new cathode material for batteries of high energy density," *Materials Research Bulletin,* vol. 15, no. 6, pp. 783-789, 1980, doi: 10.1016/0025-5408(80)90012-4.

[12] B. Xu, D. Qian, Z. Wang, and Y. S. Meng, "Recent progress in cathode materials research for advanced lithium ion batteries," *Materials Science and Engineering: R: Reports,* vol. 73, no. 5-6, pp. 51-65, 2012, doi: 10.1016/j.mser.2012.05.003.

[13] Y. Wang and G. Cao, "Developments in Nanostructured Cathode Materials for High-Performance Lithium-Ion Batteries," *Advanced Materials,* vol. 20, no. 12, pp. 2251-2269, 2008, doi: 10.1002/adma.200702242.

[14] G.-A. Nazri and G. Pistoia, *Lithium batteries: science and technology*. Springer Science & Business Media, 2008.

[15] T. H. Kim, J. S. Park, S. Chang, S. Choi, J. Ryu, and H. K. Song, "The Current Move of Lithium Ion Batteries Towards the Next Phase," *Advanced Energy*

Materials, vol. 2, no. 7, pp. 860-872, 2012, doi: 10.1002/aenm.201200028.

[16] D. Guerard and A. Herold, "Intercalation of lithium into graphite and other carbons," *Carbon,* vol. 13, no. 4, pp. 337-345, 1975, doi: 10.1016/0008-6223(75)90040-8.

[17] M. Arakawa and J.-I. Yamaki, "The cathodic decomposition of propylene carbonate in lithium batteries," *Journal of Electroanalytical Chemistry and Interfacial Electrochemistry,* vol. 219, no. 1-2, pp. 273-280, 1987, doi: 10.1016/0022-0728(87)85045-3.

[18] A. N. Dey and B. P. Sullivan, "The Electrochemical Decomposition of Propylene Carbonate on Graphite," *Journal of The Electrochemical Society,* vol. 117, no. 2, 1970, doi: 10.1149/1.2407470.

[19] R. Yazami and P. Touzain, "A reversible graphite-lithium negative electrode for electrochemical generators," *Journal of Power Sources,* vol. 9, no. 3, pp. 365-371, 1983, doi: 10.1016/0378-7753(83)87040-2.

[20] D. Billaud, F. X. Henry, and P. Willmann, "Electrochemical synthesis of binary graphite-lithium intercalation compounds," *Materials Research Bulletin,* vol. 28, no. 5, pp. 477-483, 1993, doi: 10.1016/0025-5408(93)90130-6.

[21] R. a. Fong, "Studies of Lithium Intercalation into Carbons Using Nonaqueous Electrochemical Cells," *Journal of The Electrochemical Society,* vol. 137, no. 7, 1990, doi: 10.1149/1.2086855.

[22] T. Ohzuku, "Formation of Lithium-Graphite Intercalation Compounds in Nonaqueous Electrolytes and Their Application as a Negative Electrode for a

Lithium Ion (Shuttlecock) Cell," *Journal of The Electrochemical Society,* vol. 140, no. 9, 1993, doi: 10.1149/1.2220849.

[23] C. J. Wen and R. A. Huggins, "Chemical diffusion in intermediate phases in the lithium-silicon system," *Journal of Solid State Chemistry,* vol. 37, no. 3, pp. 271-278, 1981, doi: 10.1016/0022-4596(81)90487-4.

[24] B. A. Boukamp, "All-Solid Lithium Electrodes with Mixed-Conductor Matrix," *Journal of The Electrochemical Society,* vol. 128, no. 4, 1981, doi: 10.1149/1.2127495.

[25] W. J. Weydanz, M. Wohlfahrt-Mehrens, and R. A. Huggins, "A room temperature study of the binary lithium–silicon and the ternary lithium–chromium–silicon system for use in rechargeable lithium batteries," *Journal of Power Sources,* vol. 81-82, pp. 237-242, 1999, doi: 10.1016/s0378-7753(99)00139-1.

[26] B. Gao, S. Sinha, L. Fleming, and O. Zhou, "Alloy Formation in Nanostructured Silicon," *Advanced Materials,* vol. 13, no. 11, pp. 816-819, 2001, doi: 10.1002/1521-4095(200106)13:11<816::Aid-adma816>3.0.Co;2-p.

[27] M. N. Obrovac and L. Christensen, "Structural Changes in Silicon Anodes during Lithium Insertion/Extraction," *Electrochemical and Solid-State Letters,* vol. 7, no. 5, 2004, doi: 10.1149/1.1652421.

[28] T. D. Hatchard and J. R. Dahn, "In Situ XRD and Electrochemical Study of the Reaction of Lithium with Amorphous Silicon," *Journal of The Electrochemical Society,* vol. 151, no. 6, 2004, doi: 10.1149/1.1739217.

[29] J. Li and J. R. Dahn, "An In Situ X-Ray Diffraction Study of the Reaction of Li with Crystalline Si," *Journal of The Electrochemical Society,* vol. 154, no. 3, 2007, doi: 10.1149/1.2409862.

[30] J. H. Ryu, J. W. Kim, Y.-E. Sung, and S. M. Oh, "Failure Modes of Silicon Powder Negative Electrode in Lithium Secondary Batteries," *Electrochemical and Solid-State Letters,* vol. 7, no. 10, 2004, doi: 10.1149/1.1792242.

[31] H. Wu and Y. Cui, "Designing nanostructured Si anodes for high energy lithium ion batteries," *Nano Today,* vol. 7, no. 5, pp. 414-429, 2012, doi: 10.1016/j.nantod.2012.08.004.

[32] C.-M. Hwang, C.-H. Lim, J.-H. Yang, and J.-W. Park, "Electrochemical properties of negative SiMox electrodes deposited on a roughened substrate for rechargeable lithium batteries," *Journal of Power Sources,* vol. 194, no. 2, pp. 1061-1067, 2009, doi: 10.1016/j.jpowsour.2009.05.047.

[33] S. Choi, T. W. Kwon, A. Coskun, and J. W. Choi, "Highly elastic binders integrating polyrotaxanes for silicon microparticle anodes in lithium ion batteries," *Science,* vol. 357, no. 6348, pp. 279-283, Jul 21 2017, doi: 10.1126/science.aal4373.

[34] N. Liu, Z. Lu, J. Zhao, M. T. McDowell, H. W. Lee, W. Zhao, and Y. Cui, "A pomegranate-inspired nanoscale design for large-volume-change lithium battery anodes," *Nat Nanotechnol,* vol. 9, no. 3, pp. 187-92, Mar 2014, doi: 10.1038/nnano.2014.6.

[35] H. Kim, B. Han, J. Choo, and J. Cho, "Three-dimensional porous silicon

particles for use in high-performance lithium secondary batteries," *Angew Chem Int Ed Engl,* vol. 47, no. 52, pp. 10151-4, 2008, doi: 10.1002/anie.200804355.

[36] H. Wu, G. Zheng, N. Liu, T. J. Carney, Y. Yang, and Y. Cui, "Engineering empty space between Si nanoparticles for lithium-ion battery anodes," *Nano Lett,* vol. 12, no. 2, pp. 904-9, Feb 8 2012, doi: 10.1021/nl203967r.

[37] B. Zhu, Y. Jin, Y. Tan, L. Zong, Y. Hu, L. Chen, Y. Chen, Q. Zhang, and J. Zhu, "Scalable Production of Si Nanoparticles Directly from Low Grade Sources for Lithium-Ion Battery Anode," *Nano Lett,* vol. 15, no. 9, pp. 5750-4, Sep 9 2015, doi: 10.1021/acs.nanolett.5b01698.

[38] L. F. Cui, R. Ruffo, C. K. Chan, H. Peng, and Y. Cui, "Crystalline-amorphous core-shell silicon nanowires for high capacity and high current battery electrodes," *Nano Lett,* vol. 9, no. 1, pp. 491-5, Jan 2009, doi: 10.1021/nl8036323.

[39] K. Peng, J. Jie, W. Zhang, and S.-T. Lee, "Silicon nanowires for rechargeable lithium-ion battery anodes," *Applied Physics Letters,* vol. 93, no. 3, p. 033105, 2008, doi: 10.1063/1.2929373.

[40] H. Föll, H. Hartz, E. Ossei-Wusu, J. Carstensen, and O. Riemenschneider, "Si nanowire arrays as anodes in Li ion batteries," *physica status solidi (RRL) - Rapid Research Letters,* vol. 4, no. 1-2, pp. 4-6, 2010, doi: 10.1002/pssr.200903344.

[41] N. Liu, H. Wu, M. T. McDowell, Y. Yao, C. Wang, and Y. Cui, "A yolk-shell design for stabilized and scalable li-ion battery alloy anodes," *Nano Lett,* vol.

12, no. 6, pp. 3315-21, Jun 13 2012, doi: 10.1021/nl3014814.

[42] M. Ko, S. Chae, J. Ma, N. Kim, H.-W. Lee, Y. Cui, and J. Cho, "Scalable synthesis of silicon-nanolayer-embedded graphite for high-energy lithium-ion batteries," *Nature Energy,* vol. 1, no. 9, p. 16113, 2016, doi: 10.1038/nenergy.2016.113.

[43] Y. Jin, S. Zhang, B. Zhu, Y. Tan, X. Hu, L. Zong, and J. Zhu, "Simultaneous Purification and Perforation of Low-Grade Si Sources for Lithium-Ion Battery Anode," *Nano Lett,* vol. 15, no. 11, pp. 7742-7, Nov 11 2015, doi: 10.1021/acs.nanolett.5b03932.

[44] H. Wang, H. Song, Z. Lin, X. Jiang, X. Zhang, L. Yu, J. Xu, L. Pan, J. Wang, M. Zheng, Y. Shi, and K. Chen, "Highly cross-linked Cu/a-Si core-shell nanowires for ultra-long cycle life and high rate lithium batteries," *Nanoscale,* vol. 8, no. 5, pp. 2613-9, Feb 7 2016, doi: 10.1039/c5nr06985h.

[45] H. Li, F. Cheng, Z. Zhu, H. Bai, Z. Tao, and J. Chen, "Preparation and electrochemical performance of copper foam-supported amorphous silicon thin films for rechargeable lithium-ion batteries," *Journal of Alloys and Compounds,* vol. 509, no. 6, pp. 2919-2923, 2011, doi: 10.1016/j.jallcom.2010.11.156.

[46] J. Wang, Q. Zhang, X. Li, D. Xu, Z. Wang, H. Guo, and K. Zhang, "Three-dimensional hierarchical Co3O4/CuO nanowire heterostructure arrays on nickel foam for high-performance lithium ion batteries," *Nano Energy,* vol. 6, pp. 19-26, 2014, doi: 10.1016/j.nanoen.2014.02.012.

[47] Q. Li, S. Hu, H. Wang, F. Wang, X. Zhong, and X. Wang, "Study of copper

foam-supported Sn thin film as a high-capacity anode for lithium-ion batteries," *Electrochim. Acta,* vol. 54, no. 24, pp. 5884-5888, 2009, doi: 10.1016/j.electacta.2009.05.051.

[48] F. Li, H. Yue, P. Wang, Z. Yang, D. Wang, D. Liu, L. Qiao, and D. He, "Synthesis of core–shell architectures of silicon coated on controllable grown Ni-silicide nanostructures and their lithium-ion battery application," *CrystEngComm,* vol. 15, no. 36, 2013, doi: 10.1039/c3ce40651b.

[49] Y. P. Wu, E. Rahm, and R. Holze, "Carbon anode materials for lithium ion batteries," *Journal of Power Sources,* vol. 114, no. 2, pp. 228-236, 2003, doi: 10.1016/s0378-7753(02)00596-7.

[50] S. Wu, C. Han, J. Iocozzia, M. Lu, R. Ge, R. Xu, and Z. Lin, "Germanium-Based Nanomaterials for Rechargeable Batteries," *Angew Chem Int Ed Engl,* vol. 55, no. 28, pp. 7898-922, Jul 4 2016, doi: 10.1002/anie.201509651.

[51] C. K. Chan, X. F. Zhang, and Y. Cui, "High Capacity Li-ion Battery Anodes Using Ge Nanowires," *Nano Lett,* vol. 8, no. 1, pp. 307-9, Jan 2008, doi: 10.1021/nl0727157.

[52] S. Yan, H. Song, S. Lin, H. Wu, Y. Shi, and J. Yao, "GeO(2) Encapsulated Ge Nanostructure with Enhanced Lithium-Storage Properties," *Advanced Functional Materials,* vol. 29, no. 8, 2019, doi: 10.1002/adfm.201807946.

[53] S. Wu, R. Wang, Z. Wang, and Z. Lin, "CuGeO(3) Nanowires Covered with Graphene as Anode Materials of Lithium Ion Batteries with Enhanced Reversible Capacity and Cyclic Performance," *Nanoscale,* vol. 6, no. 14, pp.

8350-8, Jul 21 2014, doi: 10.1039/c4nr00921e.

[54] Q. Liu, Y. Zhou, J. Kou, X. Chen, Z. Tian, J. Gao, S. Yan, and Z. Zou, "High-yield Synthesis of Ultralong and Ultrathin Zn(2)GeO(4) Nanoribbons Toward Improved Photocatalytic Reduction of CO(2) into Renewable Hydrocarbon Fuel," *J Am Chem Soc,* vol. 132, no. 41, pp. 14385-7, Oct 20 2010, doi: 10.1021/ja1068596.

[55] F. Jia, L. Song, W. Wei, P. Qu, and M. Xu, "Facile One-pot Method Synthesis CNT–GeO(2) Nanocomposite for High Performance Li-ion Battery Anode Material," *New Journal of Chemistry,* vol. 39, no. 1, pp. 689-695, 2015, doi: 10.1039/c4nj01742k.

[56] J. Zhang, T. Yu, J. Chen, H. Liu, D. Su, Z. Tang, J. Xie, L. Chen, A. Yuan, and Q. Kong, "Germanium-based Complex Derived Porous GeO(2) Nanoparticles for Building High Performance Li-ion Batteries," *Ceramics International,* vol. 44, no. 1, pp. 1127-1133, 2018, doi: 10.1016/j.ceramint.2017.10.069.

[57] J. Wu, N. Luo, S. Huang, W. Yang, and M. Wei, "Reversible Conversion Reaction of GeO(2) Boosts Lithium-ion Storage via Fe Doping," *Journal of Materials Chemistry A,* vol. 7, no. 9, pp. 4574-4580, 2019, doi: 10.1039/c8ta12434e.

[58] X. Liu, J. Zai, B. Li, J. Zou, Z. Ma, and X. Qian, "Na(2)Ge(4)O(9) Nanoparticles Encapsulated in 3D Carbon Networks with Long-term Stability and Superior Rate Capability in Lithium Ion Batteries," *Journal of Materials Chemistry A,* vol. 4, no. 27, pp. 10552-10557, 2016, doi: 10.1039/c6ta03085h.

[59] G. Gao, Y. Xiang, S. Lu, B. Dong, S. Chen, L. Shi, Y. Wang, H. Wu, Z. Li, A. Abdelkader, K. Xi, and S. Ding, "CTAB-assisted Growth of Self-supported Zn2GeO4 Nanosheet Network on a Conductive Foam as a Binder-free Electrode for Long-life Lithium-ion Batteries," *Nanoscale,* vol. 10, no. 3, pp. 921-929, Jan 18 2018, doi: 10.1039/c7nr05407f.

[60] S. Jin, G. Yang, H. Song, H. Cui, and C. Wang, "Ultrathin Hexagonal 2D Co(2)GeO(4) Nanosheets: Excellent Li-Storage Performance and ex Situ Investigation of Electrochemical Mechanism," *ACS Appl Mater Interfaces,* vol. 7, no. 44, pp. 24932-43, Nov 11 2015, doi: 10.1021/acsami.5b08446.

[61] W. Wei, A. Tian, F. Jia, K. Wang, P. Qu, and M. Xu, "Green Synthesis of GeO(2)/graphene Composites as Anode Material for Lithium-ion Batteries with High Capacity," *RSC Advances,* vol. 6, no. 90, pp. 87440-87445, 2016, doi: 10.1039/c6ra14819k.

[62] Z. Chen, Y. Yan, S. Xin, W. Li, J. Qu, Y.-G. Guo, and W.-G. Song, "Copper germanate nanowire/reduced graphene oxide anode materials for high energy lithium-ion batteries," *Journal of Materials Chemistry A,* vol. 1, no. 37, 2013, doi: 10.1039/c3ta12344h.

[63] H. Qiu, L. Zeng, T. Lan, X. Ding, and M. Wei, "In-situ Synthesis of GeO(2)/reduced Graphene Oxide Composite on Ni Foam Substrate as a Binder-free Anode for High-capacity Lithium-ion Batteries," *Journal of Materials Chemistry A,* vol. 3, no. 4, pp. 1619-1623, 2015, doi: 10.1039/c4ta05212a.

[64] X. L. Wang, W. Q. Han, H. Chen, J. Bai, T. A. Tyson, X. Q. Yu, X. J. Wang, and

X. Q. Yang, "Amorphous hierarchical porous GeO(x) as high-capacity anodes for Li ion batteries with very long cycling life," *J Am Chem Soc,* vol. 133, no. 51, pp. 20692-5, Dec 28 2011, doi: 10.1021/ja208880f.

[65] D. Lv, M. L. Gordin, R. Yi, T. Xu, J. Song, Y.-B. Jiang, D. Choi, and D. Wang, "GeOx/Reduced Graphene Oxide Composite as an Anode for Li-Ion Batteries: Enhanced Capacity via Reversible Utilization of Li(2)O along with Improved Rate Performance," *Advanced Functional Materials,* vol. 24, no. 8, pp. 1059-1066, 2014, doi: 10.1002/adfm.201301882.

[66] S. H. Choi, K. Y. Jung, and Y. C. Kang, "Amorphous GeOx-Coated Reduced Graphene Oxide Balls with Sandwich Structure for Long-Life Lithium-Ion Batteries," *ACS Appl Mater Interfaces,* vol. 7, no. 25, pp. 13952-9, Jul 1 2015, doi: 10.1021/acsami.5b02846.

[67] M. D. Stoller, S. Park, Y. Zhu, J. An, and R. S. Ruoff, "Graphene-based ultracapacitors," *Nano letters,* vol. 8, no. 10, pp. 3498-3502, 2008, doi: 10.1021/nl802558y.

[68] K. S. Novoselov, A. K. Geim, S. V. Morozov, D. Jiang, Y. Zhang, S. V. Dubonos, I. V. Grigorieva, and A. A. Firsov, "Electric field effect in atomically thin carbon films," *Science (New York, N.Y.),* vol. 306, no. 5696, pp. 666-669, 2004, doi: 10.1126/science.1102896.

[69] P. Goli, H. Ning, X. Li, C. Lu, K. S. Novoselov, and A. A. Balandin, "Thermal Properties of Graphene–Copper–Graphene Heterogeneous Films," *Nano Letters,* vol. 14, no. 3, pp. 1497-1503, 2014, doi: 10.1021/nl404719n.

[70] E. Yoo, J. Kim, E. Hosono, H.-s. Zhou, T. Kudo, and I. Honma, "Large Reversible Li Storage of Graphene Nanosheet Families for Use in Rechargeable Lithium Ion Batteries," *Nano Letters,* vol. 8, no. 8, pp. 2277-2282, 2008, doi: 10.1021/nl800957b.

[71] S. Wu, R. Xu, M. Lu, R. Ge, J. Iocozzia, C. Han, B. Jiang, and Z. Lin, "Graphene-Containing Nanomaterials for Lithium-Ion Batteries," *Advanced Energy Materials,* vol. 5, no. 21, p. 1500400, 2015, doi: 10.1002/aenm.201500400.

[72] G. Zhou, L. Li, C. Ma, S. Wang, Y. Shi, N. Koratkar, W. Ren, F. Li, and H.-M. Cheng, "A graphene foam electrode with high sulfur loading for flexible and high energy Li-S batteries," *Nano Energy,* vol. 11, pp. 356-365, 2015, doi: 10.1016/j.nanoen.2014.11.025.

[73] J. Luo, J. Liu, Z. Zeng, C. F. Ng, L. Ma, H. Zhang, J. Lin, Z. Shen, and H. J. Fan, "Three-dimensional graphene foam supported Fe(3)O(4) lithium battery anodes with long cycle life and high rate capability," *Nano Lett,* vol. 13, no. 12, pp. 6136-43, 2013, doi: 10.1021/nl403461n.

[74] Y. Li, D. Cao, Y. Wang, S. Yang, D. Zhang, K. Ye, K. Cheng, J. Yin, G. Wang, and Y. Xu, "Hydrothermal deposition of manganese dioxide nanosheets on electrodeposited graphene covered nickel foam as a high-performance electrode for supercapacitors," *Journal of Power Sources,* vol. 279, pp. 138-145, 2015, doi: 10.1016/j.jpowsour.2014.12.153.

[75] F. Wang, M. Zheng, L. Ma, Q. Li, J. Song, Y. You, L. Ma, and W. Shen, "Nickel

skeleton three-dimensional nitrogen doped graphene nanosheets/nanoscrolls as promising supercapacitor electrodes," *Nanotechnology,* vol. 28, no. 36, p. 365402, Sep 8 2017, doi: 10.1088/1361-6528/aa79e4.

[76] W. Zhang, C. Xu, C. Ma, G. Li, Y. Wang, K. Zhang, F. Li, C. Liu, H. M. Cheng, Y. Du, N. Tang, and W. Ren, "Nitrogen-Superdoped 3D Graphene Networks for High-Performance Supercapacitors," *Adv Mater,* vol. 29, no. 36, Sep 2017, doi: 10.1002/adma.201701677.

[77] Z. Chen, W. Ren, L. Gao, B. Liu, S. Pei, and H. M. Cheng, "Three-dimensional flexible and conductive interconnected graphene networks grown by chemical vapour deposition," *Nat Mater,* vol. 10, no. 6, pp. 424-8, Jun 2011, doi: 10.1038/nmat3001.

[78] R. Mo, D. Rooney, K. Sun, and H. Y. Yang, "3D nitrogen-doped graphene foam with encapsulated germanium/nitrogen-doped graphene yolk-shell nanoarchitecture for high-performance flexible Li-ion battery," *Nat Commun,* vol. 8, p. 13949, Jan 4 2017, doi: 10.1038/ncomms13949.

[79] H. Wang, H. Yi, X. Chen, and X. Wang, "Asymmetric supercapacitors based on nano-architectured nickel oxide/graphene foam and hierarchical porous nitrogen-doped carbon nanotubes with ultrahigh-rate performance," *J. Mater. Chem. A,* vol. 2, no. 9, pp. 3223-3230, 2014, doi: 10.1039/c3ta15046a.

[80] C.-C. Kung, P.-Y. Lin, Y. Xue, R. Akolkar, L. Dai, X. Yu, and C.-C. Liu, "Three dimensional graphene foam supported platinum–ruthenium bimetallic nanocatalysts for direct methanol and direct ethanol fuel cell applications,"

Journal of Power Sources, vol. 256, pp. 329-335, 2014, doi: 10.1016/j.jpowsour.2014.01.074.

[81] F. Li, H. Yue, Z. Yang, X. Li, Y. Qin, and D. He, "Flexible free-standing graphene foam supported silicon films as high capacity anodes for lithium ion batteries," *Materials Letters,* vol. 128, pp. 132-135, 2014, doi: 10.1016/j.matlet.2014.04.114.

[82] M. Ghidiu, M. R. Lukatskaya, M. Q. Zhao, Y. Gogotsi, and M. W. Barsoum, "Conductive two-dimensional titanium carbide 'clay' with high volumetric capacitance," *Nature,* vol. 516, no. 7529, pp. 78-81, Dec 4 2014, doi: 10.1038/nature13970.

[83] Y. T. Liu, P. Zhang, N. Sun, B. Anasori, Q. Z. Zhu, H. Liu, Y. Gogotsi, and B. Xu, "Self-Assembly of Transition Metal Oxide Nanostructures on MXene Nanosheets for Fast and Stable Lithium Storage," *Adv Mater,* vol. 30, no. 23, p. e1707334, Jun 2018, doi: 10.1002/adma.201707334.

[84] M. Naguib, M. Kurtoglu, V. Presser, J. Lu, J. Niu, M. Heon, L. Hultman, Y. Gogotsi, and M. W. Barsoum, "Two-dimensional Nanocrystals Produced by Exfoliation of Ti(3)AlC(2)," *Adv Mater,* vol. 23, no. 37, pp. 4248-53, Oct 4 2011, doi: 10.1002/adma.201102306.

[85] S. Kajiyama, L. Szabova, H. Iinuma, A. Sugahara, K. Gotoh, K. Sodeyama, Y. Tateyama, M. Okubo, and A. Yamada, "Enhanced Li-Ion Accessibility in MXene Titanium Carbide by Steric Chloride Termination," *Advanced Energy Materials,* vol. 7, no. 9, 2017, doi: 10.1002/aenm.201601873.

[86] X. Tang, X. Guo, W. Wu, and G. Wang, "2D Metal Carbides and Nitrides (MXenes) as High-Performance Electrode Materials for Lithium-Based Batteries," *Advanced Energy Materials,* vol. 8, no. 33, 2018, doi: 10.1002/aenm.201801897.

[87] N. Sun, B.-y. Yang, J.-c. Zheng, Z.-j. He, H. Tong, L.-b. Tang, C.-s. An, and B. Xiao, "Effect of Synthesis Temperature on the Phase Structure, Morphology and Electrochemical Performance of Ti(3)C(2) as an Anode Material for Li-ion Batteries," *Ceramics International,* vol. 44, no. 14, pp. 16214-16218, 2018, doi: 10.1016/j.ceramint.2018.05.267.

[88] Y. Zhang, Z. Mu, J. Lai, Y. Chao, Y. Yang, P. Zhou, Y. Li, W. Yang, Z. Xia, and S. Guo, "MXene/Si@SiOx@C Layer-by-Layer Superstructure with Autoadjustable Function for Superior Stable Lithium Storage," *ACS Nano,* vol. 13, no. 2, pp. 2167-2175, Feb 26 2019, doi: 10.1021/acsnano.8b08821.

[89] Z. Xiao, Z. Li, P. Li, X. Meng, and R. Wang, "Ultrafine Ti(3)C(2) MXene Nanodots-Interspersed Nanosheet for High-Energy-Density Lithium-Sulfur Batteries," *ACS Nano,* vol. 13, no. 3, pp. 3608-3617, Mar 26 2019, doi: 10.1021/acsnano.9b00177.

[90] M. Q. Zhao, C. E. Ren, Z. Ling, M. R. Lukatskaya, C. Zhang, K. L. Van Aken, M. W. Barsoum, and Y. Gogotsi, "Flexible MXene/carbon Nanotube Composite Paper with High Volumetric Capacitance," *Adv Mater,* vol. 27, no. 2, pp. 339-45, Jan 14 2015, doi: 10.1002/adma.201404140.

[91] M. Arakawa, S.-i. Tobishima, Y. Nemoto, M. Ichimura, and J.-i. Yamaki,

"Lithium electrode cycleability and morphology dependence on current density," *Journal of Power Sources,* vol. 43, no. 1-3, pp. 27-35, 1993, doi: 10.1016/0378-7753(93)80099-b.

[92] M. J. Chon, V. A. Sethuraman, A. McCormick, V. Srinivasan, and P. R. Guduru, "Real-time measurement of stress and damage evolution during initial lithiation of crystalline silicon," *Phys Rev Lett,* vol. 107, no. 4, p. 045503, Jul 22 2011, doi: 10.1103/PhysRevLett.107.045503.

[93] X. H. Liu and J. Y. Huang, "In situ TEM electrochemistry of anode materials in lithium ion batteries," *Energy & Environmental Science,* vol. 4, no. 10, p. 3844, 2011, doi: 10.1039/c1ee01918j.

[94] M. Balasubramanian, X. Sun, X. Q. Yang, and J. McBreen, "In situ X-ray diffraction and X-ray absorption studies of high-rate lithium-ion batteries," *Journal of Power Sources,* vol. 92, no. 1-2, pp. 1-8, 2001, doi: 10.1016/s0378-7753(00)00493-6.

[95] X.-Q. Yang, J. McBreen, W.-S. Yoon, and C. P. Grey, "Crystal structure changes of LiMn0.5Ni0.5O2 cathode materials during charge and discharge studied by synchrotron based in situ XRD," *Electrochemistry Communications,* vol. 4, no. 8, pp. 649-654, 2002, doi: 10.1016/s1388-2481(02)00406-x.

[96] K. Dokko, M. Mohamedi, N. Anzue, T. Itoh, and I. Uchida, "In situ Raman spectroscopic studies of LiNixMn2 − xO4thin film cathode materials for lithium ion secondary batteries," *J. Mater. Chem.,* vol. 12, no. 12, pp. 3688-3693, 2002, doi: 10.1039/b206764a.

[97] R. Bhattacharyya, B. Key, H. Chen, A. S. Best, A. F. Hollenkamp, and C. P. Grey, "In situ NMR observation of the formation of metallic lithium microstructures in lithium batteries," *Nat Mater,* vol. 9, no. 6, pp. 504-10, Jun 2010, doi: 10.1038/nmat2764.

[98] D. Aurbach, M. Koltypin, and H. Teller, "In Situ AFM Imaging of Surface Phenomena on Composite Graphite Electrodes during Lithium Insertion," *Langmuir,* vol. 18, no. 23, pp. 9000-9009, 2002, doi: 10.1021/la020306e.

[99] D. Li, Y. Wang, J. Hu, B. Lu, Y.-T. Cheng, and J. Zhang, "In situ measurement of mechanical property and stress evolution in a composite silicon electrode," *Journal of Power Sources,* vol. 366, pp. 80-85, 2017, doi: 10.1016/j.jpowsour.2017.09.004.

Chapter 2: Characterization Techniques

2.1 X-ray Diffraction (XRD)

X-ray diffraction (XRD) is the most common technique to study the crystalline structures of materials. Typically, a certain number of electrons are boiled off from the cathode and then accelerated by a large electric potential (> 50kV), then, the high-speed electrons are collided with a copper plate to produces strong K_α and K_β rays. These rays penetrate to the internal of the object and interact with the solid's lattice structure, in which, the interference of the incident rays with the crystalline will occurs by changing the incident angle θ of K_α rays. (**Figure 2.1**) This incident angle θ correspond to the lattice spacing of the object crystalline structure, determined by Bragg's law:

$$2d\sin\theta = n\lambda \tag{2.1}$$

The parameter d is the spacing between the two planes of atoms (lattice spacing), n is the order of reflection, λ is the wavelength of the K_α rays. This lattice spacing d can be used to identify the structure of crystal and arrangement of atoms.. However, when the size of crystallite is down to the nanoscale because the length of the range order in the structure of the crystal is not enough, the destructive interference with the direction of scattering has occurred. The Scherrer equation can be used for the calculation of crystallite size in sub-micrometer/nanometer crystallites or particles:[1, 2]

$$D = \frac{K\lambda}{\beta \cos\theta} \tag{2.2}$$

In equation 2.2, the D is the average of crystallite size, K is the shape factor which depends on the aspect ratio of crystallites, λ is the wavelength of the K_α rays, and β is the full width at half maximum (FWHM).

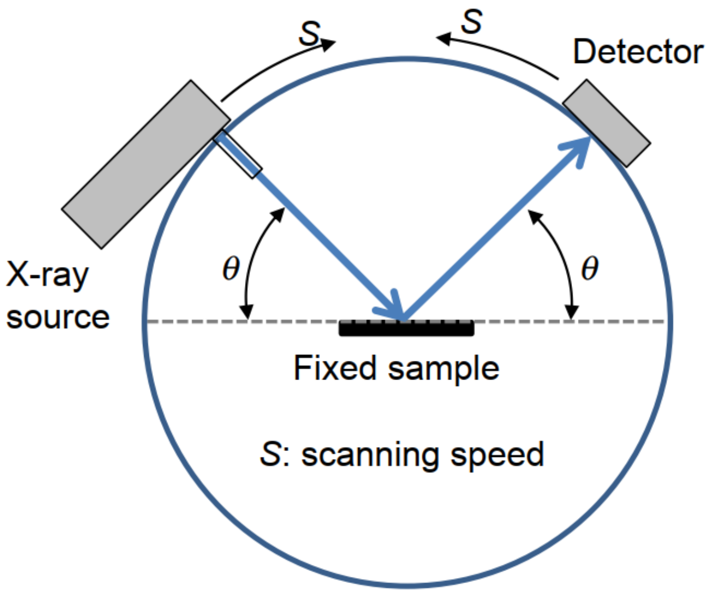

Figure 2.1 Principle of the XRD system with θ/θ goniometers.[3]

2.2 Scanning Electron Microscope (SEM)

The SEM is an extremely effective technique to observe and investigate the morphologic features of the sample, which has a higher resolution than the conventional optical microscope. Typically, the SEM uses Lanthanum hexaboride (LaB_6) as the thermionic emitter, the filament is heated with a large current to reach a high temperature above 2000K, which can accelerate the energy of electron to the range of 0.1 and 30 KeV. These electron beams are focused by using a series of lenses and finally interacts with the sample to get a clear visualization. **Figure 2.2** has shown the schematic diagram of typical SEM.

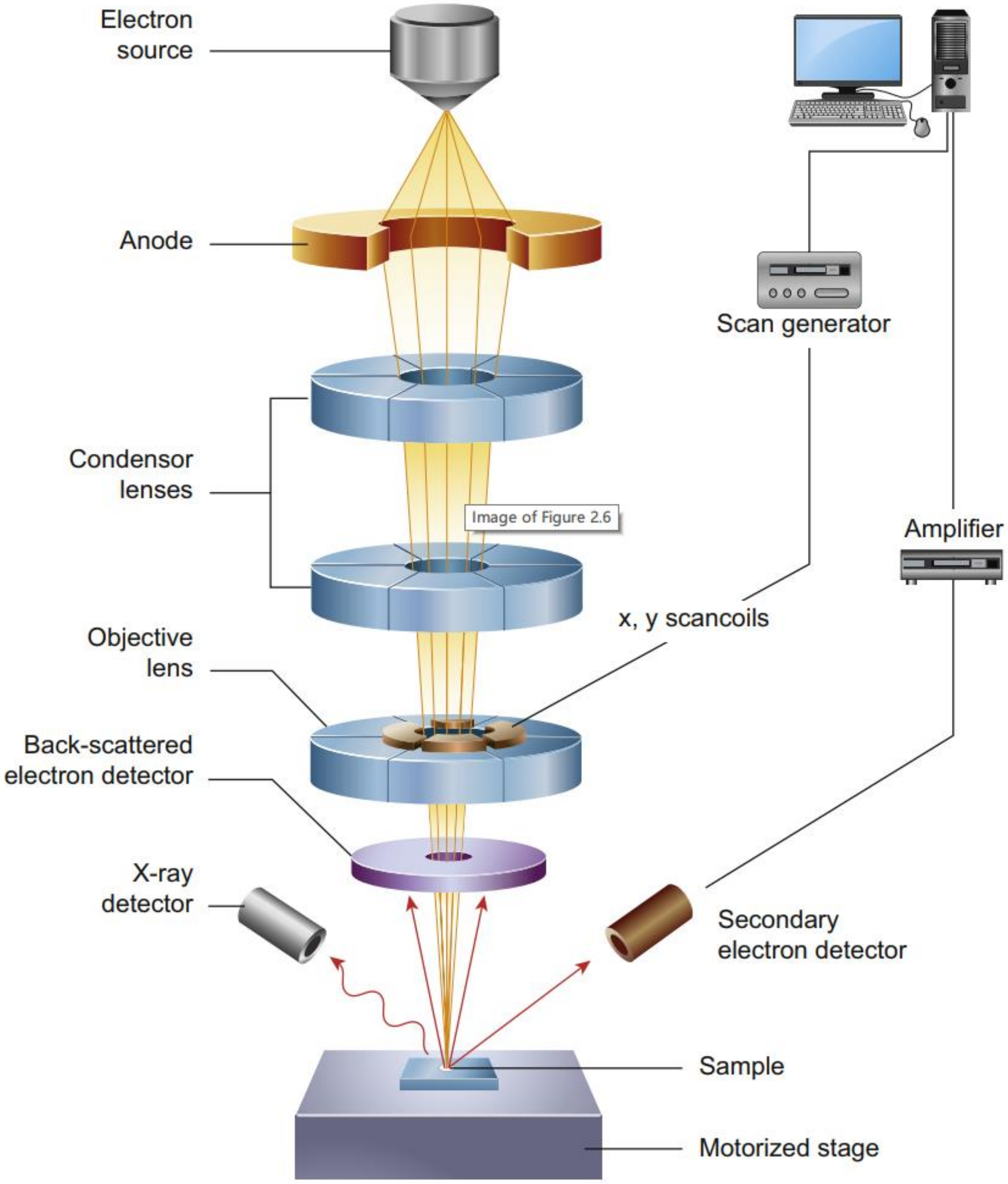

Figure 2.2 Schematic diagram of the SEM microscope.[4]

There are many types of particles (e.g., secondary electrons (SE), backscattered electrons (BSE), Auger electrons, and X-ray photons) are generated when the electron beam interacts with the sample in SEM. In these electrons, the SE and BSE are commonly used for the display as an image. The SE are low energy (<50eV) electrons, which are generated by inelastic scattering interactions between the electron beam with the valance or conductive band of sample atoms. The low energy of that means these electrons are ejected from a shallow depth of sample (few nanometers), which could be collected and detected by a scintillator-type Everhart-Thornley detector. This detector usually placed in the sidewise of the specimen holder. The SE can be collected by a faraday cage, and then accelerated and detected in the detector, which can achieve an ideal resolution around 3.5 nm for a tungsten-filament electron source. The BSE are high energy electrons that are ejected by the elastic scattering interactions between electron beam with specimen atoms. The feature of the BSE is the energy of backscatter electrons for heavy elements is larger than the light elements, which can be easily observed by the brightness of the image. This feature makes the BSE can be used to observe the chemical distribution in compositions. The BSE can be detected by the solid-state or scintillator-photomultipliers type detectors. These detectors normally placed around the electron beam, which makes the BSE are directly received by detectors. **Figure 2.3** has shown the Everhart-Thornley and circular BSE detector in SEM.[5]

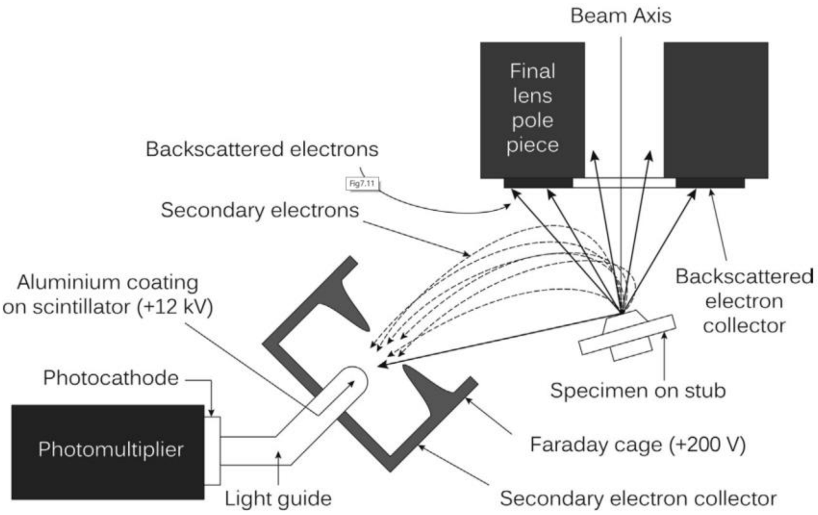

Figure 2.3 Everhart-Thornley and circular BSE detector.

When the electrons penetrate into the inner shell of the specimen atom, the Auger electrons and X-ray photons are ejected due to the electron from high energy level falls into the vacancy. In this falling process, the energy will be released by the atoms to form an emitted photon or another electron. These photons and electrons are X-ray photons and Auger electrons, respectively. By using these particles, the techniques can be developed to provide the element analysis or semi-quantitative compositional of the specimen such as Auger electron spectroscopy (AES) and energy dispersive analysis of X-ray (EDAX).

2.3 Transmission Electron Microscopy (TEM)

Unlike the SEM, the operating principle of TEM is using the electron beam transmitted through the sample to observe the structure of the object, which structure is similar to the optical microscope (OM) but uses the electron beam instead of the visible light source (**Figure 2.4**). Because the wavelength of the electron beam is much smaller than the visible light, the resolution of TEM is much larger than the conventional OM. The wavelength of the electron depends on the energy of the accelerated electron, which follows the formula:

$$\lambda_e \approx \frac{h}{\sqrt{2m_0E(1+\frac{E}{2m_0c^2})}} \tag{2.3}$$

In this formula, the m_0 is the rest mass of the electron, E is the energy of the electron, c is the speed of light, and h is the Planck constant. According to this formula, the wavelength can be effectively reduced by increasing the energy of the accelerated electron, which can be achieved by accelerating the electron in a high voltage electric potential when it is ejected from the tungsten filament or field electron emission source. After that, these electrons are focused by a series of electromagnetic and electrostatic lenses onto the sample. However, because of the small wavelength of the electrons, the solid-state specimen needs to be prepared with ultrathin thickness less than 100nm to make the electron beam can be transmitted through the sample. For the small particles, it needs to be prepared as a suspension on a metal grid.

The transmitted electrons are finally collected by the detector at the bottom of TEM, which consists of many types of information for samples such as electron density, periodicity, and phase. There are three imaging methods commonly used to obtain the information of sample in TEM, which are amplitude contrast, diffraction contrast, and phase contrast. When the electron beam transmitted through the sample, some of the electrons will be lost due to the scattering and absorption by the specimen, which causes the amplitude change in the detector. These electrons lost from the absorption can be used to form the mass-thickness contrast. When the electrons penetrate into the sample with the different distribution of the mass or thickness, the heavier or thicker area will scatter electrons with a larger angle and these electrons can be blocked by the objective aperture in the bright-field TEM. The block of the scattered electrons results in the low intensity appears on the heavier or thicker area. This difference of the intensity can be used to draw the morphology of sample structure. The diffraction contrast is normally used for the crystalline materials when the crystal with the specific crystallographic orientation of a grain. In this situation, the probability of scattering depends on the oriented way of the atomic planes, therefore the diffraction contrast can be used to demonstrate the orientation of the crystals in the crystalline or polycrystalline structure. In the high-resolution transmission electron microscopy (HRTEM), the phase contrast is employed for the image forming. Because of the electron-specimen interaction, the phase change of electrons wave will occur when the electron through the specimen with uniform thickness.[6] These phase changes can be used to provide more information about the structure of the object.

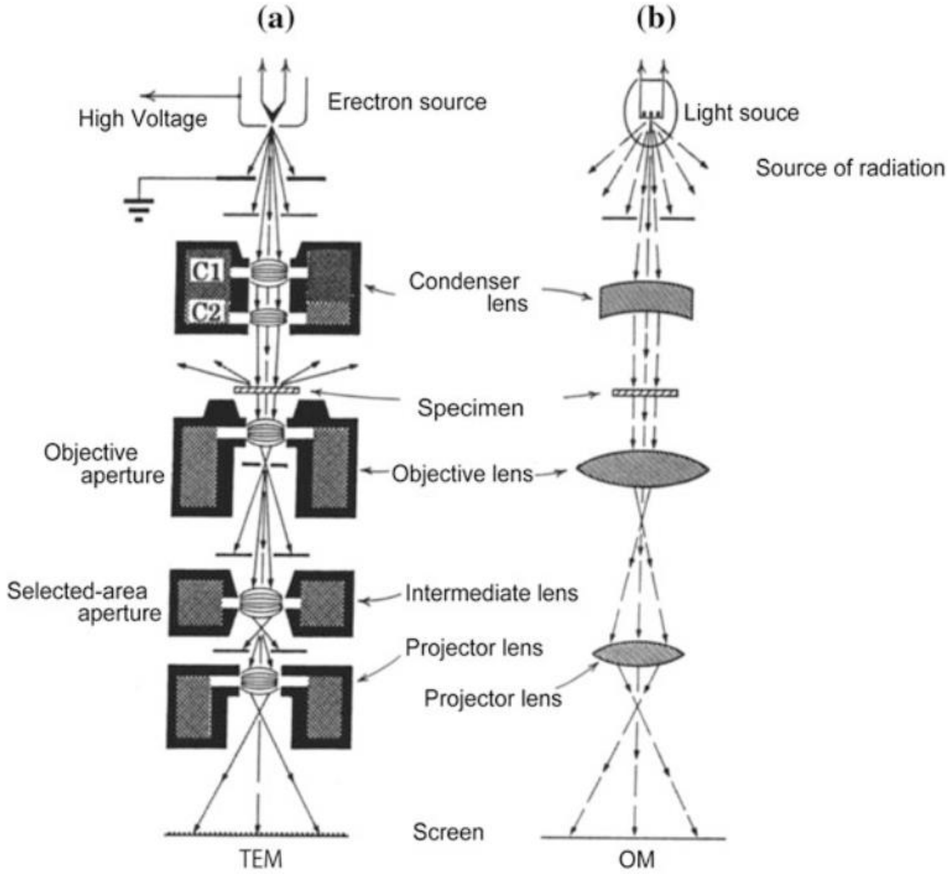

Figure 2.4 Schematic diagram of the TEM microscope. [7]

2.4 Raman Spectroscopy

The Raman spectroscopy is normally used to identify the vibrations mode in molecules, which is an effective technique to determine the physical and chemical structure of samples, and furthermore, it can provide the characteristic spectral patterns and semi-quantitatively or quantitatively analyzation for the substance in the object. The specimen of Raman spectroscopy is easy to prepare with a wide range of physical states such as liquids, solids, micro or nanoparticles, surface layer, and even for vapors. Moreover, because the method of Raman spectroscopy is rapid and simple, it can be used for the in-situ measurement of LIBs.[8]

For the system of Raman spectroscopy, a light source is an integrant part to emit the laser into the sample. The light source normally is equipped with more than one wavelength of leaser sources to satisfy various samples, such as the near-infrared laser which $\lambda = 785$ nm, the red laser which $\lambda = 633$ nm, and the green laser with $\lambda = 532$ nm. These different sources can emit the laser into the materials with different penetration depth to satisfy the various types of samples. Typically, after the light source, a series of adjustable neutral density filters are required to reduce the intensity of the light source for all wavelengths, which is used to protect the sensitive sample to prevent the radiation or heating damage. Finally, this laser with the specific intensity is focused by a microscope to reduce the laser beam down to <1 um, which microscope also act as a collector to collect the scattered photons to the detectors. Moreover, the stage of this microscope is normally can be controlled and motorized by the system to perform the automatic mapping of the sample surface. The schematic diagram of the Raman spectroscopy has shown in **Figure 2.5**.

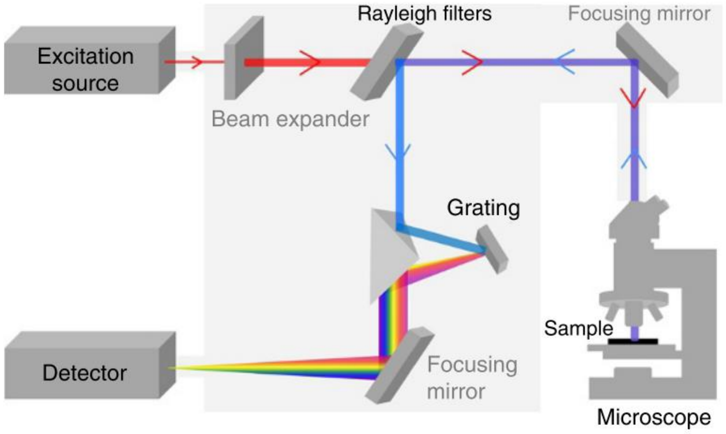

Figure 2.5 Schematic diagram of the Raman spectroscopy. [9]

2.5 References

[1] P. Scherrer, "Bestimmung der Grösse und der inneren Struktur von Kolloidteilchen mittels Röntgenstrahlen," *Nachrichten von der Gesellschaft der Wissenschaften zu Göttingen,* pp. 98-100, 1918.

[2] A. L. Patterson, "The Scherrer Formula for X-Ray Particle Size Determination," *Physical Review,* vol. 56, no. 10, pp. 978-982, 1939, doi: 10.1103/PhysRev.56.978.

[3] J. Epp, "X-ray diffraction (XRD) techniques for materials characterization," in *Materials Characterization Using Nondestructive Evaluation (NDE) Methods*, 2016, pp. 81-124.

[4] B. J. Inkson, "Scanning electron microscopy (SEM) and transmission electron microscopy (TEM) for materials characterization," in *Materials Characterization Using Nondestructive Evaluation (NDE) Methods*, 2016, pp. 17-43.

[5] F. Adams and C. Barbante, "Electron-Based Imaging Techniques," in *Chemical Imaging Analysis*, (Comprehensive Analytical Chemistry, 2015, pp. 269-313.

[6] E. J. Kirkland, *Advanced Computing in Electron Microscopy*. Springer, 2010.

[7] N. Tanaka, "Structure and Imaging of a Transmission Electron Microscope (TEM)," in *Electron Nano-Imaging*, 2017, ch. Chapter 2, pp. 17-28.

[8] E. Pollak, G. Salitra, V. Baranchugov, and D. Aurbach, "In Situ Conductivity, Impedance Spectroscopy, and Ex Situ Raman Spectra of Amorphous Silicon

during the Insertion/Extraction of Lithium," *The Journal of Physical Chemistry C,* vol. 111, no. 30, pp. 11437-11444, 2007, doi: 10.1021/jp0729563.

[9] H. J. Butler, L. Ashton, B. Bird, G. Cinque, K. Curtis, J. Dorney, K. Esmonde-White, N. J. Fullwood, B. Gardner, P. L. Martin-Hirsch, M. J. Walsh, M. R. McAinsh, N. Stone, and F. L. Martin, "Using Raman spectroscopy to characterize biological materials," *Nat Protoc,* vol. 11, no. 4, pp. 664-87, Apr 2016, doi: 10.1038/nprot.2016.036.

Chapter 3: Alloyed Cu/Si Core-shell Nanoflowers on the Three-dimensional Graphene Foam as an Anode for Lithium-ion Batteries

3.1 Three-dimensional Graphene Foam (3DGF)

Owing to its unique structure (a single atomic layer of carbon hexagons), graphene possesses many fascinated properties such as large specific surface area (2630 m^2 g^{-1})[1], excellent electric conductivity (~15000 cm^2 $V^{-1}S^{-1}$ at 300K)[2], high thermal conductivity (~3000 W Mk^{-1}, room temperature)[3], and planar sp^2-hyberidized carbon hexagons framework. In this decade years, many approaches have been developed for the synthesis of graphene, consisting of chemical vapor deposition (CVD) grown on metal substrate[4-7], mechanical exfoliation from graphite[8], chemical exfoliation from graphite oxide[9, 10], and ultrasonic exfoliation of graphite powder[11]. However, a majority of approaches introduced lots of defects in the hexagons carbon structure. These defects break the electron path and reduce the mechanical strength of graphene. Fortunately, the large-area and high-quality graphene could be grown on different metal substrates by CVD, which is far superior to other chemical approaches.

Herein, we chose a method to synthesize the 3DGF with ambient-pressure chemical vapor deposition (APCVD) by using the nickel foam as substrates[12]. A nickel foam (1.5 mm × 3.5 cm × 3.5 cm, purchased from Liyuan Novel Materials from Changde, China) was used as a template (**Figure 3.1**) for 3DGF synthesis. Firstly, it was loaded into a vacuum tube in a APCVD machine. Then the tube was heated to 1000 °C at a speed of 10 °C /min with the flow of Ar and H_2 (1000 sccm:500 sccm) at the atmosphere pressure. After that, a small amount (50 sccm) of CH_4 was then introduced into the tube for facilitating the graphene deposition. After 10 min of gas mixture flow, the samples were rapidly cooled down to the room temperature with the same flow of Ar_2 and H_2. (**Figure 3.2**) Finally, the as-prepared Ni/GF samples were etched in 3M HCl aqueous solution at 80 °C for 240 min to fully remove all the nickel foam templates to get the 3DGF. The resulting free-standing 3DGF has a mass density around 0.50-0.55 mg cm^{-2}.

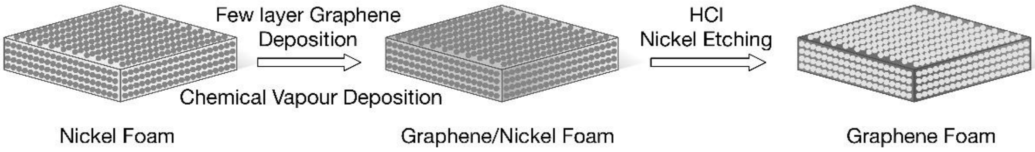

Figure 3.1 Schematic diagram of synthesizing three-dimensional graphene foam (3DGF).

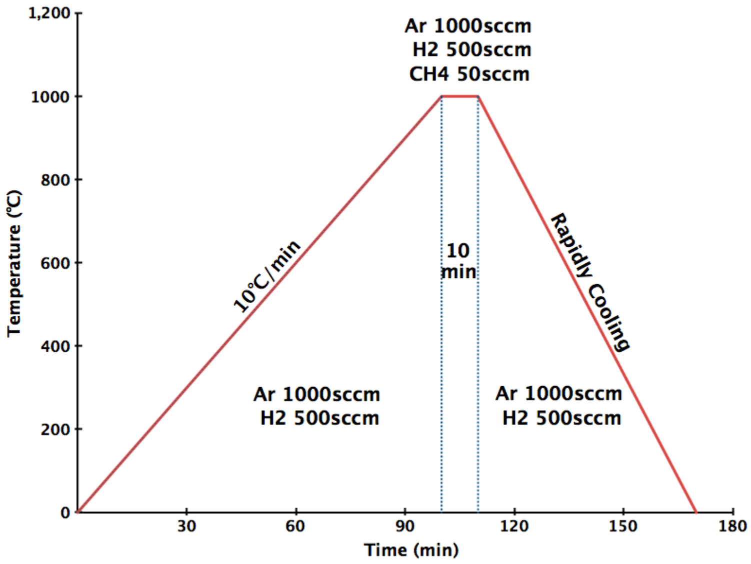

Figure 3.2 The CVD process in 3DGF synthesis.

Figure 3.3 shows the morphology of 3DGF by SEM and TEM. The SEM shows a three-dimensional (3D) porous structure with an interconnected 3D scaffold of nickel. This nickel as the template for the growth of graphene. The bare 3DGF covering on the nickel foam structure is smooth without large break or defect. The hollow graphene bridge is about 30-60 μm wide and the diameter of pores ranges from 60 μm to 200 μm. The TEM graph shows the 3-6 layers of graphene film achieved by APCVD.

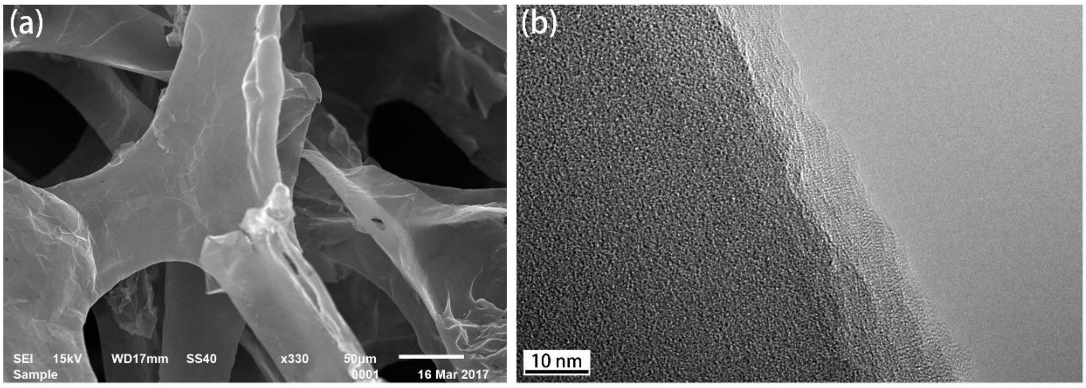

Figure 3.3 (a) SEM characterization of bare as-prepared three-dimensional graphene foam (3DGF), (b) TEM characterization of bare as-prepared 3DGF.

Figure 3.4 provides the Raman spectrum of the as-prepared 3DGF. Two bands locate at 1581 cm^{-1} and 2725 cm^{-1} correspond to G and 2D peaks of graphene. Based on the full width at half maximum (FWHM) of 2D and G band, and the intensity ratio of 2D to G band ($I_{2D}/I_G = 0.59$), the graphene film is estimated to be 4-5 layers [13] (**Table 3.1**). It is also noted that no band occurs at 1350 cm^{-1}, indicating the absence of defects for the as-prepared 3DGF.

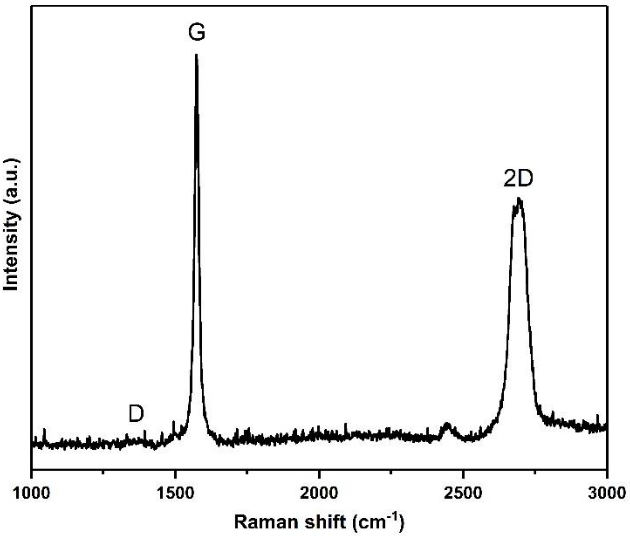

Figure 3.4 Raman spectra of 3DGF.

Table 3.1 Analysis of Raman spectrum of as-prepared 3DGF.

	FWHM (cm^{-1}) of G band	FWHM (cm^{-1}) of 2D band	Intensity ratio G/2D	Number of layers
Bare 3DGF (this work)	**17.1**	**71.3**	**0.56**	~4
Ref. [13]	13.0	60.4	0.59	3
	13.4	63.0	0.48	4
	12.6	65.0	0.41	5

3.2 Silicon-Copper Alloy Nanoflower Growth on the 3DGF

Here, we demonstrated a facile method to fabricate a flexible alloyed Cu/Si core-shell nanoflowers (NFs) structure located on 3DGF as an anode for LIBs. In this interconnected core-shell structure, the copper diffused into the Si NFs significantly improves the electrode conductivity and provides a pathway to allow the electron moving fast from the current collector to Si. Moreover, the use of 3DGF as the current collector not only offers a robust mechanical support for long-term cycle stability, but also significantly increases the mass loading of the Si due to its high specific surface area. By assembling this structure in CR2032 coin type half LIBs, the alloyed Cu/Si core-shell NFs anode achieves a final capacity of 896 mAh g^{-1} at current density of 3.2 A g^{-1} for 1000 cycles, with capacity retention of 54.4 %. Remarkably, this anode could even cycle at a high charging/discharging current density of 18 A g^{-1} for 30 runs, and then back to the 1.8 A g^{-1} with 77.7 % capacity retention. Our results reveal that the alloyed Cu/Si core-shell 3DGF nanostructure could be a promising anode material for lithium-ion batteries with superior capacity and cycling stability. Meanwhile, the 3DGF is extremely light and flexible, offering enormous potential to be used in the flexible batteries for future smartwatch or micro implantable biosensor system.

3.2.1 Experiment section

3.2.1.1 Methodology

The schematic diagram of synthesizing alloyed Cu/Si core-shell NFs on the 3DGF was shown in **Figure 3.5** To synthesize the CuO NFs on the 3DGF, Cu NPs were firstly electrodeposited on the as-prepared 3DGF with an electrochemical potential of –0.40 V for 30 s in 0.1 M Cu_2SO_4 and 0.3 M H_2SO_4 aqueous solution by an electrochemical workstation (Metrohm Autolab PGSTAT302N). Then the 3DGF covered with Cu nanoparticles was etched and oxidized in a mixed 0.05 M $K_2S_2O_8$ and 1.5 M NaOH aqueous solution at 80 °C for 2 min to achieve the final 3GDF/CuO NFs.

The plasma enhanced chemical vapor deposition (PECVD) was employed to deposit the Si shell over CuO NFs under the gas flow of 35.5 sccm SiH_4 and 2 sccm H_2 for 90 min at 100 °C. 11 W RF power under 0.2 Torr pressure was used. According to the difference in weight of the whole electrode before and after, the Si mass loading over the CuO NFs was measured to be 0.20-0.25 mg cm^{-2}. After that, the sample was heated to 450 °C in a vacuum tube with 45 sccm H_2 under 1.4 Torr pressure for 4 hours. This procedure was aimed to reduce the CuO to Cu under the Si shell and alloy this Cu with Si. The final resulting alloyed Cu/Si core-shell nanoflowered structure was used as the electrode in LIBs. **Figure 3.6** shows the optical images of 3DGF, 3DGF/Cu NPs, 3DGF/CuO NFs, 3DGF/CuO/Si NFs, and 3DGF/Cu/Si NFs samples. These images exhibit the morphology evolution of samples in different experimental processes.

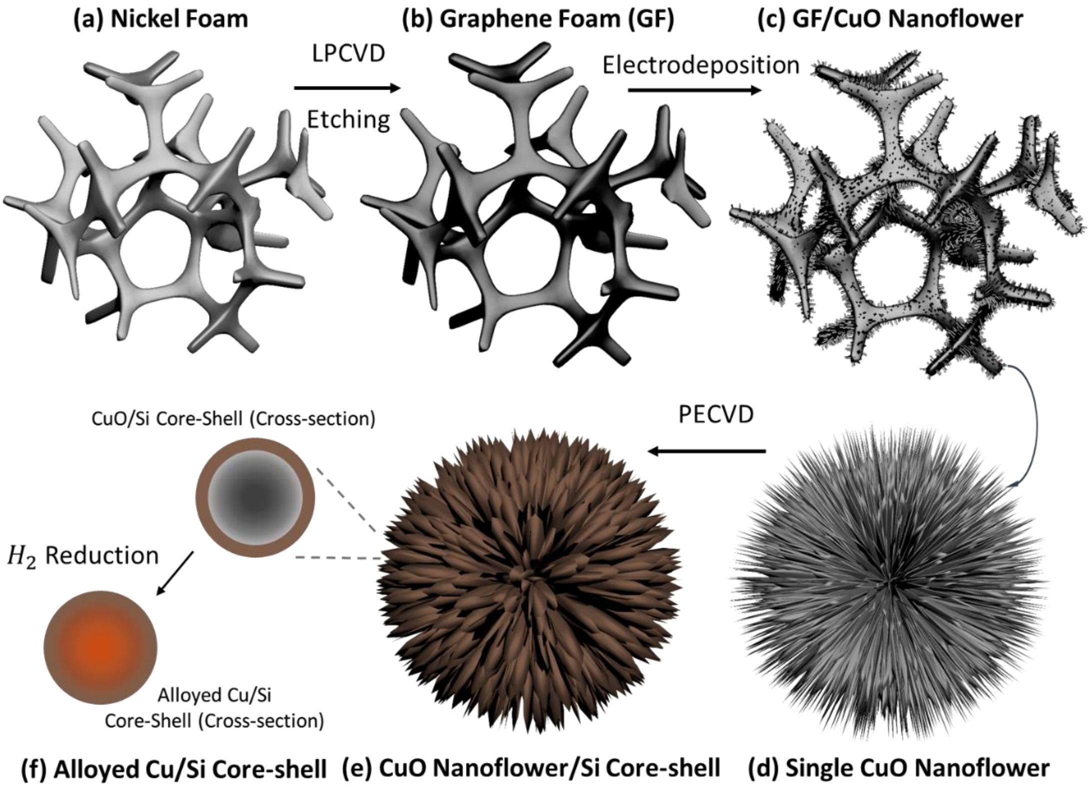

Figure 3.5 Schematic diagram of synthesizing alloyed Cu/Si core-shell NFs on the 3DGF.

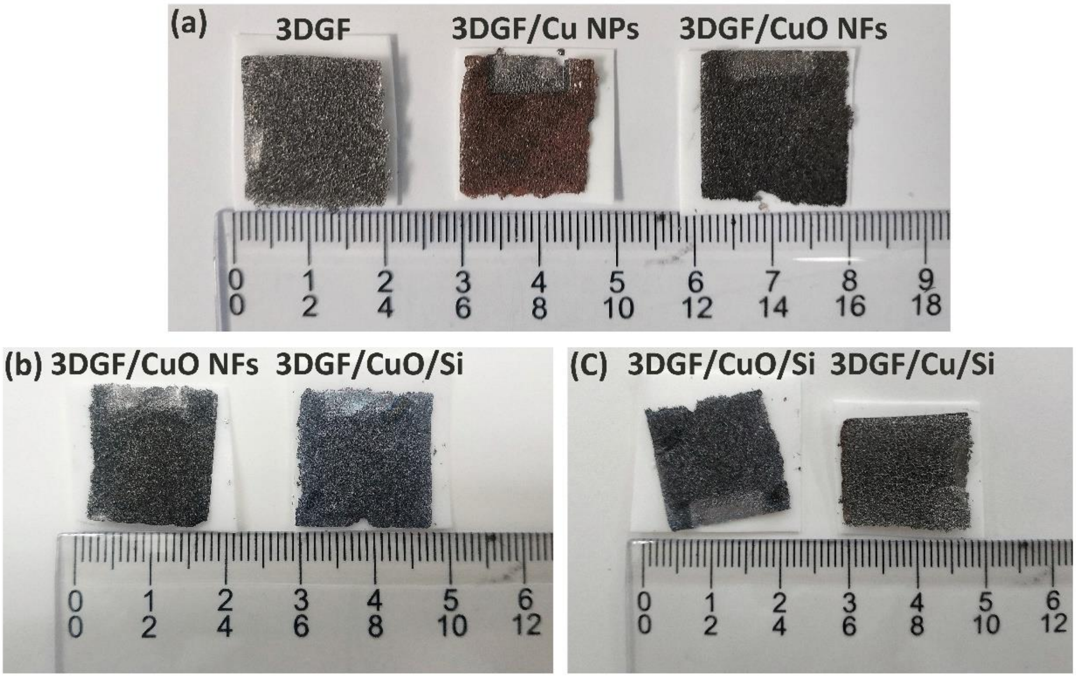

Figure 3.6 Optical images of (a) 3DGF, 3DGF/Cu NPs, and 3DGF/CuO NFs samples; (b) 3DGF/CuO NFs and 3DGF/CuO/Si NFs samples; and (c) 3DGF/CuO/Si NFs and 3DGF/Cu/Si NFs samples.

3.2.1.2 Structural Characterization

The structures and morphologies of the samples were observed by the field-emission scanning electron microscopy (FE-SEM, Hitachi S-4700), high-resolution transmission electron microscopy (HR-TEM, FEI Tecnai G2 F30), and Raman spectrometer (Horiba HR800 Raman system with 532nm wavelength). The energy dispersive spectrometer (EDS) was performed to examine the elemental information. The X-ray powder diffraction (Burker Advance D8) was used to identify the crystal structure of the resultant materials.

3.2.1.3 Electrochemical Measurements

To further characterize the electrochemical properties, CR2032-type coin cells were firstly assembled in an argon-filled glove box (H_2O, O_2 <0.5 ppm). In this half-cell test, the electrode with Cu/Si NFs anchored on 3DGF was directly used as the working electrode without any binder and conductive additive. The Li metal was acted as the negative electrode. The electrolyte was 1M $LiPF_6$ in a solution mixture of dimethyl carbonate (DMC) and ethylene carbonate (EC) (1:1 vol%). The galvanostatic cycling test was carried out with cut-off voltages of 0.01 V and 2 V on a multichannel batteries test system (Neware BTS-4000). The cycling voltammetry was measured by using an electrochemical workstation (Metrohm Autolab PGSTAT302N) at the scanning rate of 0.1 mV s^{-1} in two-electrode system. The mass density of 3DGF and mass loading of Si were determined by a high precision electronic balance (Mettler Toledo, 0.01mg).

3.2.2 Structural Characterization

Figure 3.7a-c shows the SEM characterization of the as-prepared CuO NFs anchored on the 3DGF substrate by a facile electrochemical deposition process. The diameter of high-density distribution CuO NFs is estimated to be 3.5-4.5 μm from the enlarged images of **Figure 3.7b** and **Figure 3.7c**. Each petal of NFs is measured to be approximately 200 nm width with 1 μm in length. The final achieved Cu/Si Core-Shell NFs on 3DGF are shown in **Figure 3.7d-f**. The diameters of the Cu/Si core-shell NFs increase to around 4-5.5 μm. **Figure 3.7f** shows the partial view of a single Cu/Si NF.

After depositing Si shell on NFs, the diameter of the core-shell Cu/Si petal becomes approximately 400 nm. Through a simple comparison with the CuO petal, the thickness of the sidewall-coated Si shell is around 100-150 nm. This NFs structure could effectively release the stress effect when the Si expands during lithiation processes. **Figure 3.8** shows typical SEM images of Cu/Si NFs grown on 3DGF with different distribution at different magnifications. The number inserted indicates the concentration of $CuSO_4$ and H_2SO_4 electrolyte used in electrochemical deposition electrolyte. It is clear that for 0.1 M $CuSO_4$/0.3M H_2SO_4 electrolyte the morphology of Cu/Si NFs is the most optimal without any unexpected spikes and inhomogeneous distribution.

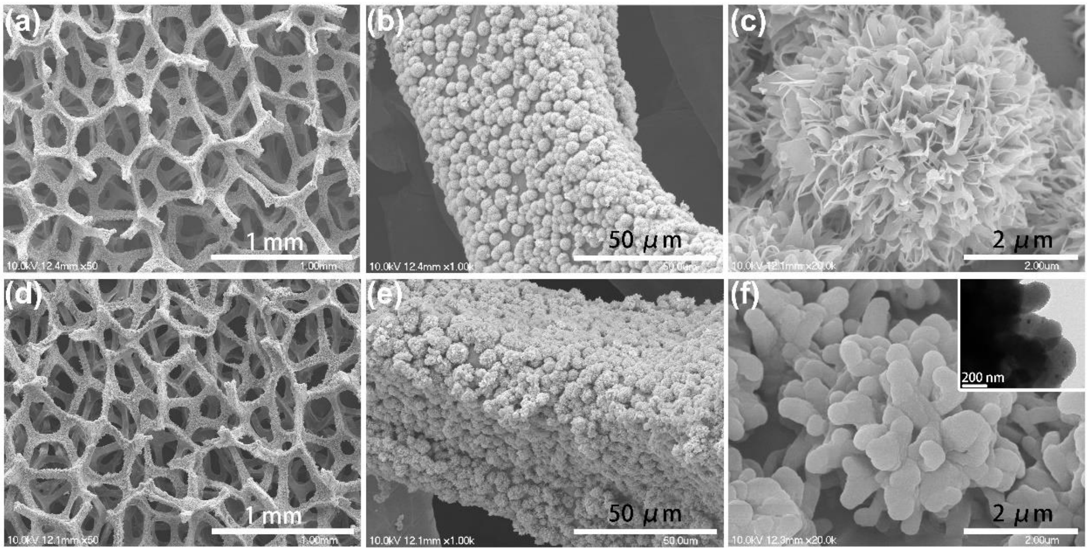

Figure 3.7 (a) and (b) low- and high-magnification SEM characterization of CuO NFs anchored on 3DGF; (c) partial enlarged detail of a single CuO NF; (d, e) low- and high-magnification SEM of Cu/Si core-shell NFs grown on 3DGF; (f) partial enlarged detail of a single Cu/Si core-shell NF by SEM characterization. The insert shows the TEM image of Cu/Si core-shell structure on the single NF.

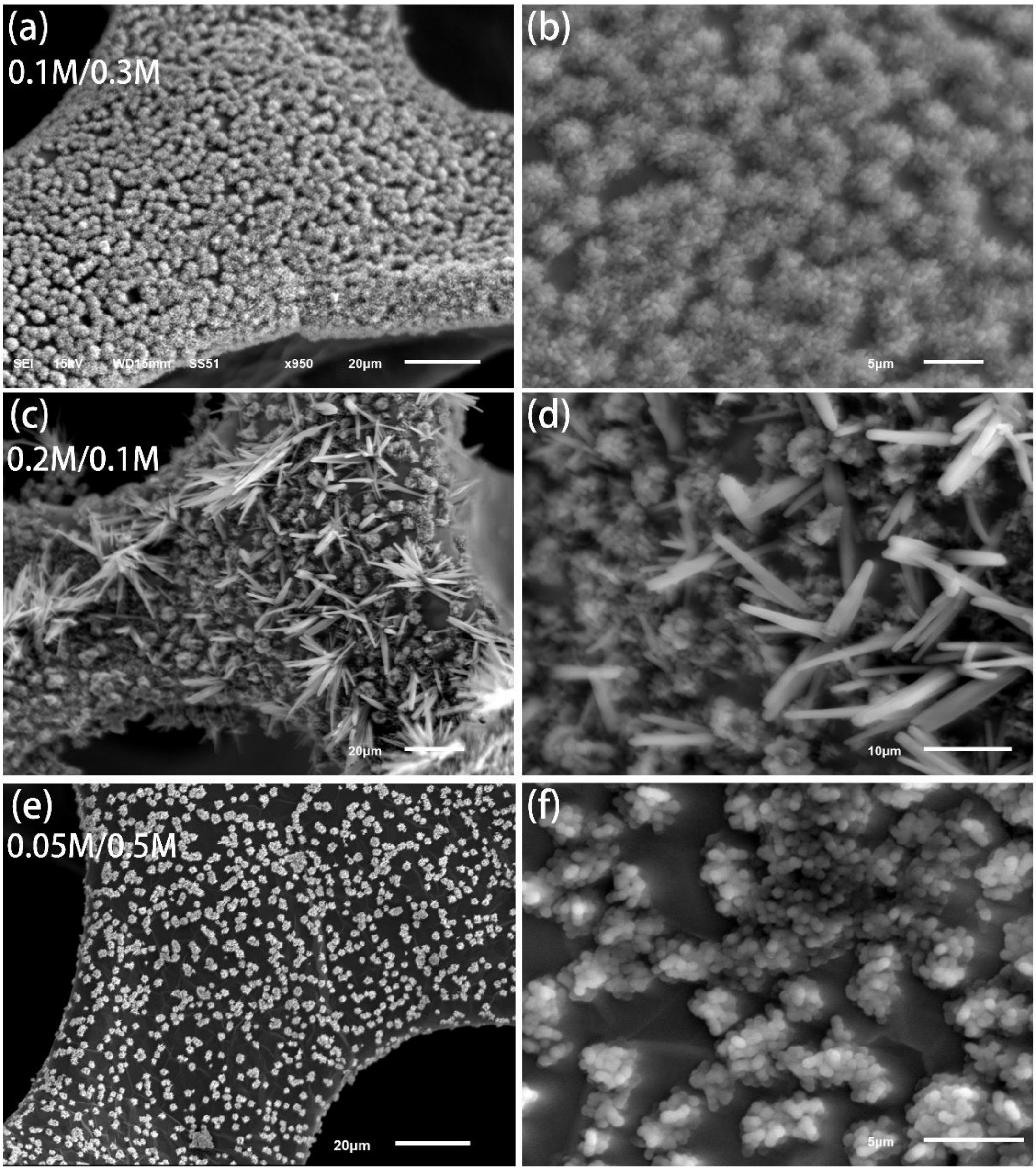

Figure 3.8 Typical SEM images of Cu/Si nanoflowers (NFs) grown on 3DGF with different distribution at different magnifications. The number inserted indicate the concentration of $CuSO_4$ and H_2SO_4 sources in electrochemical deposition electrolyte.

To examine further details, the TEM image and EDS mapping of the unannealed CuO/Si core-shell NFs and annealed Cu/Si core-shell NFs on 3DGF are provided in **Figure 3.9**. As seen in **Figure 3.9a**, before annealing a significant core-shell boundary between CuO and Si is observed. The Si shell and CuO core are identified separately by different gray levels. Most of CuO cores were uniformly coated with the Si shell by the PECVD system, which is also confirmed by the EDS mapping of Cu and Si elements with a single unannealed CuO/Si NF (**Figure 3.9c**). This boundary becomes ambiguous after H_2 annealing at 450 °C for 4h, as shown in **Figure 3.9b** and **Figure 3.9d**, suggesting that the Cu core is successfully diffused into Si shell by the annealing processes.

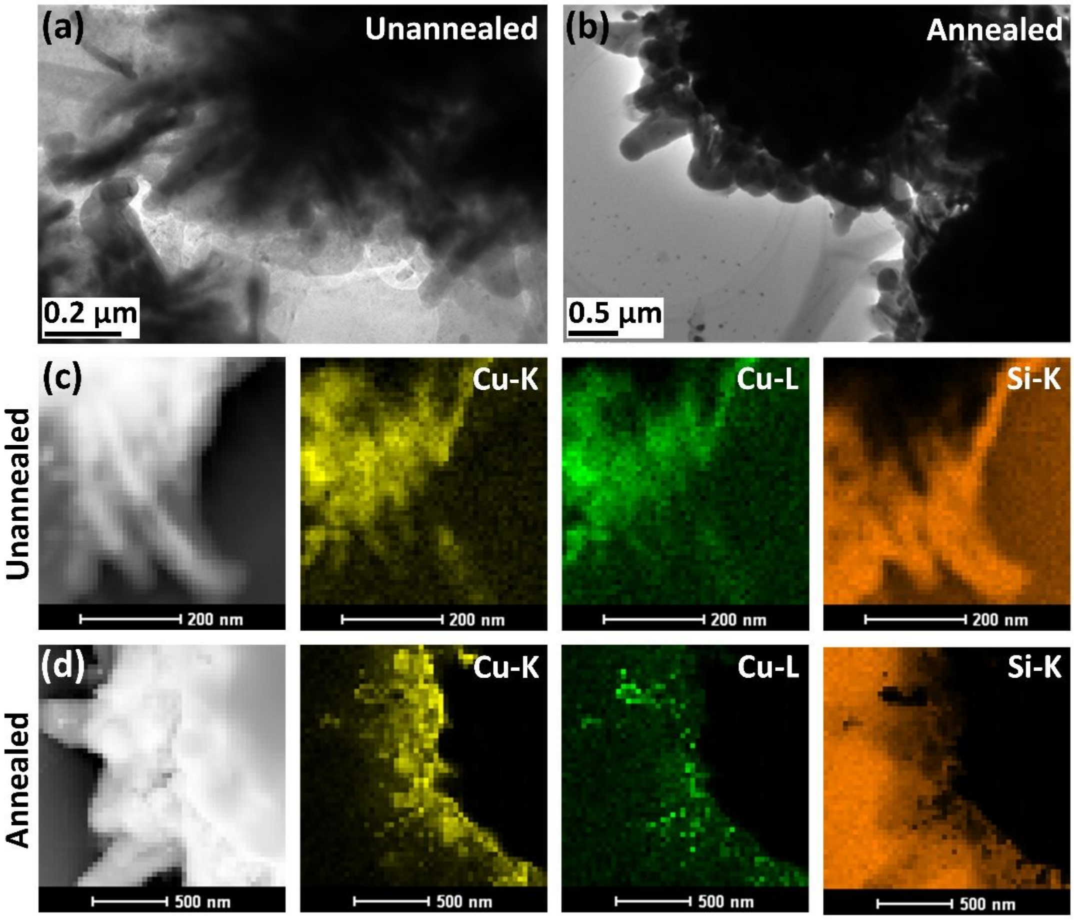

Figure 3.9 (a, c) TEM image and EDS mapping of the unannealed CuO/Si Core-Shell NFs on 3DGF, (b, d) TEM image and EDS mapping of the Cu/Si Core-Shell NFs on 3DGF annealed in hydrogen atmosphere at 450 °C for 4h.

Figure 3.10 shows the EDS carbon, copper, and silicon elements mapping of Cu/Si core-shell NFs grown on 3DGF. In Si mapping image, the element Si (cyan color) is mainly aggregated on the CuO NFs, indicating that the CuO NFs is more desirable for the deposition of Si to be coated on compared with the bare 3DGF, Large specific surface area of this NF structure may result in more active sites, therefore improving the Si mass loading and the conductivity of the whole electrode.

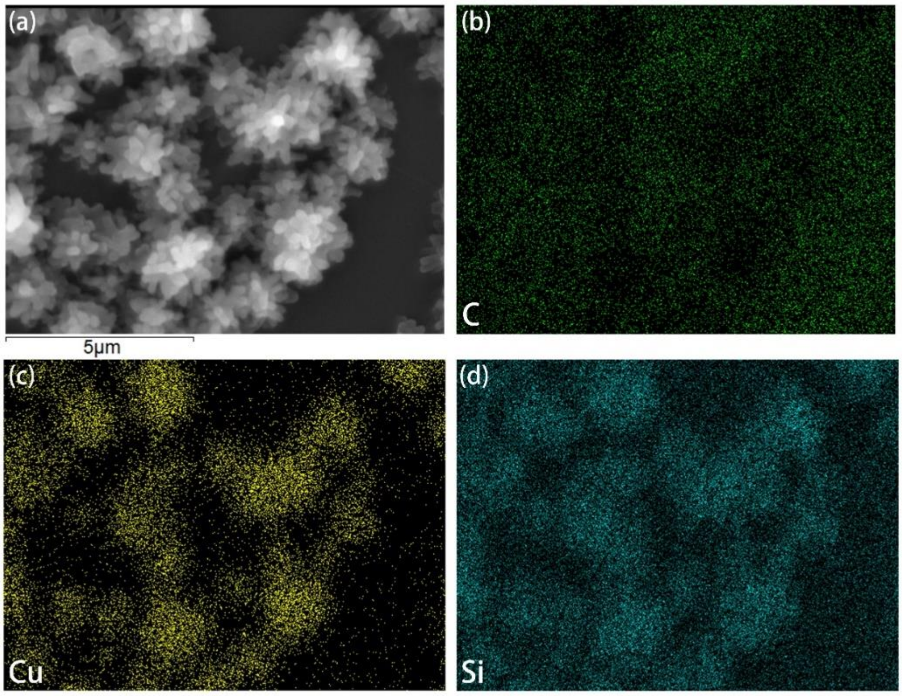

Figure 3.10 (a) SEM image of the Cu/Si Core-Shell NFs on 3DGF, (b-d) corresponding EDS carbon, copper, and silicon elemental mapping.

Figure 3.11 shows the XRD patterns for the CuO NFs, CuO/Si core-shell structure, and alloyed Cu/Si core-shell structure after being annealed at 350 °C and 450 °C for 4 hours. Regarding to the CuO NFs structure, a series of sharp diffraction peaks of CuO and Cu_2O are observed in accordance with PDF #44-0706 and #35-1091, which is an evidence of the oxidation from Cu nanoparticles to CuO NFs by NaOH and K_2SO_4 solution. After the Si shell coating on the CuO NFs by PECVD, no obvious peak is observed in related to Si shell, suggesting the formation of amorphous Si film on the CuO NFs. It was reported that the amorphous Si demonstrates more effective lithiation/delithiation process than the crystallized Si [14]. After simple annealing at 350 °C under H_2 for 4 hours, all the diffraction peaks associated with CuO and Cu_2O disappear Several new sharp diffraction peaks located at 36.6°, 44.5°, 44.9°, 77.5°, and 82.2° appear, which are consistent with crystalline planes of Cu_3Si (201), (012), (300), (430) and (003) (PDF #51-0916), respectively. With increasing the annealing temperature to 450 °C, no other new peaks were emerged, suggesting that the temperature 350 °C is favorite to activate the reduction of CuO to form the Cu-Si alloy.

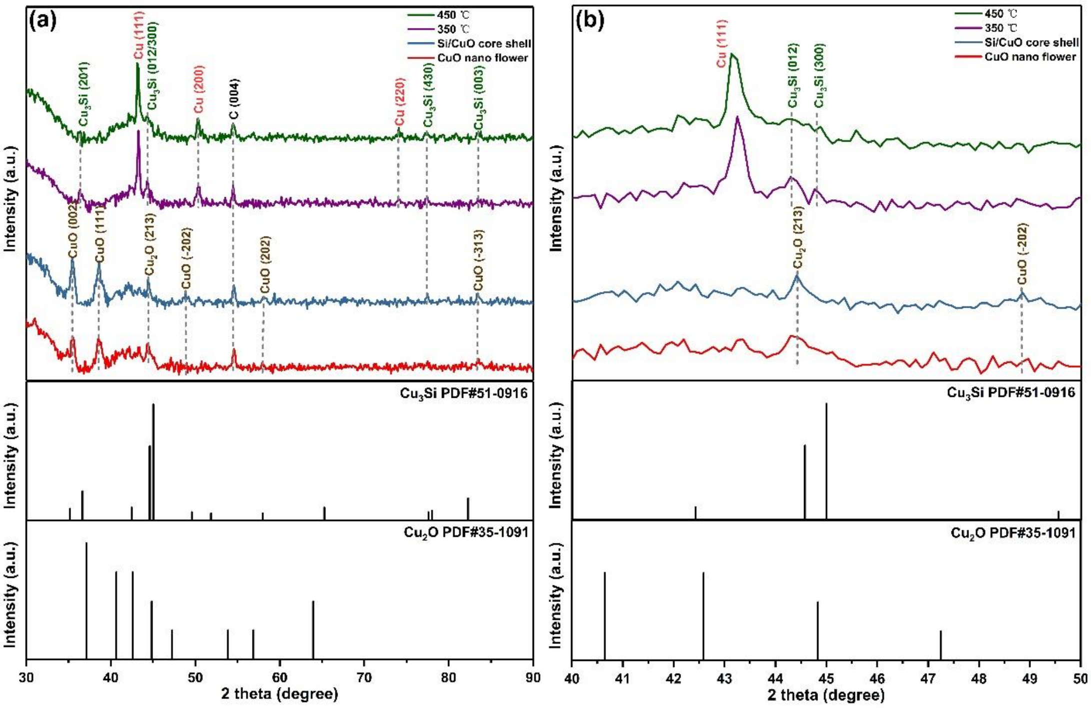

Figure 3.11 (a) XRD spectra of CuO NFs, CuO/Si core-shell structure, and alloyed Cu/Si core-shell structure after annealing at 350 °C and 450 °C compare with PDF

card #51-0916, #35-1091, and #44-0706 (b) partial detail of XRD spectra with 2 theta from 40 ° to 50 °.

3.2.3 Electrochemical Performance

For the electrochemical test of the alloyed Cu/Si core-shell NFs anode, we use a standard CR2032 coin cell to test the cyclic voltammetry (CV) and galvanostatic charge-discharge. In this test, the mass density of Si in Cu/Si core-shell NFs anode and bare 3DGF are measured to be around 0.20-0.25 mg cm^{-2} and 0.50-0.55 mg cm^{-2}, respectively. The half-cell test of this composite anode shows an initial discharge capacity of 1868 mAh g^{-1} at current density of 1.6 A g^{-1}, based on the Si mass. In comparison, the bare 3DGF without Si coating results in a discharge capacity of only 280 mAh g^{-1} in a control experiment (**Figure 3.14**). Therefore, the mass of Si is approximately used in all calculations.

Figure 3.12 shows the CV curves of the alloyed Cu/Si core-shell NFs anode measured with a scan rate of 0.1 mV s^{-1} over the potential window of 0.01 V to 1.1 V versus Li$^+$/Li. During the first discharge of alloyed Cu/Si anode, a cathodic peak at ~ 0.7 V is observed, but disappears in subsequent cycles, implying that this peak relates to the formation of solid SEI. After that, two peaks occur at 0.15 V and 0.03 V at the first discharge process, corresponding to the formation of Li$_x$Si by the lithiation of Si. These two peaks are also observed in the second and third discharge processes, implying a similar reaction pathway of two-stage lithiation process in subsequent cycles. When the battery is charging, two sharp peaks are observed at 0.30 V and 0.46 V in the anodic scan, which suggests that the phase changes from $Li_{15}Si_4$ alloy back to the amorphous Li_xSi, and the Li ion release from the Si anode. The peaks located at 0.01V and 0.23V in the cathodic and anodic scan are attributed to the lithiation/delithtaion process of graphene in the 3DGF substrate. When compared the whole three CV cycles, it can be seen that the CV curves of subsequent cycles almost overlap the previous cycle except a slight difference probably be caused by the surface change during the lithiation of Si. These results demonstrate a good reversibility for the redox reaction of Si anodes.

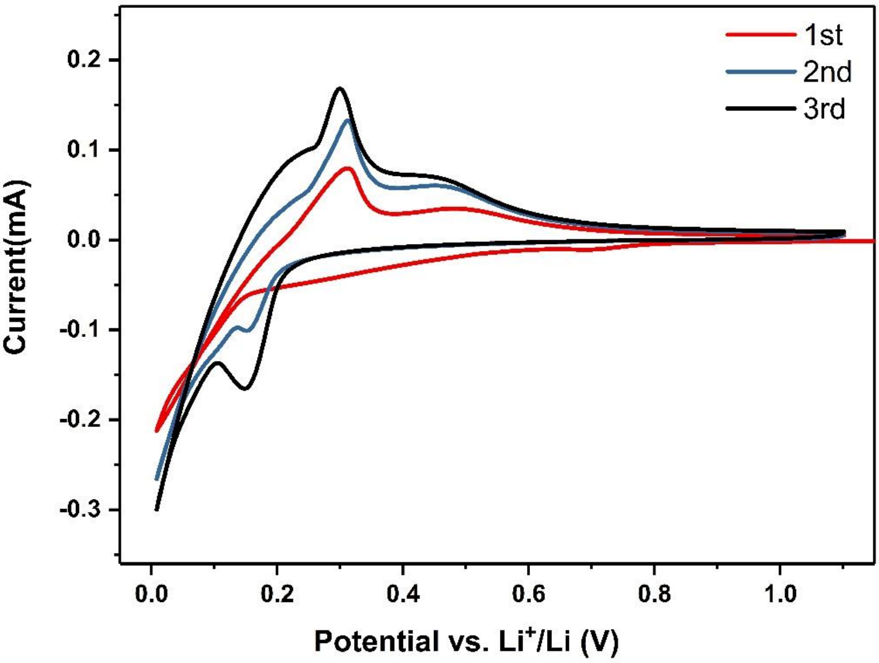

Figure 3.12 The cyclic voltammetry (CV) curves of alloyed Cu/Si core-shell NFs in the first three cycles with the scan rate of 0.1 mV s^{-1} between 0.01 V to 1.1 V.

Figure 3.13 shows the first three galvanostatic discharge/charge voltage profiles cycling at a current density of 0.35 A g^{-1}. Two voltage plateaus around 30 mV and 200 mV are observed on the discharge curve, due to the lithiation of Si shell on Cu NFs. For the charge curves, the voltage plateaus around 300 mV and 450 mV can be found, in a good agreement with the peaks shown in the CV curves in Figure 6a. Meanwhile, in the first discharge cycle, an earlier voltage stage occurs ~700mV during the first lithium-ion insertion of alloyed Cu/Si anode, which is consistent with the cathodic peak associated with the surface formation of SEI shown in **Figure 3.12**.

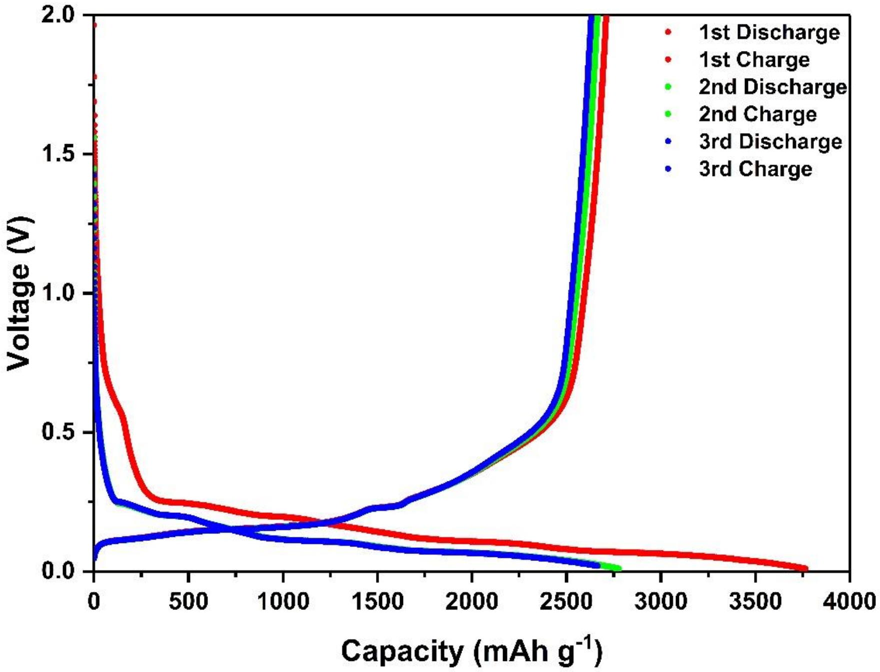

Figure 3.13 The voltage profiles of Cu/Si NFs anode in the first three cycles at 0.35 A g^{-1}.

The cycling performance of the alloyed Cu/Si core-shell NFs anode at 1.6 A g^{-1} and 3.2 A g^{-1}, and non-alloyed Cu/Si core-shell NFs anode at 3.2 A g^{-1} during their initial

500 cycles are shown in **Figure 3.14**. The non-alloyed core-shell NFs structures were reduced to Cu before the Si deposition for a comparison purpose. After initial cycles for the formation of SEI layer and activation of the active materials, the alloyed Cu/Si NFs anode exhibits a specific capacity of 1868 mAh g^{-1} and 1647 mAh g^{-1} at a discharge/charge current density of 1.6 A g^{-1} and 3.2 A g^{-1}, respectively. The capacity retention rates of these two current densities are about 66.6% and 65.1% from 6th to the 500th cycle, which is significantly higher than that of the non-alloyed Cu/Si core-shell NFs anode. This result highlights the benefits of alloyed Cu/Si core-shell nanostructure, which plays a significant role enhancing the reaction stability for anode electrodes.

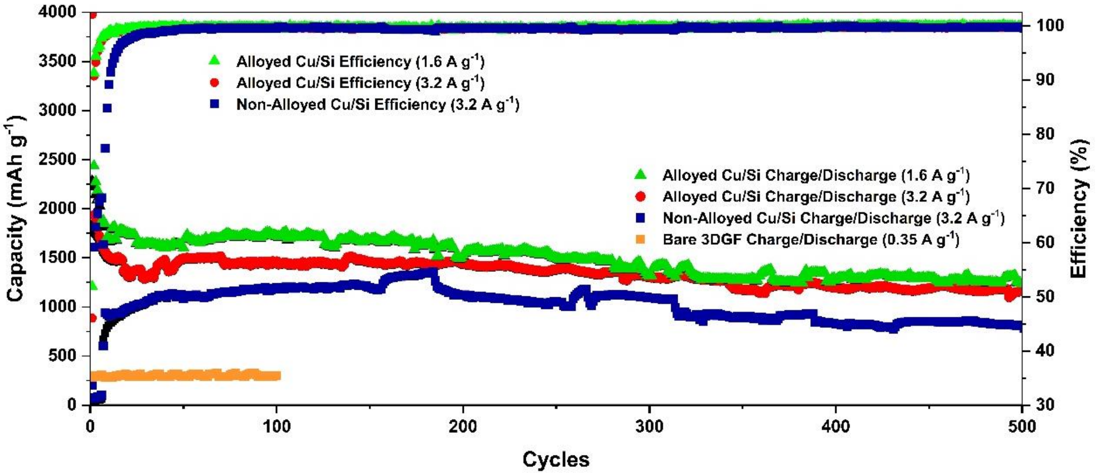

Figure 3.14 The cycling performance of alloyed Cu/Si anode with charge/discharge current density of 1.6 A g^{-1}, 3.2 A g^{-1} and non-alloyed Cu/Si anode with charge/discharge current density of 3.2 A g^{-1}.

The rate capability of alloyed Cu/Si core-shell NFs anode has been tested with an increase gradient of current density at 0.35 A g^{-1} , 1.8 A g^{-1}, 3.5 A g^{-1}, 7 A g^{-1}, 9 A g^{-1}, and 18 A g^{-1}, corresponding to the discharge capacities of 2087 mAh g^{-1}, 1315 mAh g^{-}

^{1}, 931 mAh g^{-1}, 592 mAh g^{-1}, 511 mAh g^{-1}, and 257 mAh g^{-1}, respectively (**Figure 3.15**). Remarkably, when the current density gradually decreases back to 1.8 A g^{-1}, the capacity retention remains 101%, 92%, 95%, 81.4%, and 77.7% corresponding to the discharging/charging current densities at 18 A g^{-1}, 9 A g^{-1}, 7 A g^{-1}, 3.5 A g^{-1}, and 1.8 A g^{-1}. This good rate performance and stability are likely due to the unique alloyed Cu/Si core-shell NFs structure that provides superior conductivity for the active materials. Another reason is probably related to the good conductivity of 3DGF as the flexible current collector in LIBs.

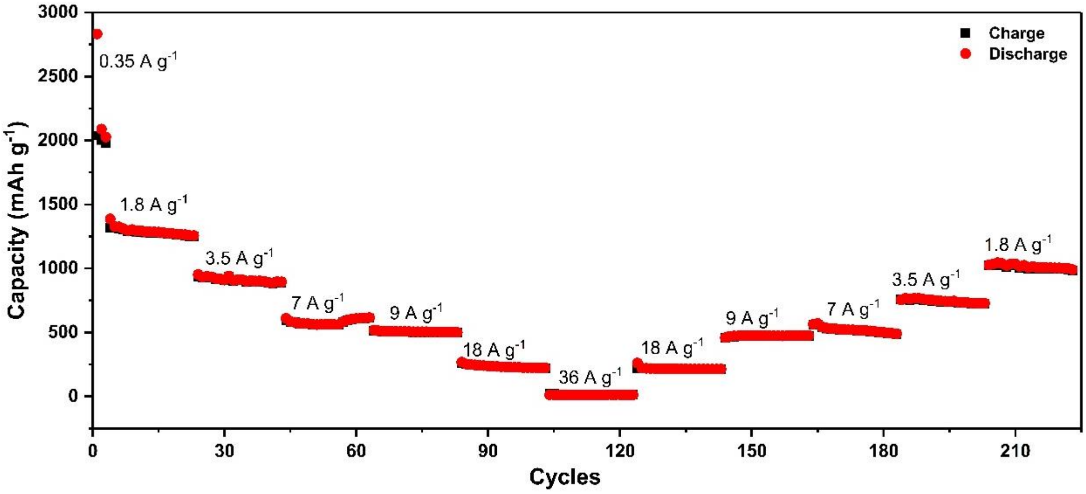

Figure 3.15 The rate performance of alloyed Cu/Si core-shell NFs anode.

Furthermore, the alloyed Cu/Si core-shell NFs anode exhibits an exceptional long-term cycle performance (**Figure 3.16**). There is a significant activation process observed in the initial 270 cycles[15], which includes a rapid capacity fading in the first 20 cycles, and a rising region in the subsequent 250 cycles that increase the capacity from 84 to 680 mAh g^{-1}. The capacity performance of the alloyed Cu/Si core-shell NFs anode sample achieves a high capacity retention (> 63 %) after 1000 runs at 10 A g^{-1} current density, compared with the highest capacity 680 mAh g^{-1} (at 270 cycles).

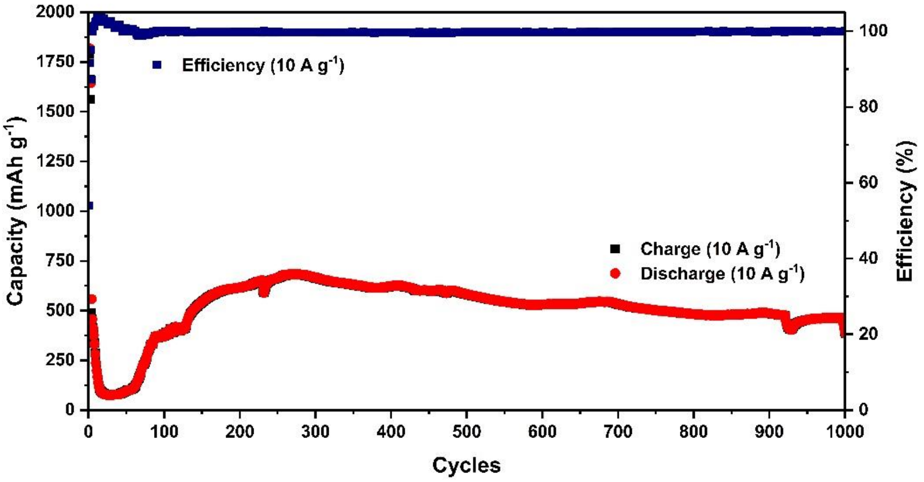

Figure 3.16 The long-term cycle performance of the alloyed Cu/Si NFs anode with a charge/discharge current density of 10 A g^{-1}.

To further assess the stability and mechanical strength of this Cu/Si core shell structure performed in LIBs, Cu/Si NFs on 3DGF electrode after 50 cycles at 1.6 A g^{-1} current density was examined under SEM (as shown in **Figure 3.17**). Compared with the pristine Cu/Si NFs electrode, it is interesting to note that the Cu/Si core shell NFs are well preserved on 3DGF after cycling. Moreover, we used Energy Dispersive Spectrometer (EDS) to characterize the cycled electrode sample. As shown in **Figure 3.18**, the C, O, F, Si, P, and Cu were detected in cycled Cu/Si NFs. The C, Si, Cu are contributed by the pristine Cu/Si NFs. O, F, and P are from the SEI and residual electrolyte.

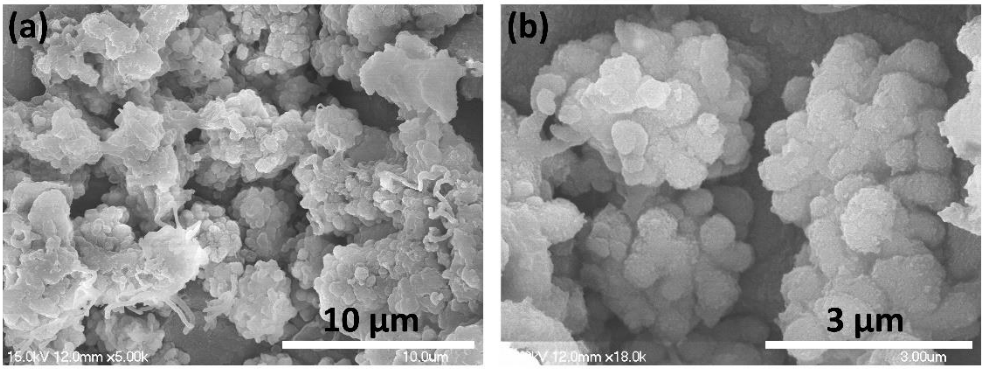

Figure 3.17 (a, b) Low- and high-magnification SEM characterization of the Cu/Si Core-Shell NFs on 3DGF after 50 cycles with a charge/discharge current density of 1.6 A g^{-1}.

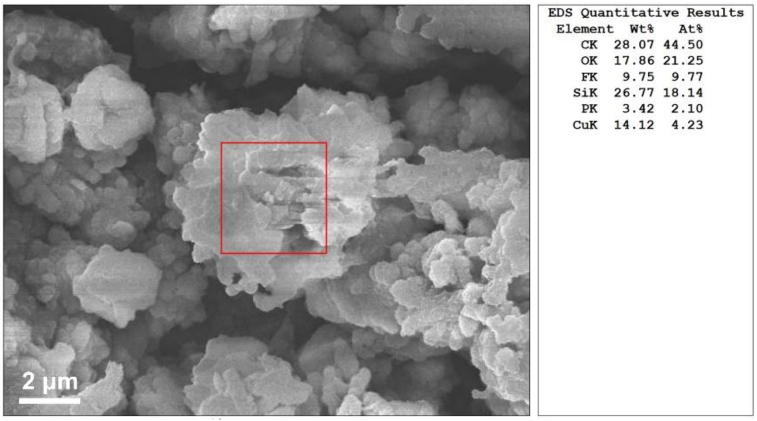

```
EDS Quantitative Results
 Element  Wt%    At%
     CK  28.07 44.50
     OK  17.86 21.25
     FK   9.75  9.77
    SiK  26.77 18.14
     PK   3.42  2.10
    CuK  14.12  4.23
```

Figure 3.18 SEM image and corresponding EDS quantitative elements table of the Cu/Si core-shell NFs on 3DGF after 50 cycles with a charge/discharge current density of 1.6 A g^{-1}.

This observation confirms the robust structural property of Cu/Si NFs, which is promising to relieve the stress and remain the structure after long cycling operations. Moreover, these unique NFs are still firmly anchored on the 3DGF during battery cycling, indicating a tight connection between Cu NFs with 3DGF. According to previous results, the achievement of high rate performance and long-term cycling stability of the alloyed Cu/Si anode could be ascribed to the alloyed Cu/Si core-shell NFs providing numerous fast pathways for lithium-ion during lithiation/delithiation processes. On the other hand, the 3DGF substrate acts as a significant role in supporting and holding the Cu/Si NFs to accommodate the contraction and expansion reversibly during the cycling process. This soft substrate could release the stress in Si to offer excellent mechanical stability for the whole electrode, which is an effective way to prevent the structural collapse and conductive loss after a long-term cycling [16].

3.3 Conclusion

In summary, we have demonstrated a facile method to fabricate a novel alloyed Cu/Si core-shell NFs anchored on the 3DGF structure as an anode in LIBs. This structure could be directly assembled to batteries without any conductive additive or binder. The electrochemical performance of this anode reaches a high capacity of 1869 mAh g^{-1} at 1.6 A g^{-1}, with a high retention rate of 66.6 % after 500 cycles. Even at a high current density of 10 A g^{-1}, this anode exhibits a superior high capacity retention >63% over the 500 cycles (compared with the highest capacity of 679 mAh g^{-1}). These improvements of electrochemical performance can be ascribed to the combination of flexible 3DGF and unique alloyed Cu/Si core-shell NFs. And this structure provides an effective strategy for next-generation Si-based flexible anodes in LIBs.

3.4 References

[1] M. D. Stoller, S. Park, Y. Zhu, J. An, and R. S. Ruoff, "Graphene-based ultracapacitors," *Nano letters,* vol. 8, no. 10, pp. 3498-3502, 2008, doi: 10.1021/nl802558y.

[2] K. S. Novoselov, A. K. Geim, S. V. Morozov, D. Jiang, Y. Zhang, S. V. Dubonos, I. V. Grigorieva, and A. A. Firsov, "Electric field effect in atomically thin carbon films," *Science (New York, N.Y.),* vol. 306, no. 5696, pp. 666-669, 2004, doi: 10.1126/science.1102896.

[3] P. Goli, H. Ning, X. Li, C. Lu, K. S. Novoselov, and A. A. Balandin, "Thermal Properties of Graphene–Copper–Graphene Heterogeneous Films," *Nano Letters,* vol. 14, no. 3, pp. 1497-1503, 2014, doi: 10.1021/nl404719n.

[4] Q. Yu, J. Lian, S. Siripongleri, H. Li, Y. P. Chen, and S.-S. Pei, "Graphene segregated on Ni surfaces and transferred to insulators," *Applied Physics Letters,* vol. 93, no. 11, p. 113103, 2008.

[5] S. J. Chae, F. Güneş, K. K. Kim, E. S. Kim, G. H. Han, S. M. Kim, H. J. Shin, S. M. Yoon, J. Y. Choi, and M. H. Park, "Synthesis of large-area graphene layers on poly-nickel substrate by chemical vapor deposition: wrinkle formation," *Advanced Materials,* vol. 21, no. 22, pp. 2328-2333, 2009.

[6] A. Reina, X. Jia, J. Ho, D. Nezich, H. Son, V. Bulovic, M. S. Dresselhaus, and J. Kong, "Large area, few-layer graphene films on arbitrary substrates by chemical vapor deposition," *Nano letters,* vol. 9, no. 1, pp. 30-35, 2008.

[7] K. S. Kim, Y. Zhao, H. Jang, S. Y. Lee, J. M. Kim, K. S. Kim, J.-H. Ahn, P. Kim, J.-Y. Choi, and B. H. Hong, "Large-scale pattern growth of graphene films for stretchable transparent electrodes," *nature,* vol. 457, no. 7230, p. 706, 2009.

[8] K. S. Novoselov, A. K. Geim, S. V. Morozov, D. Jiang, Y. Zhang, S. V. Dubonos, I. V. Grigorieva, and A. A. Firsov, "Electric field effect in atomically thin carbon films," *science,* vol. 306, no. 5696, pp. 666-669, 2004.

[9] D. A. Dikin, S. Stankovich, E. J. Zimney, R. D. Piner, G. H. Dommett, G. Evmenenko, S. T. Nguyen, and R. S. Ruoff, "Preparation and characterization of graphene oxide paper," *Nature,* vol. 448, no. 7152, p. 457, 2007.

[10] S. Park and R. S. Ruoff, "Chemical methods for the production of graphenes," *Nature nanotechnology,* vol. 4, no. 4, pp. 217-224, 2009.

[11] Y. Hernandez, V. Nicolosi, M. Lotya, F. M. Blighe, Z. Sun, S. De, I. McGovern, B. Holland, M. Byrne, and Y. K. Gun'Ko, "High-yield production of graphene by liquid-phase exfoliation of graphite," *Nature nanotechnology,* vol. 3, no. 9, pp. 563-568, 2008.

[12] Z. Chen, W. Ren, L. Gao, B. Liu, S. Pei, and H.-M. Cheng, "Three-dimensional flexible and conductive interconnected graphene networks grown by chemical vapour deposition," *Nature materials,* vol. 10, no. 6, p. 424, 2011.

[13] D. Yoon, H. Moon, H. Cheong, J. Choi, J. Choi, and B. Park, "Variations in the Raman Spectrum as a Function of the Number ofGraphene Layers," *Journal of the Korean Physical Society,* vol. 55, no. 3(2), pp. 1299-1303, 2009, doi: 10.3938/jkps.55.1299.

[14] M. T. McDowell, S. W. Lee, W. D. Nix, and Y. Cui, "25th anniversary article: Understanding the lithiation of silicon and other alloying anodes for lithium-ion batteries," *Adv Mater,* vol. 25, no. 36, pp. 4966-85, Sep 25 2013, doi: 10.1002/adma.201301795.

[15] J. Wang, Q. Zhang, X. Li, B. Zhang, L. Mai, and K. Zhang, "Smart construction of three-dimensional hierarchical tubular transition metal oxide core/shell heterostructures with high-capacity and long-cycle-life lithium storage," *Nano Energy,* vol. 12, pp. 437-446, 2015, doi: 10.1016/j.nanoen.2015.01.003.

[16] C. Yu, X. Li, T. Ma, J. Rong, R. Zhang, J. Shaffer, Y. An, Q. Liu, B. Wei, and H. Jiang, "Silicon Thin Films as Anodes for High-Performance Lithium-Ion Batteries with Effective Stress Relaxation," *Advanced Energy Materials,* vol. 2, no. 1, pp. 68-73, 2012, doi: 10.1002/aenm.201100634.

Chapter 4: Enhanced Electrochemical Performance by GeOx-Coated MXene Nanosheet Anode in Lithium-ion Batteries

Here, we demonstrate a facile method to synthesize an amorphous GeO_x-coated MXene nanosheet structure as the anode in lithium-ion batteries. By using the GeO_3^{2-} as the precursor, $NaBH_4$ as the reduction agent, we performed a one-step in situ synthesis of GeO_x nano particles coated MXene nanosheet composite. Due to the small size of the GeO_X nanoparticles on MXene nanosheet, this alternative structure provided a fast pathway for Li-ion interaction. Moreover, the MXene also serves as the excellent conductive additives to improve the electrochemical stability and electrical conductivity of composite because of its unique properties. It is indicated that the GeO_x/MXene nanosheet structure can significantly improve the stability during the lithiation/delithiation prosses, with the enhanced capacity by the improvement of processes' kinetics.

Furthermore, When the powder like active materials was using in the electrode, the slurry preparation is also a crucial step for the electrochemical performance in LIBs. The Li-PAA has been confirmed as a promising binder for the large-volume change alloy materials in electrodes, due to it exhibited better mechanical properties of elastomeric than polyvinylidene fluoride (PVDF) binder.[1] For the GeO_X based materials, the water-based lithium polyacrylate (Li-PAA) has been used for slurry preparation which demonstrated outstanding electrochemical performance.[2, 3] However, because of the solvent of water-soluble Li-PAA and water-insoluble PVDF is different. The dispersion of the active materials could exhibit distinct state in solvent, which different states were due to the hydrophilia of materials. Especially for the hydrophilic MXene based nanosheet, which hydrophilia properties solvent could lead to the distinct-different electrochemical properties when it was used in electrodes. These different of the electrochemical properties are worth to investigating.

Therefore, to further investigate the effect of solvent hydrophile in the preparation of slurry, we prepared two different types of electrode. One is prepared with Li-PAA binder and de-ionized (DI)-water solvent, another is prepared with PVDF binder and N-methyl pyrrolidinone (NMP) solvent. The electrode with PVDF binder and NMP solvent exhibited an excellent sustainable capacity of 381 mAh g^{-1} at 15 A g^{-1}. By contrast, the electrode with Li-PAA and DI-Water solvent demonstrate a reversible capacity of 950 mA h g^{-1} at 0.5 A g^{-1} after 100 cycles. The results showed that both combinations of binder and solvent have respective advantages in the different electrochemical properties, which could be ascribed to the different dispersion states in the two types of electrodes. To confirm the reason for these differences, we further investigated the electrochemical kinetics and structure of these electrodes, which demonstrated the distinct structure that led to the different electrochemical properties when the electrode was prepared by the different combinations of binder and solvent.

4.1 Experiment Section

4.1.1 Synthesis of MXene ($Ti_3C_2T_x$)

The MXene ($Ti_3C_2T_X$) was synthesized by etching precursor Ti_3AlC_2 (< 32 um) with LiF/HCl as reported previously.[4] Typically, LiF (2 g, Aladdin) and HCl (40 ml, 9 M, Sinopharm Chemical Reagent) were mixed by stirring in a Teflon beaker. Then, Ti_3AlC_2 powder (1 g) was slowly added into the mixture of the acid solution for 24 h at 35 °C. After the reaction, the resultant was washed with serval centrifugation-rinsing cycles (3500 rpm for 10 min) with DI-Water until the PH of the resultant solution is approaching to 6. Then, the washed resultant was dispersed in 40 ml of ethanol and kept under ultrasonic for 1.5 h. After this exfoliation process, the dark gray product was collected by centrifugation at 10000 rpm for 10 min. To get the finally dark green MXene supernatant, the dark gray product was re-dispersed in DI-water and kept under ultrasonic for 20 min, and then treated by 5 min centrifugation at 3500 rpm to separate the sediment.

To characterize the structure of MXene nanosheet, we use vacuum filtration to achieved free-standing and flexible MXene paper. As shown in **Figure 4.1**, the MXene paper exhibited a uniformly paper structure, which could be easily curved by a tweezer. **Figure 4.2** displays the SEM image of this MXene paper, a layer by layer structure with the thickness around 5 μm could be observed in **Figure 4.2b**. Because of the highly electrical conductivity of the MXene nanosheet, this layer by layer structure could provide a tight cross-link of each sheet, further improve the electrical conductivity of the whole structure. Finally, a high conductivity ~0.4 Ω/□ of this MXene paper was measured by the four probes system.

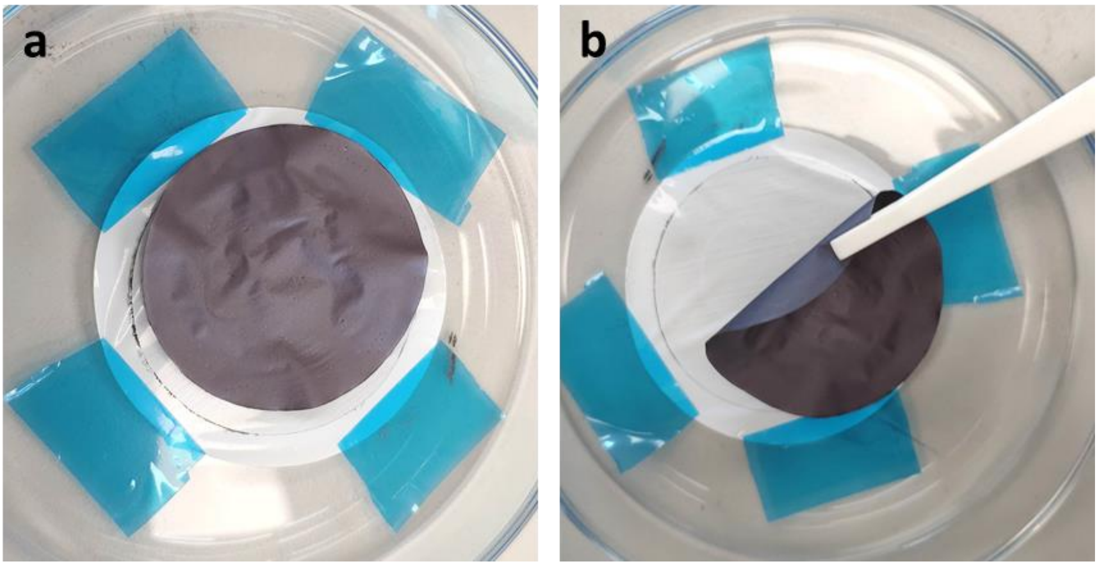

Figure 4.1 Optical image of the flat (a) and curved (b) MXene paper which is prepared by vacuum filtration.

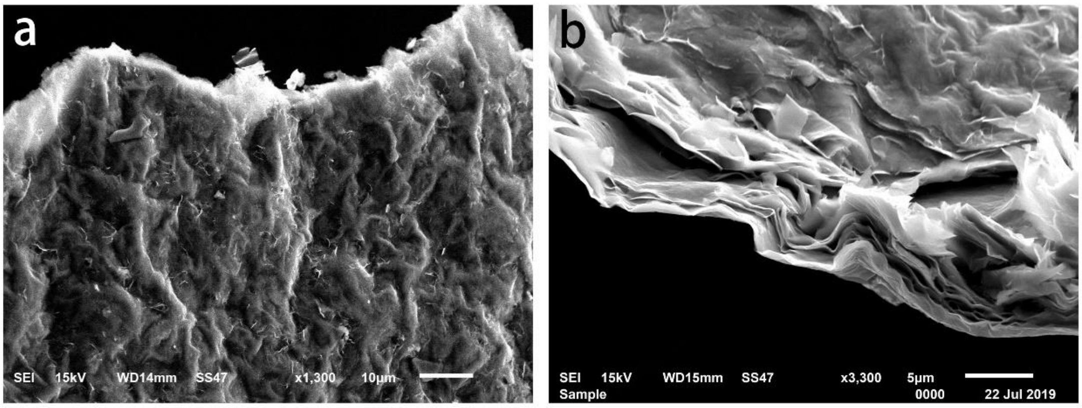

Figure 4.2 SEM image of the MXene paper which is prepared by vacuum filtration. (a) Top-view and (b) Cross-section.

To further investigate the proprieties of a single MXene nanosheet, the AFM was employed to measure the thickness of the MXene nanosheet. The sample was prepared by a simple drop of the MXene dispersion (0.05 mg/ml) on the silicon wafer. As shown in **Figure 4.3**, the thickness of the MXene nanosheet is estimated to be around 2.14nm, which confirmed the existing of the single MXene sheet.

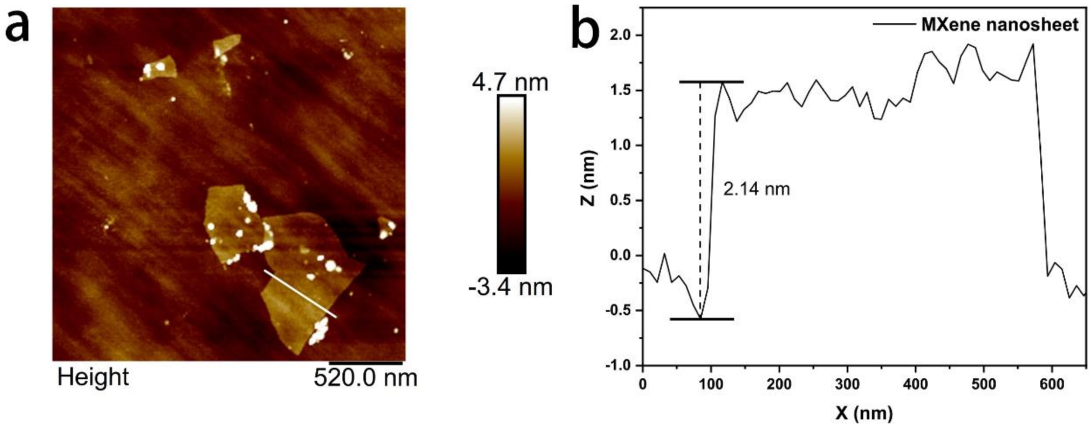

Figure 4.3 AFM images of the MXene nanosheet. (a) Hight map (b) Sheet thickness measure across the boundary of the nanosheet and silicon wafer. The thickness of the MXene nanosheet is estimated to be around 2.14nm.

4.1.2 Synthesis of MXene@GeOx

Firstly, 0.03 g Polyvinyl Pyrrolidone (PVP) was dispersed into 25 mL of the MXene dispersion (12 mg/ml) by ultrasonication. Meanwhile, 500 mg GeO_2 was added to 5 ml DI-water at 70 °C. Followed by adding the 2.5 ml ammonia (13.2 mol L^{-1}) into the GeO_2 suspension. After that, the GeO_2/ammonia mixture was quickly transferred to a transparent and clear solution. After that, this mixture was added to PVP/MXene dispersion with further ultrasonic treatment. Then, the $NaBH_4$ (0.9 g $NaBH_4$ adding into 20 mL DI-Water with ice-water bath was added into the above mixture solution by drop wise with magnetic stirring. After 12 h magnetic stirring, the dark-green suspension was obtained and then the resulting powder was collected by centrifugation and washed with ethanol several times. Finally, these collected powder was dried in the vacuum furnace at 60°C overnight. By contrast, the pure GeO_X was prepared by a similar approach, excluding the addition of MXene nanosheet.

Figure 4.4 shows the fabrication process of the GeO_X/MXene nanosheet composite. The GeOX/MXene was prepared by a one-pot method that only involves one chemical reaction. The PVP was firstly dissolved in the as-prepared MXene ($Ti_3C_2T_X$) aqueous dispersion by ultrasonication. Then the GeO_3^{2-} precursor solution was prepared by the reaction between ammonia and GeO_2. After that, this GeO_3^{2-} precursor solution was added into the MXene and GeO_X solution under stir to produce a uniform dispersion which contains the GeO_3^{2-}, MXene, and PVP. The reduction agent $NaBH_4$ was following drop-wise into the above dispersion, in which, $NaBH_4$ could in-situ reduce the GeO_3^{2-} to GeO_X on the MXene nanosheet. In this reaction, the PVP act as a capping ligand to provide a limitation of the size of nanoparticles, further assisted the formation of small size GeO_X nanoparticle which anchored on MXene nanosheet (GeO_X/MXene).

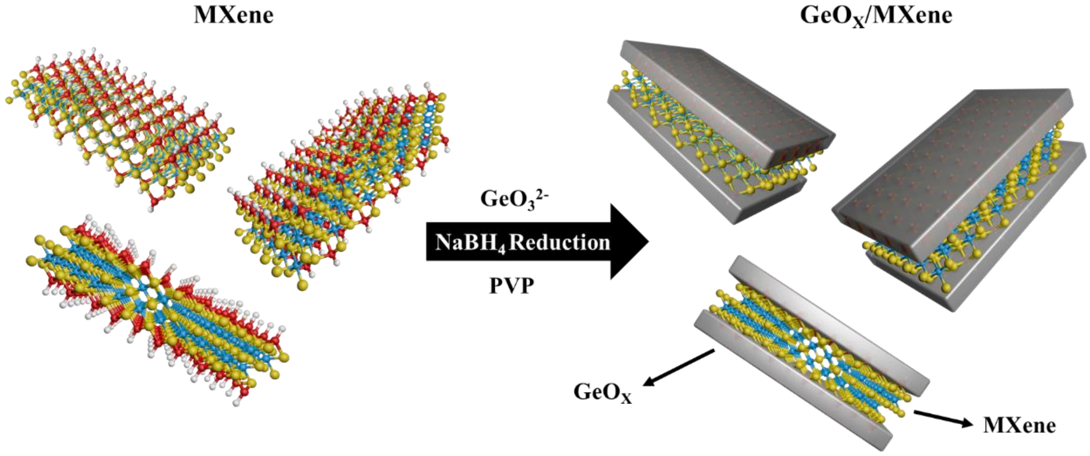

Figure 4.4 The schematic diagram for the fabrication of the GeO_X/MXene nanosheet composite.

4.1.3 Structural Characterization

The microstructure and morphologies of the achieved sample were obtained by the high-resolution transmission electron microscopy (HR-TEM, FEI Tecnai G2 F30) and field-emission scanning electron microscopy (FE-SEM, Hitachi S-4800). The crystal structure of resultant materials was characterized by a Bruker Advance D8 (Cu Ka) XRD from 3 to 80 ° at 5 deg min^{-1}. The X-ray photoelectron spectroscopy (XPS) patterns were measured by Thermo scientific ESCALAB 250Xi with Al Ka X-ray source. The thermogravimetric (TG) curve was determined by the TA Instruments SDT2960 from room temperature to 1200 °C with the heating rate of 10 °C min^{-1} under the argon atmosphere.

4.1.4 Electrochemical Measurements

The electrochemical performance of the GeO_X/MXene and GeO_X were performed by using coin cells with CR2032-type. For the preparation of two types of slurry, the achieved GeO_x/MXene samples were firstly mixed with different binders (PVDF and Li-PAA) and conductive additive Super-P with a weight ratio of 8:1:1, while the NMP and DI-water were respective used for PVDF and DI-water as the solvent. This slurry was then coated on the copper foil followed by drying at 60 °C for 10 h. The electrodes with 13mm diameter were punched from the dried slurry/copper foil. The lithium metal was used for the negative electrode. The coin cells were assembled in an argon-filled glove box (H_2O, O_2 <0.2 ppm). Each cell was composed of a GeO_x/MXene electrode, Celgard 2325 separator, lithium metal negative electrode, and 1M $LiPF_6$ in a solution mixture of DMC and EC (1:1 vol%) electrolyte. The CV test with the scanning rate of 0.1 mV s^{-1} was measured on a Metrohm Autolab PGSTAT302N electrochemical workstation. For the galvanostatic cycling test of batteries, the Neware BTS-4000 multichannel batteries test system was used with a cut-off voltage between 0.01 V and 1.2 V. On average, the mass loading of the whole electrode was about 1.2 mg cm^{-2} According to the different preparation of slurry, the electrode samples were labeled with the different abbreviations. GeOx/MXene/PVDF (NMP) and GeOx/PVDF (NMP) represent the GeOx/MXene and pure GeOx electrode with PVDF binder and NMP solvent. GeOx/MXene/Li-PAA (DI-water) and GeOx/Li-PAA (DI-water) represent the GeOx/MXene and pure GeOx electrode with Li-PAA binder and DI-water solvent.

4.2 Structure Characterization of MXene/GeO_X

The morphologies and structures of the as-prepared sample were characterized as shown in **Figure 4.5**. The SEM images (**Figure 4.5a** and **Figure 4.5b**) show the GeO_x/MXene nanosheets dispersed on the substrate. The GeO_x are uniformly coated on the MXene, without unexpected agglomeration and damage of the original structure for MXene sheets. To further determine the nanostructure of GeO_X, the atomic force microscope (AFM) images of the GeO_x/MXene nanosheets was shown in **Figure 4.5f**. In which, the GeOx demonstrated the structure of nanoparticles that anchored on the MXene nanosheet. The diameter and thickness of the GeO_x nanoparticles were measured around 50nm and 20nm, respectively (**Figure 4.5g**), which nanostructure of particles can significantly improve the contact surface between active materials with the electrolyte, as well as provide more and fast pathways for Li-ion insertion. Moreover, the alternative composite structure can be confirmed by TEM in **Figure 4.5c** and **Figure 4.5d**. In **Figure 4.5c**, shows the slightly stacked GeO_x/MXene nanosheets appear well distributed in the field of view. The high-resolution TEM image of GeO_x/MXene (**Figure 4.5d**) further demonstrates that the amorphous GeO_x is intimately coated on the MXene film, with the distinct layered structure of the MXene sheets. The distribution of the GeO_x on MXene nanosheets was confirmed by the EDS mapping of the as-obtained GeO_x/MXene nanosheet (**Figure 4.5e**), which shows a uniform distribution of Ti, C, Ge, O on the composites, indicating the uniform growth of the GeO_x on the MXene sheets by the self-assembly processes and in-situ reduction.

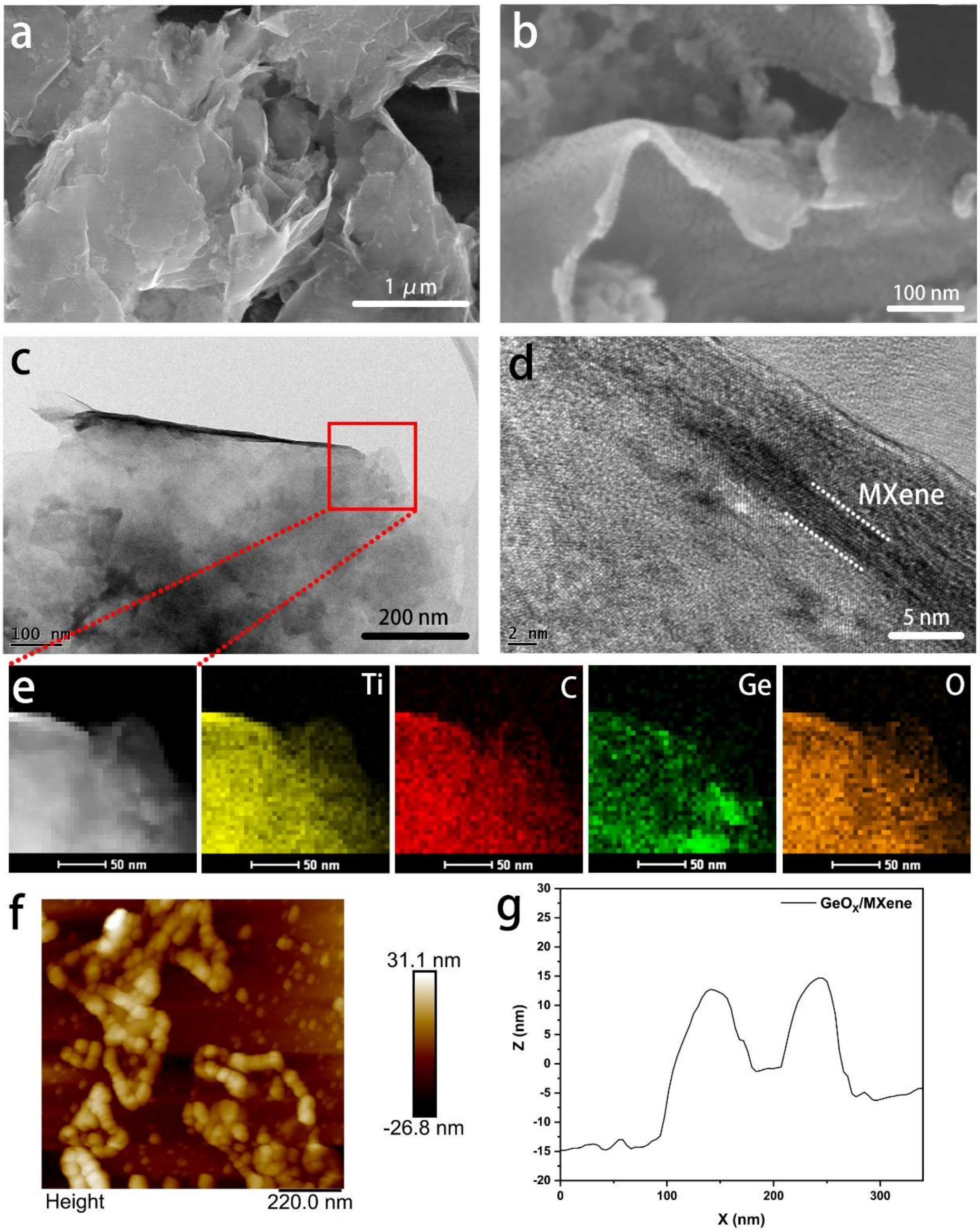

Figure 4.5 Morphologies, EDS mapping images, AFM images, and pore size distribution of the GeO_X/MXene nanosheet structure: (a and b) Field emission SEM, (c) TEM, and (d) High-resolution TEM images; (e) EDS mapping images of Ti, C, Ge, and O; (f-g) AFM images of the GeOX/MXene nanosheet. (f) Hight map (g) the diameter and thickness of GeOX nanoparticles.

To validate the surface textures and nanostructure of the GeO_x/MXene nanosheet, the nitrogen adsorption isotherms and pore size distribution and shown in **Figure 4.6a** and **Figure 4.6b**. The specific surface area (SSA) of the MXene and GeO_x/MXene nanosheet were obtained by Brunauer–Emmett–Teller (BET) method are 41.47 m^2 g^{-1} and 124.88 m^2 $g^{-1,}$ respectively. The significant increment of the SSA in GeO_x/MXene is attributed to the uniformity coated of GeO_x on the MXene. In **Figure 4.6b**, the pore size distribution of GeO_x/MXene demonstrates a wide range from 1.8 to 50nm, which is confirmed the size of GeO_X nanoparticles in the composite, as supported by the above characterization.

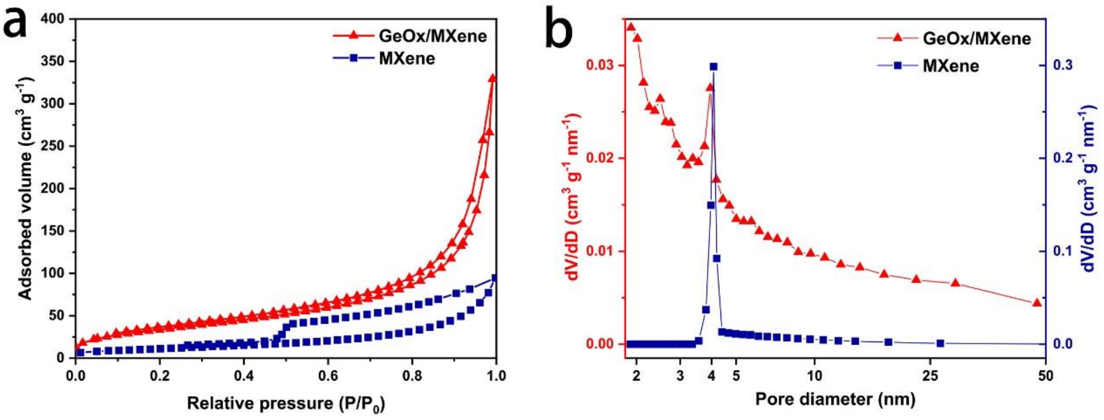

Figure 4.6 (a) Nitrogen adsorption isotherms and (b) Pore size distribution of GeO_X/MXene and pure MXene sample.

The amorphous feature of GeO_x could be further confirmed by the XRD patterns (**Figure 4.7g**). For the GeO_x/MXene composite, there are only two sharp diffraction peaks locating at 4 ° and 60.1 °, attributed to the MXene (002) and (110) . After a simple heat-treatment at 700 °C under Ar for 2 hours, several new sharp diffraction peaks were observed in the pattern, which is ascribed to the GeO_x decomposing to Ge and GeO_2 at 700 °C. These peaks are associated with crystalline planes of GeO_2 (101), (112), (113) (JCPDS #65-0862) and Ge (111), (220), (311), (400), (311) (JCPDS #65-0333), respectively. Since pure GeO_2 or Ge are the consequence of the heat-treatment, it demonstrates that oxidation species of germanium in the composite is amorphous GeO_x (where x smaller than 2). As can be seen in **Figure 4.7b-d**, the XPS spectra of Ti 2*p*, Ge 3*d* and O1*s* for GeO_x/MXene composite provide more information of the chemical environment of the composite. **Figure 4.7b** shows the Ti 2*p* spectrum of the GeO_x/MXene composite, in which, the Ti-C, Ti^{2+}, and Ti^{3+} peaks are consistent with the previous report.[5] It demonstrates that the growth process of GeO_x is mild and the MXene structure remains intact after GeO_x Growth. The chemical state of the GeOx could be confirmed by Ge 3*d* spectrum (**Figure 4.7c**). In this figure, 4 peaks at 29.3, 31.1, 32.0, and 32.6 eV are fitted, corresponding to Ge^0, Ge^{2+}, Ge^{3+}, and Ge^{4+}, respectively.[6] The peak centered at 29.4 eV confirms the existence of Ge^0 in the particles. The main peak, at 32.5eV is fitted to the three peaks at 31.1, 32.0, and 32.6 eV corresponding to Ge^{2+}, Ge^{3+}, and Ge^{4+}. The peak area calculation of this Ge 3*d* spectrum indicates that the surface of GeO_x consists of Ge^0 (6.02 %), Ge^{2+} (3.98 %), Ge^{3+} (36.77 %), and Ge^{4+} (53.21 %). The G:O stoichiometry ratio of 1:1.65 was determined by the Ge 3*d* spectrum, which confirmed the moderate oxidation of GeO_X. Moreover, the XPS spectrum of O 1*s* (**Figure 4.7d**) implies the composition of GeO_x with MXene. The Ti-O, Ti-C-O_x, Ti-C-OH, Ge-O, and absorbed H_2O could be well determined in the spectrum.

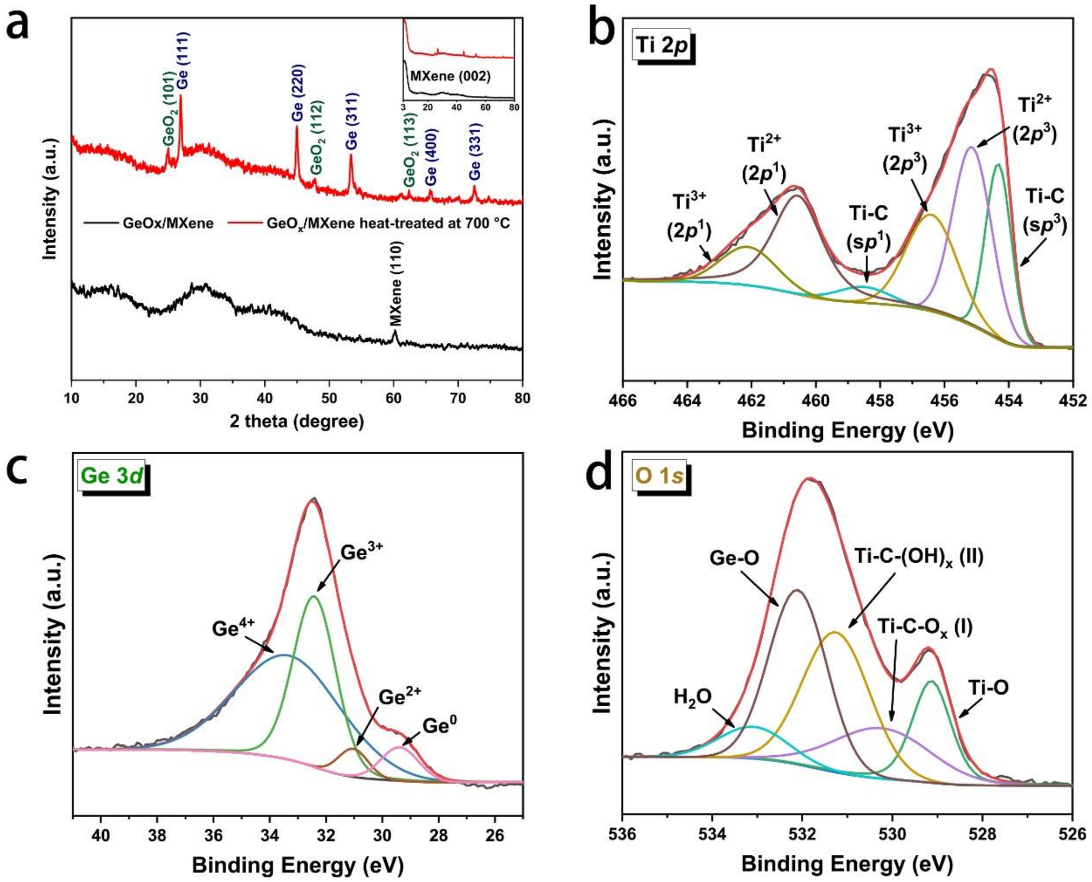

Figure 4.7 (a) XRD pattern of GeO_X/MXene; XPS of (b) Ti 2*p*, (c) Ge 3*d*, and (d) O 1*s* spectrum of the GeO_X/MXene nanosheets.

To determine the content of GeO_x in the composite, the weight of the composite (pristine MXene with the reduced GeOx) was recorded after dried in vacuum furnace. The content of GeO_x could be simply calculated by the difference in weight of pristine MXene and the GeO_x/MXene composite. To ensure an accurate result, this experiment was repeated several times and the GeOx content in GeO_X/MXene was calculated to be in the range of 40–43 %. In **Figure 4.8**, the black TG curve of the GeO_X/MXene shows a sharp decrease in weight (38.86%) when the temperatures increased from 700 to

850 °C, which is related to the decomposition of the GeO_x.[3]

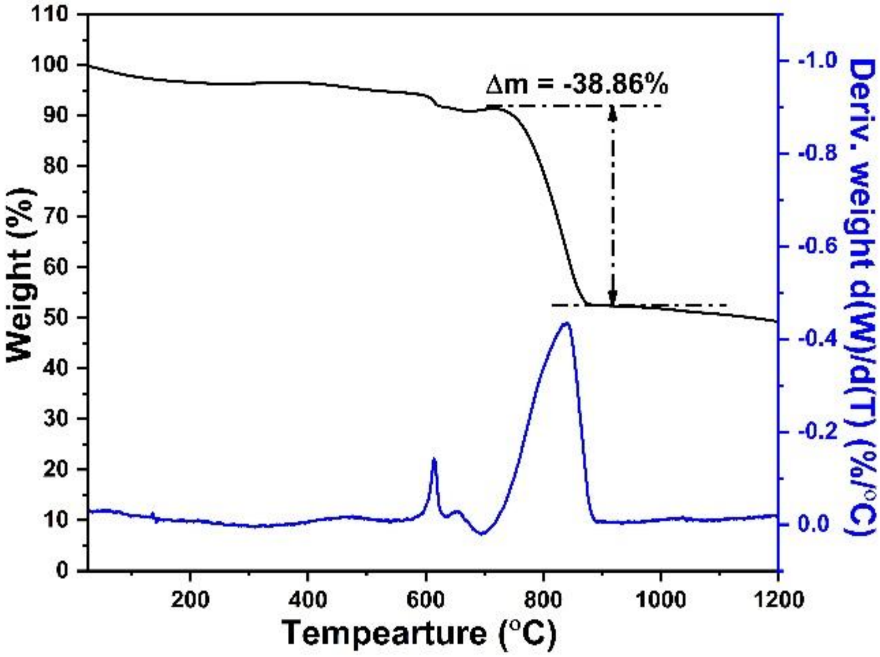

Figure 4.8 TGA curves of GeO_X/MXene.

4.3 Electrochemical Performance of GeOx/MXene Electrode

Figure 4.9 - Figure 4.14 displays the electrochemical performance of the GeOx/MXene electrode. The CV curves tested of GeO_X/MXene/Li-PAA (DI-water) in the voltage of 0.01 V – 1.2 V with scan rate 0.1 mV s^{-1} was plotted in **Figure 4.9a**. For the first lithiation of the GeOx/MXene, the small current increasing start from 1.0 V is related to the formation of SEI between the active materials with the electrolyte. This formation of the SEI layer results in low Coulombic efficiency in the first cycle.[7] With the continue of lithiation, a peak appears around 0.4 V is associated with the deoxidation of GeO_2. Finally, a sharp peak occurs from 0.3 V to 0.01 V resulting from

the alloying of Li with Ge to form Li$_X$Ge. In the oxidation curve, the peak at 0.45 V and are assigned to the delithiation of Li-Ge alloy.[3] These peaks are also observed on the following cycles, indicating the stable reaction pathway for the lithiation process of GeOx/MXene composite. **Figure 4.9b** shows the first three CV curves of GeO$_X$/MXene with PVDF binder and NMP solvent (GeO$_X$/MXene/PVDF (NMP)), which shapes are similar to the GeO$_X$/MXene/Li-PAA (DI-water) except for the first lithiation step. The GeO$_X$/MXene/PVDF (NMP) demonstrates a large current during the formation of SEI, which probably due to the increasement of contact area between active materials and electrolyte when the hydrophilic materials are uneven dispersion in the hydrophobic solvent. This result would be further confirmed and investigated in the following discussion.

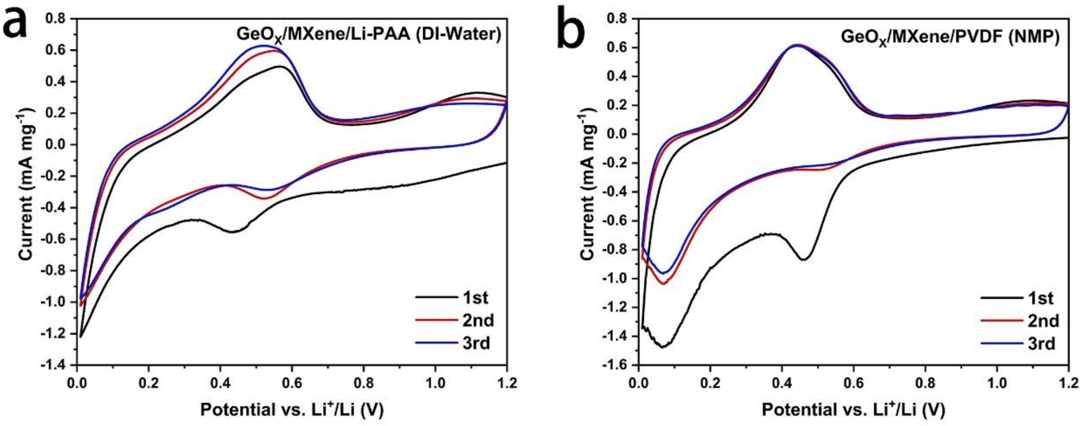

Figure 4.9 the first three cyclic voltammetry (CV) curves of GeO$_X$/MXene/Li-PAA (DI-water) (a) and GeO$_X$/MXene/PVDF (NMP) (b) between 0.01V-3V with the scan rate of 0.1mV s^{-1}; (b) the first three cyclic voltammetry (CV) curves of GeO$_X$/MXene/PVDF (NMP) between 0.01V-3V with the scan rate of 0.1mV s^{-1}.

Figure 4.10a shows the charge/discharge curves of the GeO_X/MXene/Li-PAA (DI-water) at a current density of 200 mA g^{-1} of current density in a voltage window from 0.01 V to 1.2 V.[8] A capacity of approximately 2102 mAh g^{-1} (corresponding to the mass of GeOx) is exhibited in the discharge of the first cycle. In comparsion, the pure MXene nanosheet without GeO_X coating exhibits in a capacity of only 35 mA g^{-1} in the control experiment (**Figure 4.11**). Therefore, the mass of GeO_X is approximately used for the calculation. It is clear that a significant drop of capacity for the second and the further cycles is observed. This irreversible capacity loss is probably attributed to the irreversible formation of Li_2O and SEI layers on the GeO_x/MXene nanosheets during the first lithiation.[9, 10] After few cycles to stabilize the active materials, the shape of the 10th charge–discharge curve is similar to the 30th cycle, revealing a good cycling stability of this GeO_x/MXene nanosheets. **Figure 4.10b** shows the charge/discharge curves of the GeO_X/MXene/PVDF (NMP), which exhibits the same charge and discharge characteristics with **Figure 4.10a**. Moreover, the capacity of the first discharge curve is larger, which indicates to the more formation of SEI, which could be corresponding to the CV curves in **Figure 4.9b**.

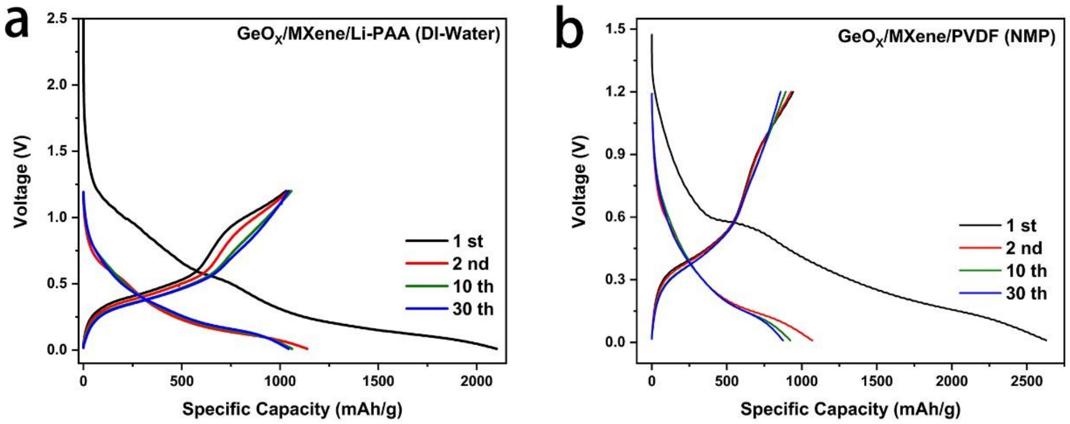

Figure 4.10 The cyclic voltammetry (CV) curves of GeO$_X$/MXene/Li-PAA (DI-water) (a) and GeO$_X$/MXene/PVDF (NMP) (b) between 0.01V-3V with the scan rate of 0.1mV s^{-1}.

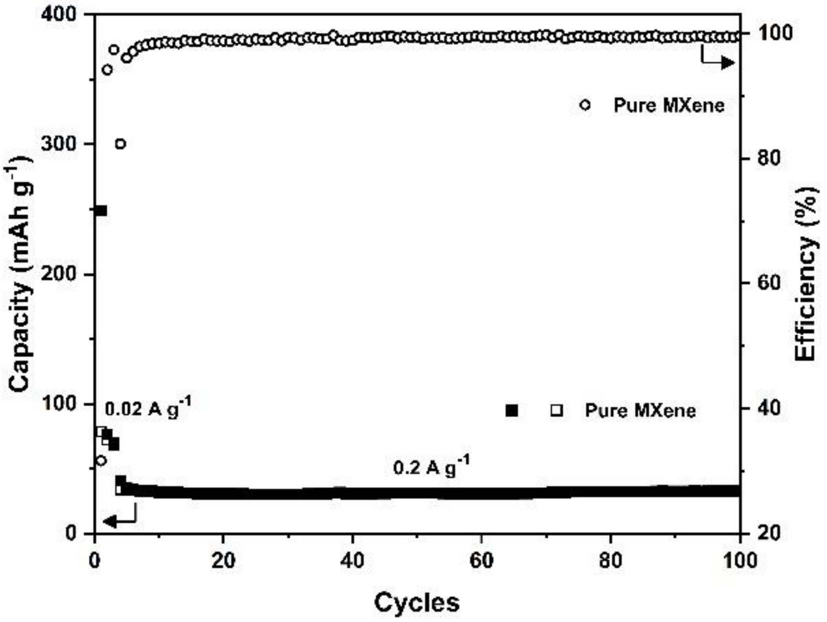

Figure 4.11 Cycling performance of pure MXene with charge/discharge current density of 0.2 A g^{-1}.

The cycling performance of the GeO_X/MXene and GeO_X anodes with different binders and solvent under the current density of 0.2 A g^{-1} and 0.5A g^{-1} is shown in **Figure 4.12**. In the cycling performance with the current density of 0.2 A g^{-1} (**Figure 4.12a**), the GeO_X/MXene/Li-PAA (DI-water) and GeO_X/MXene/PVDF (NMP) demonstrates the discharge capacity of 1138 mA h g^{-1} and 1070 mA h g^{-1} in the second cycle and retains 1026 mA h g^{-1} and 826 mA h g^{-1} after 50 cycles respectively. Both electrodes demonstrate a good capacity retention in this current density due to the combination of MXene and GeO_X. By comparison, the GeO_X anode alone exhibits a discharge capacity of 1015 mA h g^{-1} in the second cycle and retains 438 mA h g^{-1} after 22 cycles, the retention (43.2 %) of discharge capacity is much lower than that of the GeO_X/MXene/PVDF (NMP) (77.2 %) and GeO_X/MXene/PVDF (DI-water) (90.2 %). This extraordinary performance highlights the importance of the addition of the MXene structure. The flexible MXene structure nanosheet structure can significantly release the stresses accumulated during the lithiation process of GeO_X, eventually enhancing the reaction stability of the active materials. When the current density increased to 0.5 A g^{-1} (**Figure 4.12b**), GeO_X/MXene/Li-PAA (DI-water) achieved excellent cycling stabilization, corresponding to the discharge capacity of 1078 mA h g^{-1} in 5th cycles and retains 950 mA h g^{-1} after 100 cycles. Which indicated the tough structure of the GeO_X/MXene anode when using the Li-PAA binder and DI-water solvent in the slurry preparation. The uniformly dispersed of the hydrophilic GeO_X/MXene nanosheet in DI-water lead to a tight crosslink of that with Li-PAA binder in electrode, provide a significant improvement of the electrochemical stability. By comparison, the capacity of GeO_X/MXene/PVDF (NMP) demonstrates a sequential decline of the capacity with this current density. That probably due to the porous structure was appeared in electrode structure when the hydrophilic GeO_X/MXene is agglomerate in the hydrophobic NMP solvent. This porous structure cannot satisfy the huge stress effect during the lithiation of GeO_X, further lead to the rapid capacity fading.

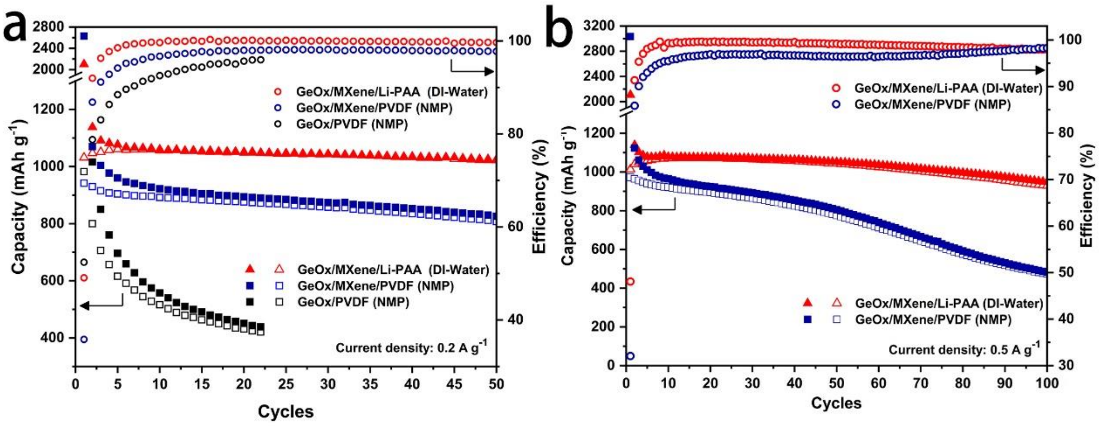

Figure 4.12 Cycling performance of GeO_X/MXene and GeO_X anodes with charge/discharge current density of 0.2 A g^{-1} (a) and 0.5 A g^{-1} (b).

Figure 4.13 shows the rate capability of the GeO_X/MXene anode under the increasing current density. For the GeO_X/MXene/Li-PAA (DI-water), the discharge capacities of that reach 1191, 1049, 901, 776, 482, and 261 mAh g^{-1} at different current densities from 0.2, 1, 3, 5, 10 to 15 A·g^{-1}. When the current density resets to 1 A·g^{-1}, the specific capacity can recover to 1046 mAh·g^{-1}, and still remain the excellent capacity stability in further dozens of cycles. These results indicate this GeO_X/MXene nanosheet structure with excellent rate capability, which is ascribed to the cross-linked MXene nanosheets acts as a conductive network that providing superior conductivity for the active materials in the electrode. Moreover, the ultrasmall of GeOx nanoparticles facilitates a fast pathway for lithiation and delithiation processes. For the GeO_X/MXene/PVDF (NMP), the discharge capacities of that are slightly behind the GeO_X/MXene/Li-PAA (DI-water) in the current densities from 0.2 to 5 $A \cdot g^{-1}$. However, when the current density increases to 10 and 15 $A \cdot g^{-1}$, the rate capability of that demonstrate a better result corresponding to the capacity of 381 mAh g^{-1} at 15 $A \cdot g^{-1}$. This could be ascribed to the porous of electrode structure allowed the fast through of Li-ion, moreover, this structure causes more active materials are exposed to the electrolyte, which produces the larger number of active sites for Li-ions. In contrast, as shown in **Figure 4.18**, the GeO_X/MXene anode demonstrates a tightly and compact structure when it disperses in the DI-water based slurry. This compact structure relatively blocks the Li-ion pathway and close the active sites for Li-ions, which slightly reduce the rate capability in electrochemical energy storage.

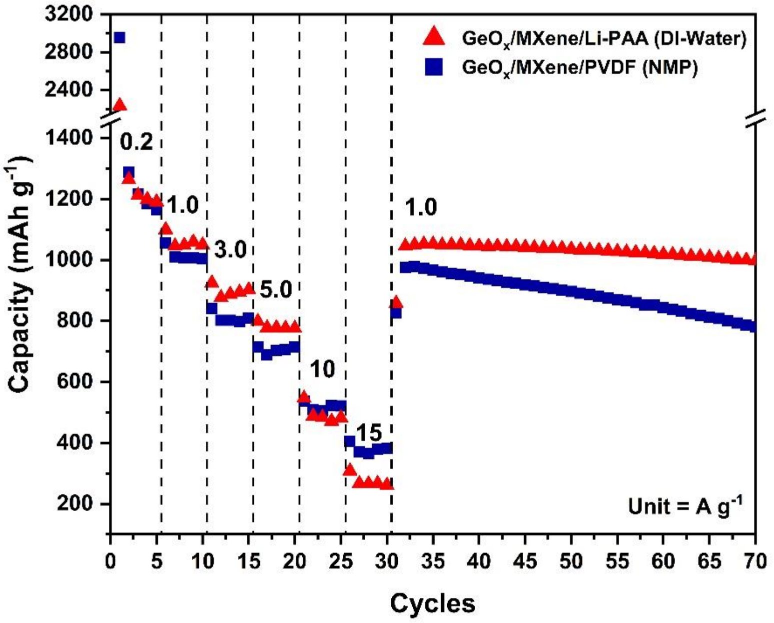

Figure 4.13 Rate performance of GeOx/MXene with current densities from 0.2 to 15 A g^{-1}.

Figure 4.14 displays the charge/discharge profiles of the GeOx/MXene/Li-PAA (DI-water) and GeOx/MXene/PVDF (NMP) in the various current densities. With increasing current density, the level of distinct polarization becomes more pronounced. However, the discharge plateaus from 0.35 to 0.01 V still remain when the current density increases to a high rate of 15 A·g^{-1}, suggesting that GeOx/MXene composite offer stable permeability for Li-ion transfer and excellent electrical conductivity with a wide range of current rates.

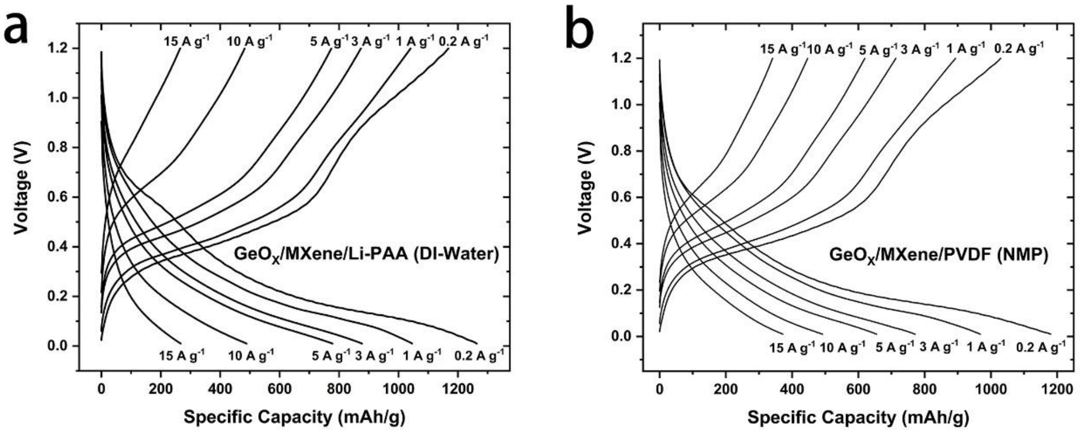

Figure 4.14 The galvanostatic charge-discharge curves of GeO$_X$/MXene/Li-PAA (DI-water) (a) and GeOX/MXene/PVDF (NMP) (b) with current densities from 0.2 to 15 A g^{-1}.

Overall, the resulted excellent rate performance of GeO$_x$/MXene should be ascribed to the uniform growth of the GeO$_x$ nanoparticles on the MXene nanosheet, which provides fast pathway for both of electron and ion during lithiation and delithiation processes. Moreover, the GeO$_x$/MXene display the different features when the electrode was prepared with different combinations of binder and solvent. The hydrophobic NMP solvent would make the electrode present a nonuniform and porous structure, which could provide more surface area to allow the Li-ions through into the electrode then interact with the active materials. But this porous structure probably too weak to endure the huge stress effect during the lithiation of GeOx. Contrarily, the electrode prepared with DI-water solvent own tightly structure to prevent the pulverization of the whole electrode, demonstrates an excellent cycle stabilization. But this compact structure limits the free shuttle of the Li-ions, which leads to a decrease of rate performance. The further investigation of the electrode's properties would be displayed in **Figure 4.15** - **Figure 4.20**.

4.4 Electrochemical Kinetics of GeO$_X$/MXene Electrode

The electrochemical kinetics of GeO$_X$/MXene anode with different binder and solvent in lithium storage could be investigated by using a series of CV curves with various scan rates from 0.1 to 1 mV s^{-1} (**Figure 4.15**). Typically, the current (i) versus scan rate (v) should follow the equation (4.1) and (4.2) [11]

$$i = av^b \qquad (4.1)$$

$$\log(i) = b\log(v) + \log(a) \qquad (4.2)$$

In this equation, the value b could be obtained by the slope of log(i) versus log(v). if b is 0.5, it is suggested that the diffusion-controlled process dominates in the electrochemical storage, while if b is equal to 1, a capacity behavior plays a more important role.

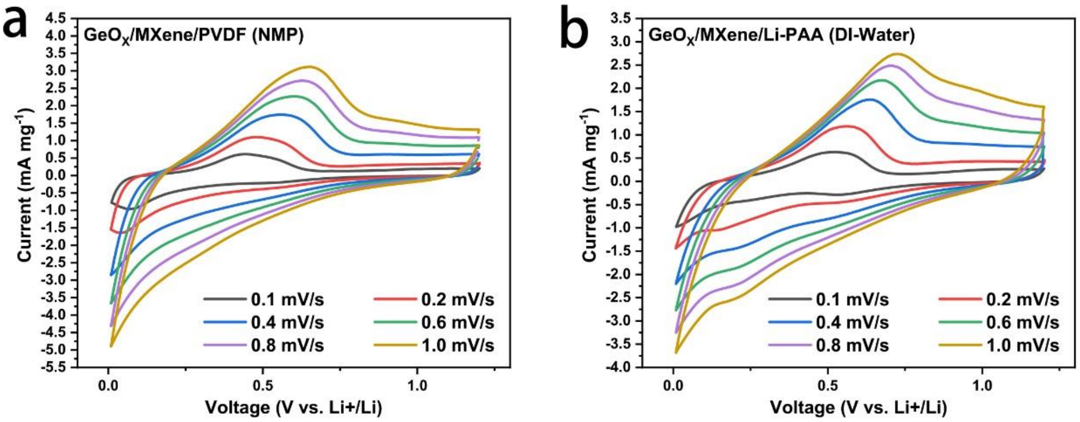

Figure 4.15 The CV curves of the GeOX/MXene/PVDF (NMP) (a) and GeOX/MXene/Li-PAA (DI-water) (b) with different scan rates from 0.1 to 1 mV s^{-1}.

When plotting the log(v) with scan rate and log(i) of GeOx/MXene from 0.1 to 1 mV s^{-1}, a linear relationship was observed in **Figure 4.16**. For the GeOX/MXene/PVDF (NMP), the parameter b was calculated as 0.71/0.70 according to reduction/oxidation peaks, which indicates the synergistic effect of diffusion-controlled and capacitance-controlled behaviors in electrochemical energy storage, indicate the GeOx/MXene nanosheet provides abundant fast pathway for ion diffusion. For GeOX/MXene/Li-PAA (DI-water), the parameter b is slightly smaller than the above result, corresponding to 0.58/0.60 during reduction/oxidation processes. The lower of parameter b means the electrode exhibit more diffusion-controlled behavior, which confirms the compact structure of the electrode limit the anchor of Li-ions on the surface of active materials.

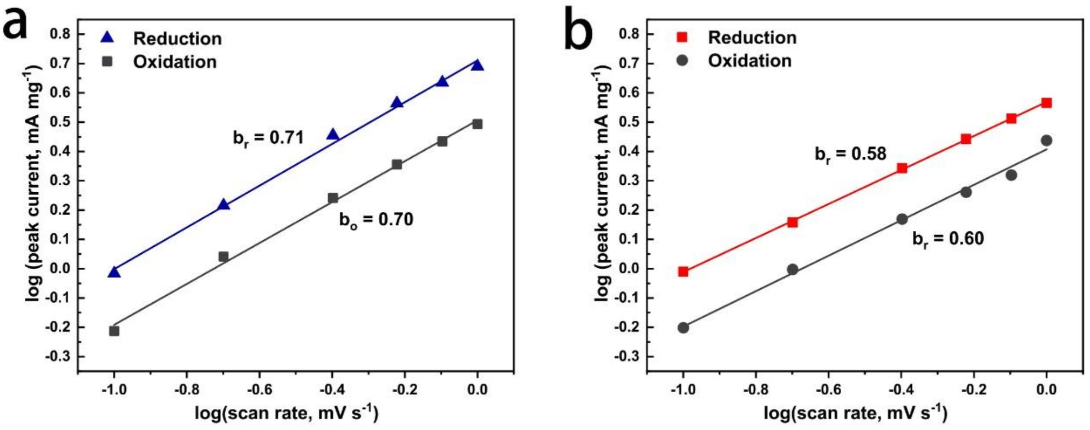

Figure 4.16 The log(v) versus log(i) curves and determined b-values based on the reduction peaks for GeOX/MXene/PVDF (NMP) (a) and GeOX/MXene/Li-PAA (DI-water) (b).

The capacitance and diffusion contribution ratios of the GeOx/MXene could be further quantified by splitting the current response (i) to diffusion-controlled insertion ($k_2 v^{1/2}$)

and capacitive reactions $(k_1 v)$ via the following equations[12]

$$i(v) = k_1 v + k_2 v^{1/2} \tag{4.3}$$

$$i(v)/v^{1/2} = k_1 v^{1/2} + k_2 \tag{4.4}$$

The constants of k_1 and k_2 could be calculated by plot $v^{1/2}$ versus $i(v)/v^{1/2}$ with different response current and the scan rate. Finally, by computing k_1 and k_2, the contribution ratio of diffusion-controlled insertion $(k_2 v^{1/2})$ and capacitive reactions $(k_1 v)$ could be determined, as shown in **Figure 4.17**. When the sweep rate increases from 0.1 to 1 mV s^{-1}, the capacitive-controlled proportion of the GeO_X/MXene/PVDF (NMP) approaches to a maximum value of 65%. By comparison, the capacitive-controlled proportion for GeO_X/MXene/Li-PAA (DI-water) displays around 10% smaller than the above result. This difference further supports the difference of rate capability for two types electrode in **Figure 4.13**.

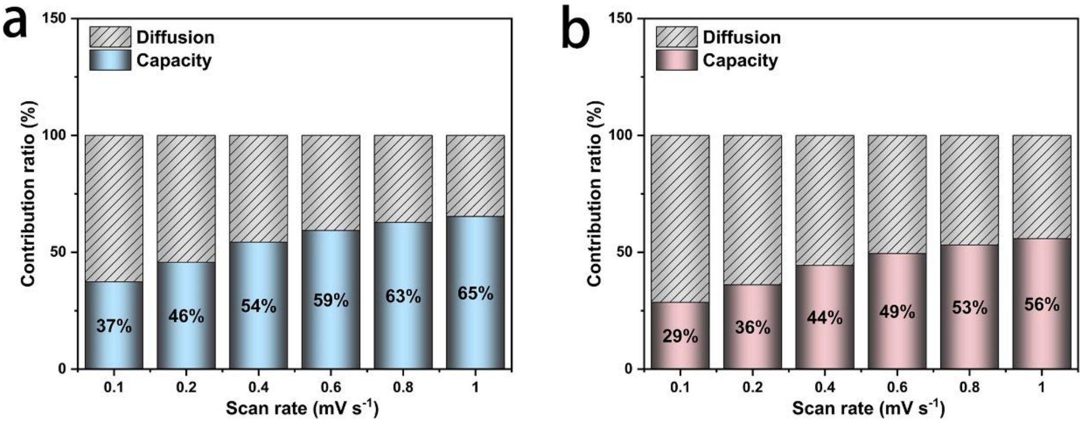

Figure 4.17 The contribution of diffusion-controlled and capacitive-controlled capacities for GeOX/MXene/PVDF (NMP) (a) and GeOX/MXene/Li-PAA (DI-water) (b) at various scan rates from 0.1 to 1 mV s^{-1}.

4.5 Structure Characterization of MXene/GeO$_X$ Electrode

To further investigate the structure of the electrodes when it is using the different binder and solvent **Figure 4.18** displays the SEM image of the electrode with the different binder and solvent. For the GeO$_X$/MXene/PVDF (NMP) electrode, the **Figure 4.18a** and **Figure 4.18b** demonstrate uneven dispersed and agglomeration of materials, lead to the rough and porous structure in the electrode. By contrast, the GeO$_X$/MXene/Li-PAA (DI-water) electrode exhibit smooth and compact structure in electrode, which confirmed the water solvent are indeed improve the compactibility of the structure. Interestingly, this phenomenon does not exist in the GeO$_X$ nanoparticle structure for both of NMP and DI-water solvent (**Figure 4.19**), which confirmed this dispersion difference would only happen on the MXene-based nanosheet structure due to its unique structure and hydrophilic properties. The properties schematics diagram of these two types of electrode were conclude in the **Figure 4.20**.

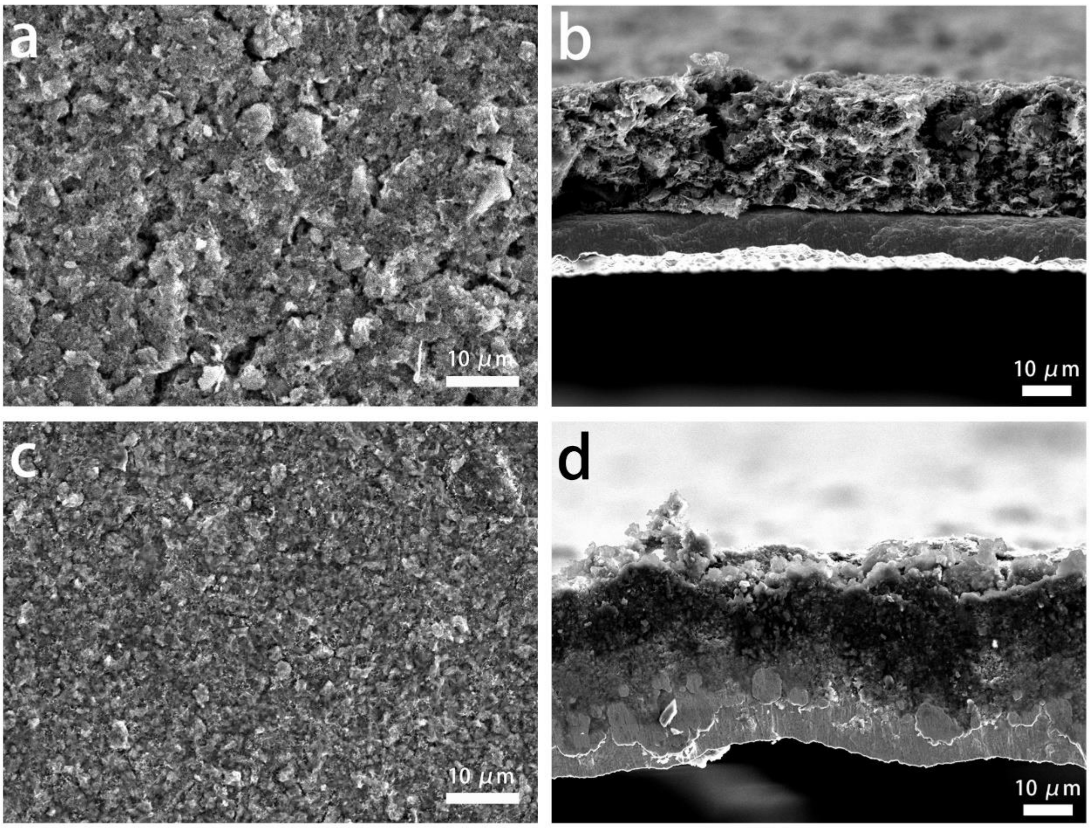

Figure 4.18 SEM images of the GeO_X/MXene electrode. Top-view and cross-section of fresh electrode for GeO_X/MXene/Li-PAA (DI-water) (a and b) and GeO_X/MXene/PVDF (NMP) (c and d).

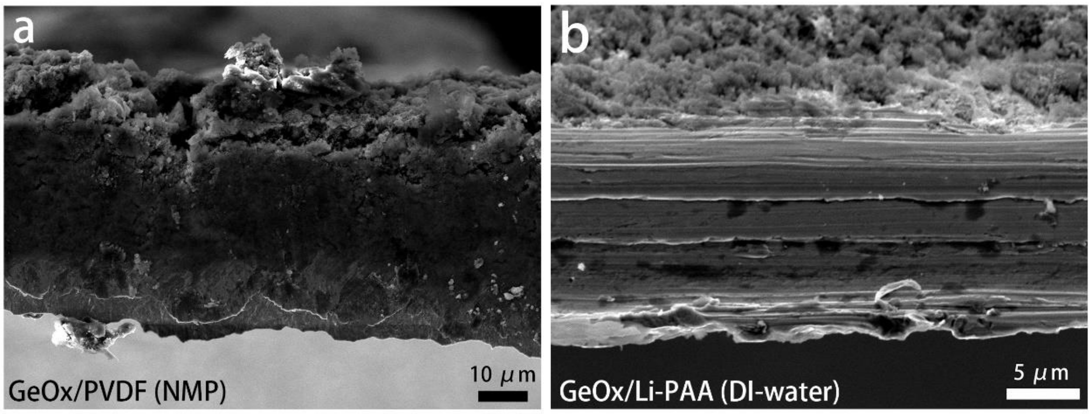

Figure 4.19 Cross-section of fresh electrode for (a) GeO_X/PVDF (NMP) and (b) GeO_X/Li-PAA (DI-water).

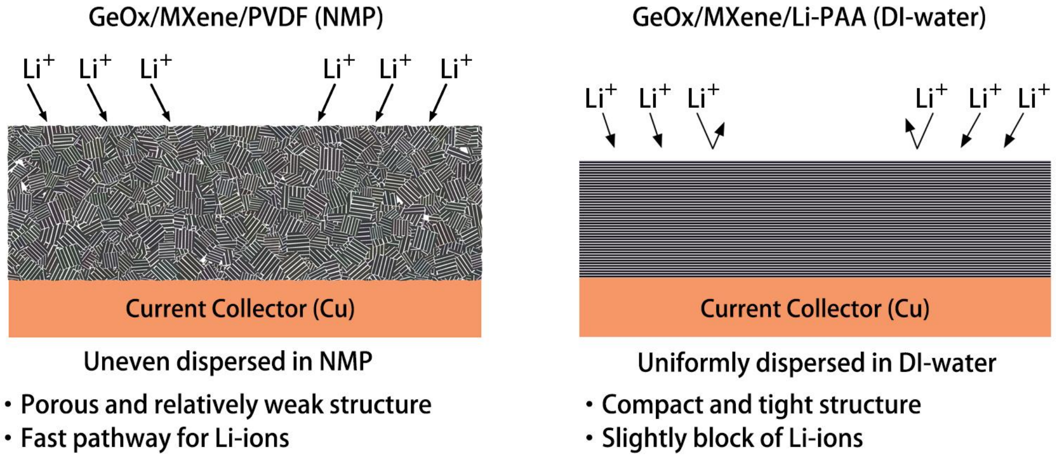

Figure 4.20 Structure schematics diagram of GeO_X/MXene/PVDF (NMP) and GeO_X/MXene/Li-PAA (DI-water).

Figure 4.21c and **Figure 4.21f** show the cross-section of electrodes after 100 cycles to investigate the mechanical stability of the electrode structure. At pristine states, the cross-section of the GeO_X/MXene/PVDF (NMP) and GeO_X/MXene/Li-PAA (DI-water) electrodes showed thickness are 25.64 µm (**Figure 4.21a**) and 20.19 µm (**Figure 4.21c**). However, these electrodes exhibit a drastic difference after 100 cycles. The thickness of the GeO_X/MXene/PVDF (NMP) and GeO_X/MXene/Li-PAA (DI-water) electrode increase to 50.86 µm (**Figure 4.21b**) and 22.48 µm (**Figure 4.21d**), respectively, thereby confirming the well-distributed and compact structure could provide a strict limitation of the volume change of GeOx materials. Overall, the GeO_X/MXene/Li-PAA (DI-water) electrode demonstrates an effective strategy to inhibit the pulverization of the GeO_X materials, which probably inspire the combination of Li-PAA binder and DI-water solvent is more suitable for the composition of alloyed anodes materials with MXene nanosheet in LIBs. But for other materials which does not have the huge volume change during the lithiation, the combination of PVDF binder and NMP solvent seems a better choice. Because it could provide more active sites and fast pathway for Li-ions, further improve the electrochemical kinetics and rate capability in the electrochemical properties.

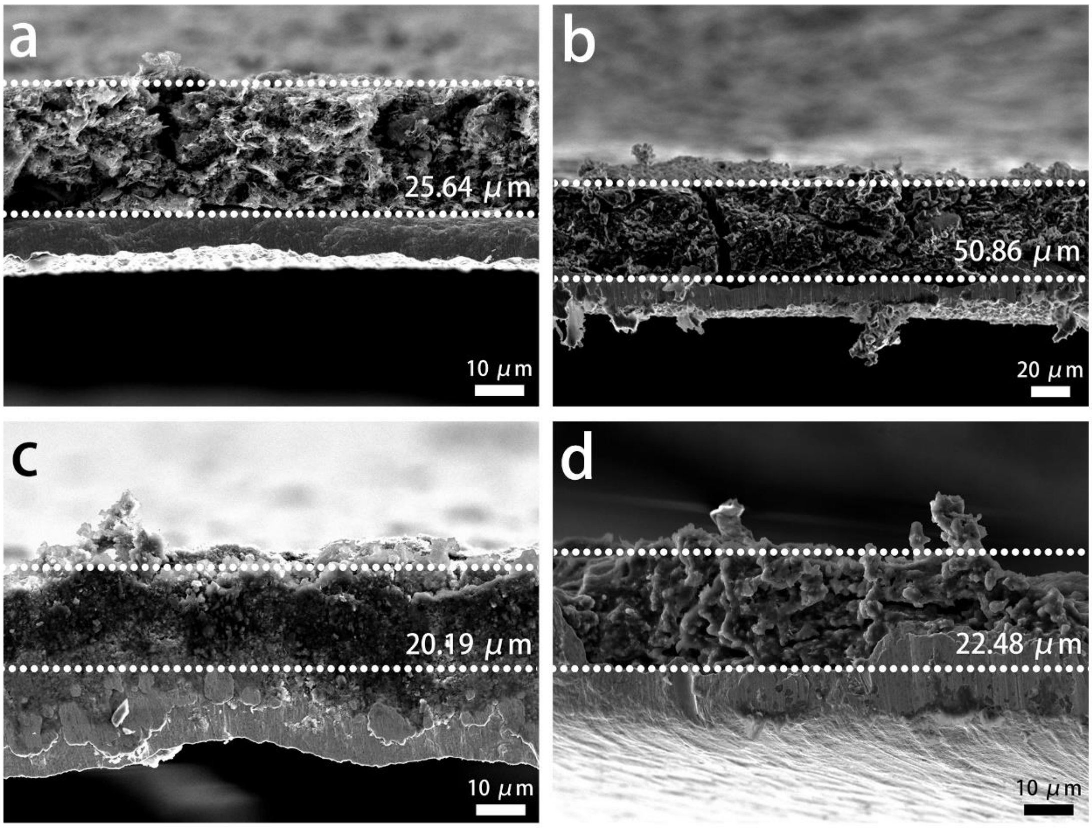

Figure 4.21 Cross-section of fresh electrode for GeO_X/MXene/PVDF (NMP) (a) and GeO_X/MXene/Li-PAA (DI-water) (c); the cross-section of GeO_X/MXene/PVDF (NMP) (b) and GeO_X/MXene/Li-PAA (DI-water) (d) after 100 cycles at the current density of 0.2 A g^{-1}.

4.6 Conclusion

In this study, we have demonstrated a facile one-step approach to fabricate the GeO_x/MXene nanosheet composite, where the amorphous GeO_x nanoparticles were uniformly growth on the MXene nanosheets. This MXene nanosheet and GeO_x nanoparticles significantly enhance the electrical conductivity and Li-ion interaction kinetics in the LIBs. Moreover, we discussed the difference of the electrodes when it prepared by two different combinations of binder and solvent, which demonstrated respective advantages in the different electrochemical properties. For GeO_X/MXene/PVDF (NMP), the electrode exhibited an excellent sustainable capacity of 381 mAh g^{-1} at 15 A g^{-1}. In contrast, the GeO_X/MXene/Li-PAA (DI-water) electrode demonstrates a reversible capacity of 950 mA h g^{-1} at 0.5 A g^{-1} after 100 cycles. To further investigate the reason of these differences, we display the structure and the contribution of diffusion-controlled and capacitive-controlled capacities of these electrodes. The results showed the existence of porous structure in the GeO_X/MXene/PVDF (NMP), which could be ascribed to the uneven dispersion of the GeO_X/MXene nanosheet in the electrode. This porous structure could provide more pathway for Li-ions, but reduce the mechanical strength of the whole electrode. For the GeO_X/MXene/Li-PAA (DI-water) electrode, a compact and tight structure was demonstrated in the SEM image, which provides a robust mechanical strength for the whole electrode, but this tight structure slightly blocks the channel of Li-ions, corresponding to the relatively lower electrochemical kinetics and rate capability.

4.7 References

[1] J. Li, D.-B. Le, P. P. Ferguson, and J. R. Dahn, "Lithium Polyacrylate as a Binder for Tin–cobalt–carbon Negative Electrodes in Lithium-ion Batteries," *Electrochim. Acta,* vol. 55, no. 8, pp. 2991-2995, 2010, doi: 10.1016/j.electacta.2010.01.011.

[2] X. L. Wang, W. Q. Han, H. Chen, J. Bai, T. A. Tyson, X. Q. Yu, X. J. Wang, and X. Q. Yang, "Amorphous hierarchical porous GeO(x) as high-capacity anodes for Li ion batteries with very long cycling life," *J Am Chem Soc,* vol. 133, no. 51, pp. 20692-5, Dec 28 2011, doi: 10.1021/ja208880f.

[3] D. Lv, M. L. Gordin, R. Yi, T. Xu, J. Song, Y.-B. Jiang, D. Choi, and D. Wang, "GeOx/Reduced Graphene Oxide Composite as an Anode for Li-Ion Batteries: Enhanced Capacity via Reversible Utilization of Li(2)O along with Improved Rate Performance," *Advanced Functional Materials,* vol. 24, no. 8, pp. 1059-1066, 2014, doi: 10.1002/adfm.201301882.

[4] C. E. Ren, M.-Q. Zhao, T. Makaryan, J. Halim, M. Boota, S. Kota, B. Anasori, M. W. Barsoum, and Y. Gogotsi, "Porous Two-Dimensional Transition Metal Carbide (MXene) Flakes for High-Performance Li-Ion Storage," *ChemElectroChem,* vol. 3, no. 5, pp. 689-693, 2016, doi: 10.1002/celc.201600059.

[5] Y. T. Liu, P. Zhang, N. Sun, B. Anasori, Q. Z. Zhu, H. Liu, Y. Gogotsi, and B. Xu, "Self-Assembly of Transition Metal Oxide Nanostructures on MXene

Nanosheets for Fast and Stable Lithium Storage," *Adv Mater,* vol. 30, no. 23, p. e1707334, Jun 2018, doi: 10.1002/adma.201707334.

[6] S. H. Choi, K. Y. Jung, and Y. C. Kang, "Amorphous GeOx-Coated Reduced Graphene Oxide Balls with Sandwich Structure for Long-Life Lithium-Ion Batteries," *ACS Appl Mater Interfaces,* vol. 7, no. 25, pp. 13952-9, Jul 1 2015, doi: 10.1021/acsami.5b02846.

[7] N. Sun, C.-l. Peng, J.-c. Zheng, Z.-j. He, H. Tong, L.-b. Tang, C.-s. An, and B. Xiao, "Self-assembled 3D Network GeOx/CNTs Nanocomposite as Anode Material for Li-ion Battery," *Powder Technology,* vol. 338, pp. 211-219, 2018, doi: 10.1016/j.powtec.2018.07.011.

[8] S. Jin, N. Li, H. Cui, and C. Wang, "Growth of the Vertically Aligned Graphene@amorphous GeOx Sandwich Nanoflakes and Excellent Li Storage Properties," *Nano Energy,* vol. 2, no. 6, pp. 1128-1136, 2013, doi: 10.1016/j.nanoen.2013.09.008.

[9] H. Jia, R. Kloepsch, X. He, J. P. Badillo, M. Winter, and T. Placke, "One-step Synthesis of Novel Mesoporous Three-dimensional GeO(2) and Its Lithium Storage Properties," *J. Mater. Chem. A,* vol. 2, no. 41, pp. 17545-17550, 2014, doi: 10.1039/c4ta03933e.

[10] J. s. S. Peña, I. Sandu, O. Joubert, F. S. n. Pascual, C. O. Areán, and T. Brousse, "Electrochemical Reaction Between Lithium and β-Quartz GeO(2)," *Electrochemical and Solid-State Letters,* vol. 7, no. 9, 2004, doi: 10.1149/1.1778931.

[11] X. Zhao, H. Xu, Z. Hui, Y. Sun, C. Yu, J. Xue, R. Zhou, L. Wang, H. Dai, Y. Zhao, J. Yang, J. Zhou, Q. Chen, G. Sun, and W. Huang, "Electrostatically Assembling 2D Nanosheets of MXene and MOF-Derivatives into 3D Hollow Frameworks for Enhanced Lithium Storage," *Small,* p. e1904255, Oct 7 2019, doi: 10.1002/smll.201904255.

[12] H. Li, J. Lang, S. Lei, J. Chen, K. Wang, L. Liu, T. Zhang, W. Liu, and X. Yan, "A High-Performance Sodium-Ion Hybrid Capacitor Constructed by Metal-Organic Framework-Derived Anode and Cathode Materials," *Advanced Functional Materials,* vol. 28, no. 30, 2018, doi: 10.1002/adfm.201800757.

Chapter 5: In-situ Measurement of Stress Evolution and Pulverization in Coin Cell by High-Frequency Capacitance Characterization (HFCC)

In this chapter, we demonstrate a facile equipment to measure the high-frequency capacitance change of the silicon composite electrode. This capacitance change corresponds to the stress evolution and pulverization of the silicon composite electrode due to the structure of coin type LIBs. Because of the limitation of the chemical reaction time during the lithiation/delithiation processes, the coin cell could be simplified to a plane-parallel capacitor by a high-frequency measurement. In this situation, we could use one high-frequency capacitance characterization (HFCC) system to measure the relative change of distance and surface area of two planes, corresponding to the stress and pulverization effect of the electrodes.

5.1 Methodology

5.1.1 The Principle of HFCC System

The principle of HFCC system is utilizing a high-frequency AC source to detect the geometrical capacitance of the coin type batteries. In high-frequency situation, the hypothesis circuit of the coin cell could be considered as a combination of geometrical capacitance and resistance. Alloy anodes exhibited huge volume expanse during the lithiation/delithiation processes, the changes in geometrical capacitance could be ascribed to the stress evolution and pulverization effect. Thereby the variation trend of the stress and pulverization could be determined by the change of geometrical capacitance.

The HFCC system uses a switchable circuit to in-situ measure the capacitance change during the cycling of batteries. The whole system consists of two working modes: charging/discharging mode and measurement mode. The charging/discharging mode consists of an Agilent 3647A DC power supply which could provide an adjustable current to the coin cell and offer a programmable discharge/charge process for the batteries. Concerning the measurement mode, a Hewlett Packard (HP) 4275A multi-frequency LCR meter is employed to measure the capacitance of coin cell with 100 KHz frequency at 50 mV AC amplitude. Furthermore, to switch the circuit connection between the two modes, a switch box acts as an bridge to connect the coin cell with the LCR meter and power supply, which includes two 4-channel 5V DC relay modules. This switching box is also connected with another Agilent 3647A DC power supply to receive the command signal. All equipment could be controlled and programmed by a computer, which plays the role of central bus to give the command, and then collect and process data from the HFCC system. Finally, this system could in-situ measure the capacitance change ever 300s during the cycling process. The data of capacitance versus time could be directly achieved from the computer. At the same time, the voltage versus time curves also could be collected from the DC power supply, corresponding to the charge-discharge curves of the coin cell. The schematic diagram and photo of HFCC system were shown in **Figure 5.1**

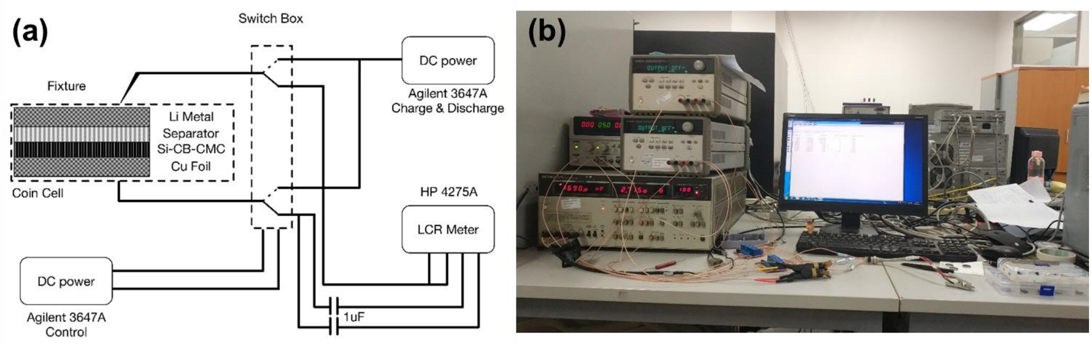

Figure 5.1 Schematic diagram (a) and photo (b) of the HFCC system.

Moreover, As shown in the **Figure 5.1**, we connect a pair of 1 μF capacitor between the coin cells and LCR meter to protect the LCR. According to the handbook of LCR meter (**Figure 5.2**), it is not allowed to directly connect the active device to the auto-balancing impedance measurement equipment.

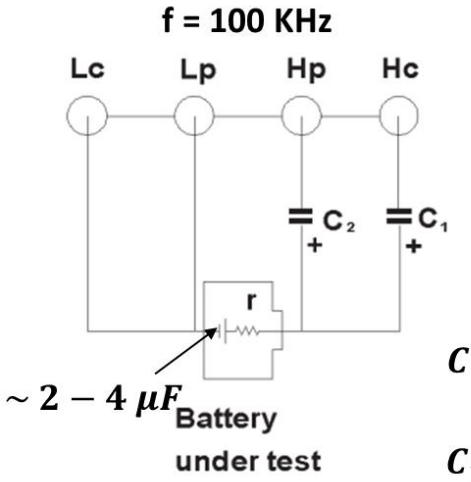

$C_1: \geq \frac{1}{10\pi f}$

(f: Measurement frequency)

C_2: 1 μF

$$C_1 \geq \frac{1}{10\pi f} = \frac{1}{10\pi 100K} = 318.3pF$$

$$C_1 = C_2 = 1\mu F$$

Figure 5.2 Setup of the battery measurement.

To further discuss the changes of capacitance during the lithiation/delithiation processes, the structure of coin type cells was shown in **Figure 5.3**. When the Li-ions are inserted to the silicon anode, the huge stress would occur in the silicon anode then trapped in the coin cell due to its limited space. Then, this stress would release to the polypropylene (PP) or polyethylene (PE) separator, because these polymer separators have lower elastic modulus than the Si electrode. Therefore, the increase of stress inside the coin cell would finally reduce the thickness of separator and further increase the capacitance of whole capacitance. Moreover, the pulverization of Si electrode also leads to the increment of the surface area and further increases the capacitance of the batteries. The change of the capacitance could be simplified to the formula:

$$C = \frac{\varepsilon \times s}{d} \tag{5.1}$$

ε is related to the dielectric constant and s is the surface area of electrode, which is associated with the pulverization of Si electrode. d is the distance between the anode and cathode, corresponding to the thickness of separator, which is mainly influenced by the stress effect.

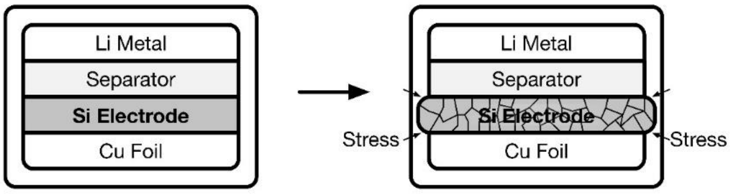

Figure 5.3 Schematic diagram of stress and pulverization effect in coin cell.

5.1.2 Electrode Preparation and Cell Assembly

For the detail of the electrode and battery fabrication, the Si powder (size ~1um, Aladdin) was mixed with carbon Super-P, sodium carboxymethylcellulose (CMC) and polymerized Styrene Butadiene Rubber (SBR) in the mass ratios (68.7:22.9:4.2:4.4) of 2g. A slurry was obtained by mixing the powders with 8ml distilled water for 2.5h. Then, this slurry was coated on the current collector Cu foil (10 um thick) to form the whole electrode by using a gap doctor blade. After that, the film was dried for 2h at 85°C in a vacuum oven to remove the most of water in slurry. The electrode of 13mm diameter was punched out of the dried film. On average, the mass loading of the active materials on electrode was about 1.7 mg cm$^{-2,}$ with the thickness about 18 μm.

The CR2032 coin cells were assembled in an argon-filled glove box (vigor). In this glove box, both oxygen and moisture contexts were controlled to below 1ppm. Lithium metals acted as the counter electrodes. This cell was filled with electrolyte which consists of 1M lithium hexafluorophosphate $LiPF_6$ in EC and DMC with 1:1 vol%.

Moreover, to confirm these capacitance changes that are ascribed to the pulverization and stress effect of the Si anode materials, the Swagelok type cell was employed in this experiment. The main difference between the Swagelok cell and commercial coin cell is a spring inside the Swagelok cell (**Figure 5.4**). This spring eliminated the space limitation of the cell structure and effectively released the stress effect in the cell structure, which ensured that the separator could be shift in the structure to avoid squeezing. By introducing this Swagelok cell structure in the HFCC system, the capacitance changes due to the pulverization probably could be divided from the complex coin cell structure.

Figure 5.4 Structure of Swagelok cell.

5.2 Result

5.2.1 The Verification of the Feasibility in HFCC System

To confirm the feasibility of HFCC system, we firstly tested the microparticles Si anode in the charging/discharging mode of HFCC system and battery test system (BTS) to find out whether they demonstrated a similar lithiation/delithiation processes in the LIBs. The current density for all measurements was adjusted to C/10, where C = 4200 mA g^{-1}.

As shown in **Figure 5.5** and **Figure 5.6**, the time versus voltage curves of the coin cell for the first ten cycles shows a similar result for both of HFCC and BTS, thereby the feasibility of HFCC system is verified. In addition, it is comfirmed that the charging/discharging mode could effectively work for in-situ measurement of the dynamic changes processes during the lithiation/delithiation of the anode.

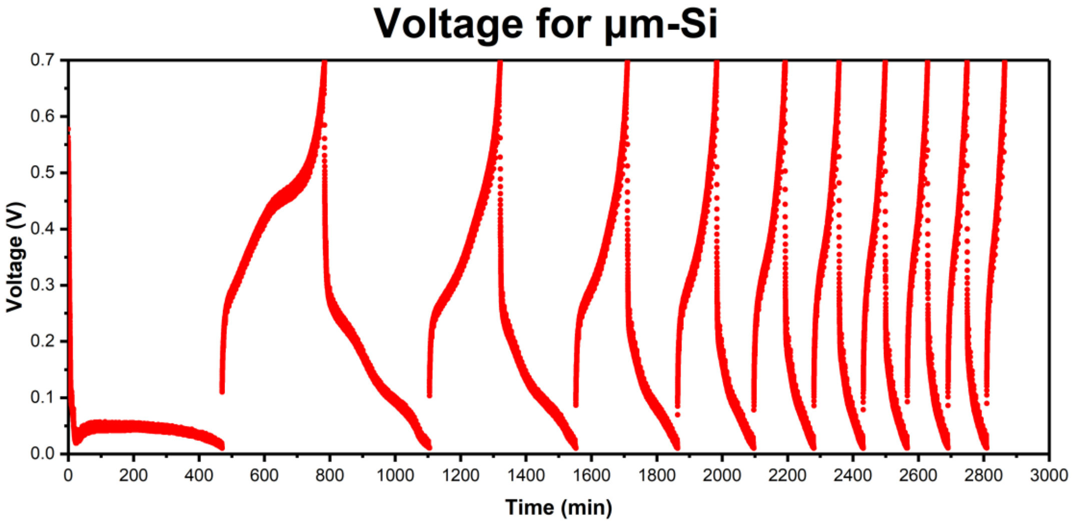

Figure 5.5 Voltage profile of Si microparticles anode in coin cell from HFCC system at the current density of C/10.

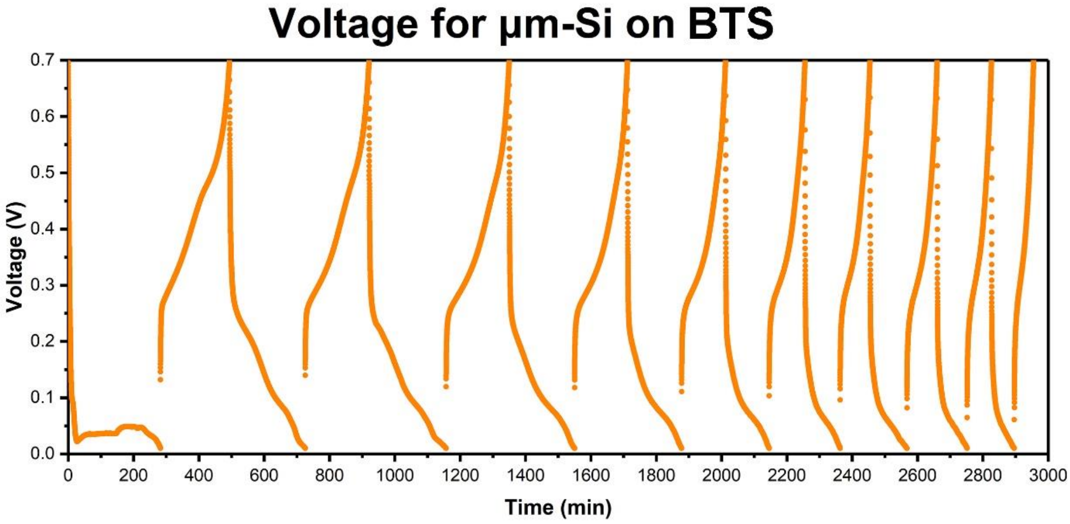

Figure 5.6 Voltage profile of Si microparticles anode in coin cell from BTS at the current density of C/10.

5.2.2 Result of the Si microparticles Anode in Coin Cell

As shown in **Figure 5.7** and **Figure 5.8**, the Si microparticles anode was measure by HFCC system in this section to discuss the stress and pulverization effect of the Si anode in coin cell. The behavior of the capacitance would be introduced in the following part, respectively.

First Discharge/Lithiation:

The read line in the change of capacitance curve displays the change of the capacitance during the lithiation of silicon. In this process, the stress inside the electrode would increase because the Li-ions interact with silicon anode. Due to the space limitation of coin cell, the distance between anode and cathode (d) is therefore decreased. As shown in formula 5.1, the descending of distance would increase the capacitance of coin cell during the first lithiation, which is consistent with the results in **Figure 5.8**.

First Charge/Delithiation:

The blue line in the **Figure 5.8** demonstrates the trend of capacitance during the first delithiation of microparticle silicon anode, corresponding to the dealloying of Li_XSi. That process would release the stress inside the coin cell and increase the distance between electrodes. Moreover, the cracks of electrode was occur in this situation, causing a severe increment of surface area, which means the increment of both s and d probably counteract with each other at the same time. However, according to the formula (5.1), it seems that the change of surface area dominates the capacitance change in the lithiation of silicon, thereby confirms the huge pulverization of the microparticle silicon.

Second Discharge/Lithiation:

In **Figure 5.8**, the yellow line corresponding to the capacitance change is shown in the second discharge step. For the lithiation of silicon anode, the electrode will expand to increase the stress again. At the beginning, the increased stress would lead to a decrease of the distance between the electrodes and further increase the capacitance. However, the expansionof electrode would repair the crack of silicon in the later process of lithiation, thus causing the significant decrease of the surface area and capacitance.

3rd to 5th cycles of batteries:

After the second lithiation of the silicon electrode, the increasing of capacitance during the delithiation and the decreasing of capacitance during the lithiation would simply repeat with further cycling of batteries. This means the dominated factor of these processes is cracks appearing and repairing during the cycling. Moreover, because of the pulverization and capacity fading in silicon anode, the capacitance of electrode shows a decreased trend due to the irreversible produce of the disconnected Li_xSi. The decrease of capacitance could be ascribed to the fading of discharge/charging time in the **Figure 5.7**.

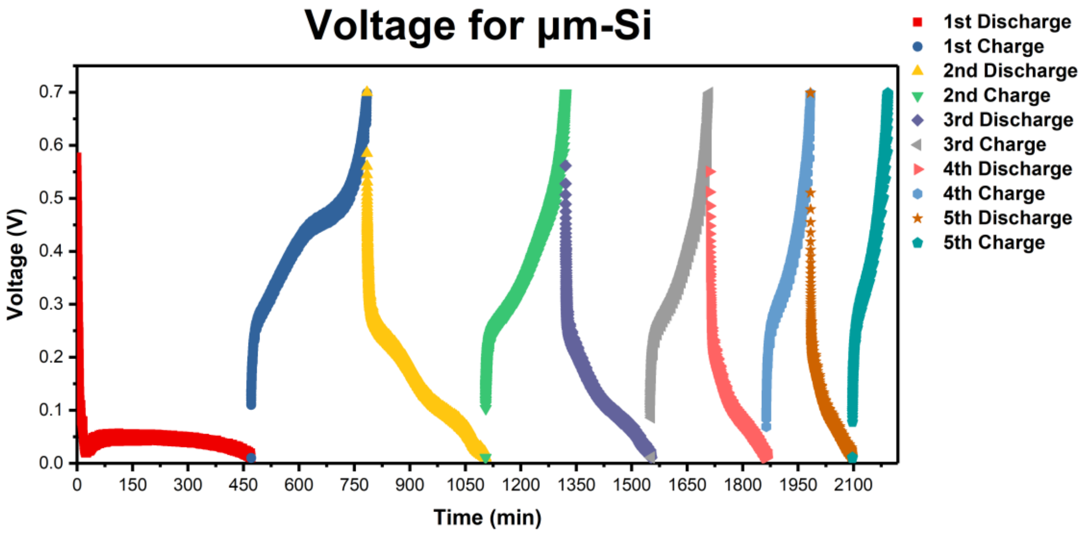

Figure 5.7 The first five voltage profile curves of Si microparticles anode in coin cell from HFCC system at the current density of C/10.

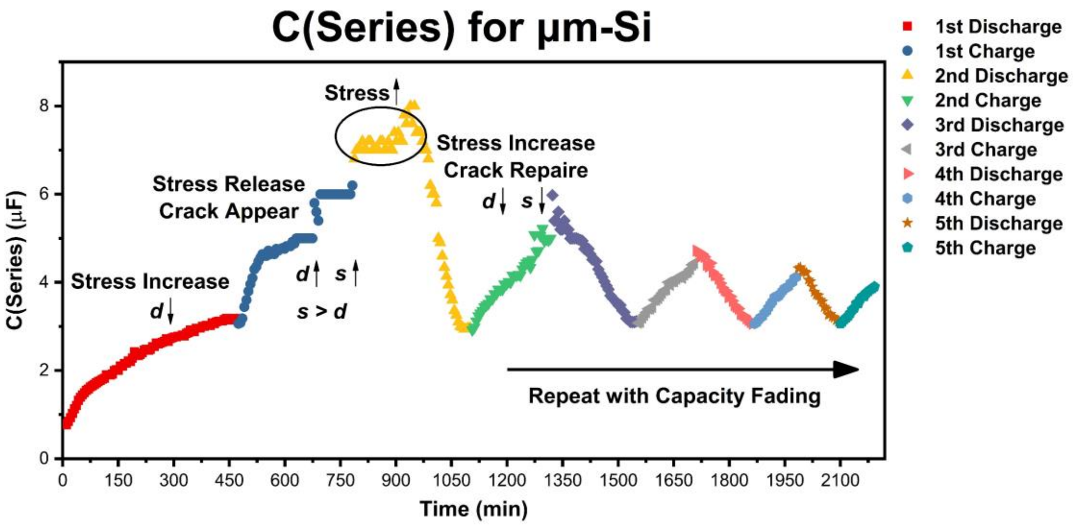

Figure 5.8 The first five capacitance curves of Si microparticles anode in coin cell from HFCC system at the current density of C/10.

5.2.3 Result of the Si microparticles Anode in Swagelok Cell

In order to investigate the effect of stress inside electrode, the Swagelok type cell structure was employed in this section (**Figure 5.9** and **Figure 5.10**). The spring inside the Swagelok cell could release the stress during the lithiation of silicon, mainly demonstrating the capacitance related to the pulverization of electrode, which could help the analysis of cracked and pulverization effect.

First Discharge/Lithiation:

For the first lithiation of silicon anode, when the Li-ion interacts with the silicon, the electrode would exhibit a expansive behavior. However, due to the existing of spring in the Swagelok Cell, the separator would move following the expansion of electrode, resulting in a relatively lower increment of the stress. Thereby, the change of capacitance in the Swagelok is lower than the coin cell, and it only occurs in the beginning of the lithiation process.

First Charge/Delithiation:

Similar to the coin cell with Si microparticles, the capacitance of the first delithiation process demonstrates a rapid increment from the beginning because of the crack of silicon on the electrode. But following with the alloying of silicon, the uncontrolled capacitance growth occur, probably due to the special structure of Swagelok cell. The spring releases the stress inside the cell to further excite pulverization of Si. The deep pulverization causes the severe break of interconnection between the Si particles. These effects not only significantly increase the surface area, but also lead to a rapid capacity fading in the further cycles.

2nd to 5th cycles of batteries:

The further cycles of Swagelok cell are similar to the former coin cell, with the repeat increasing (delithiation) and decreasing (lithiation) of capacitance. The difference is the tendency of capacitance demonstrating a quickly decreasing in Swagelok cell, which confirms the capacitance and capacity fading of this cell is more violent than the coin cell and is consistent with the results from first delithiation process.

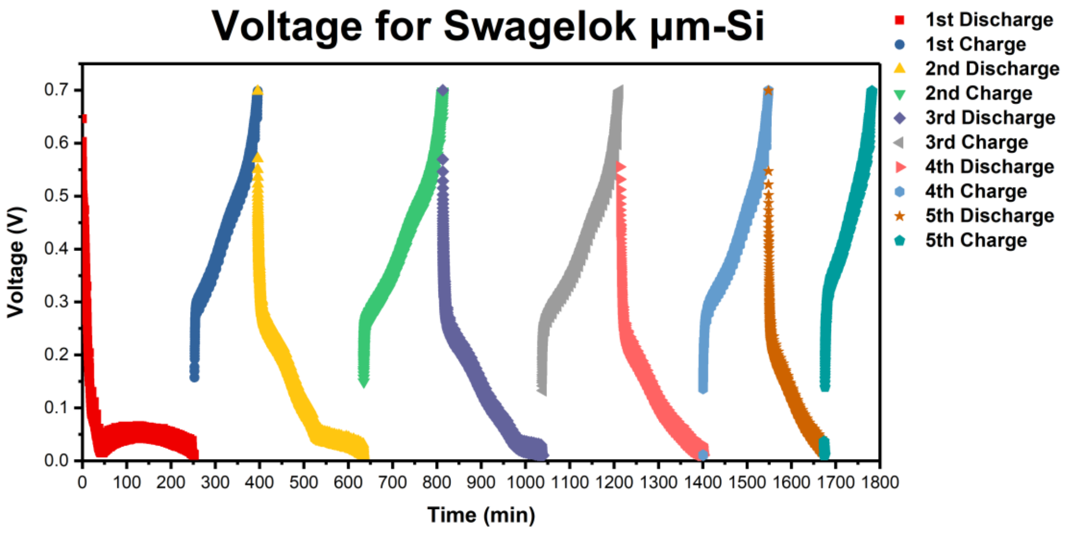

Figure 5.9 The first five voltage profile curves of Si microparticles anode in Swagelok cell from HFCC system at the current density of C/10.

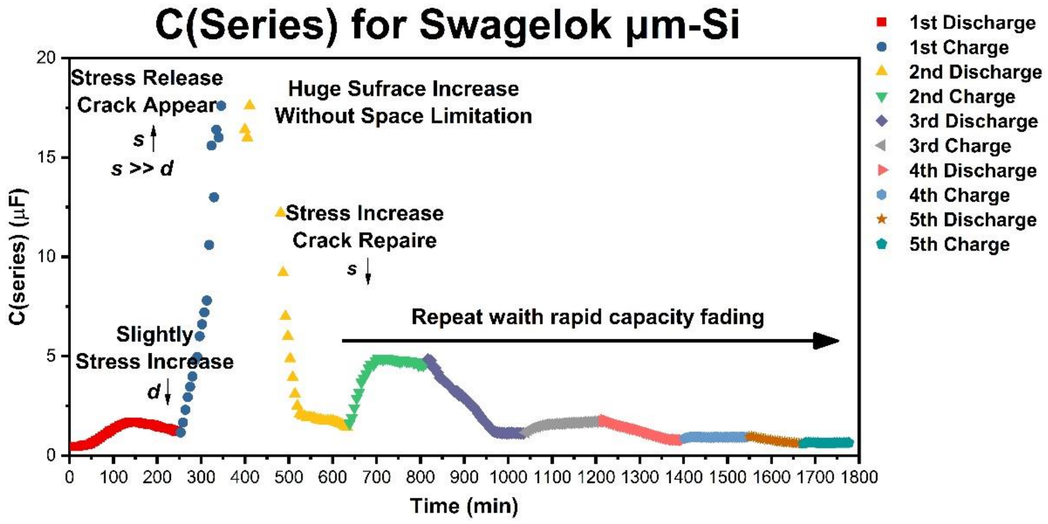

Figure 5.10 The first five capacitance curves of Si microparticles anode in Swagelok cell from HFCC system at the current density of C/10.

5.2.4 Result of the Si nanoparticles Anode in Coin Cell

To further investigate the effect of surface area and stress by HFCC system, the Si nanoparticles were introduced, by which smaller diameter cloud effectively release the stress effect in the electrode (**Figure 5.11** and **Figure 5.12**). These results demonstrate the difference of the capacitance change between the Si nanoparticles and Si microparticles anodes.

First Discharge/Lithiation:

The shape of Si nanoparticles curve in first lithiation step is similar to the coin cell. The capacitance increases with the decline of the distance between two electrodes. The difference is the increment in capacitance of Si nanoparticles is much lower than that of the microparticles Si microparticles owing to the nanosize of Si particles, which could effectively reduce the structure inside the electrode, thereby release the effect of the thickness of separator.

First Charge/Delithiation:

For the first delithiation process, a distinguished difference occurs in the latter part of this period. As shown in formula (5.1), the decline of capacitance is mainly caused by the increase of distance between electrodes in this lithiation situation. That means the Si nanoparticles significantly release the stress effect inside the electrode, which leads to the thickness of separator that dominates the main factor in the change of capacitance. These results further confirm the relatively lower increment of capacitance in the first lithiation curve.

2nd to 5th cycles of batteries:

The capacitance curves in the further cycles also demonstrate a periodic ascending and descending which is similar to the trends of microparticles Si. But the cycle performance of the Si nanoparticle is better than the microparticles Si for both Swagelok cell and coin cell, which demonstrates that the good structure of nanoparticles Si successfully improve the batteries performance in the Si anode.

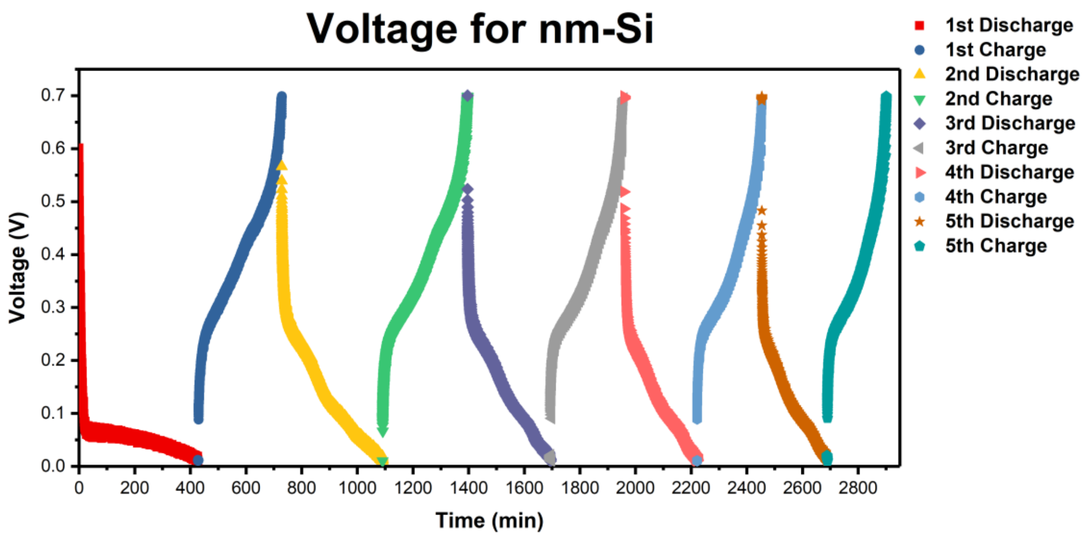

Figure 5.11 The first five voltage profile curves of Si nanoparticles anode in coin cell from HFCC system at the current density of C/10.

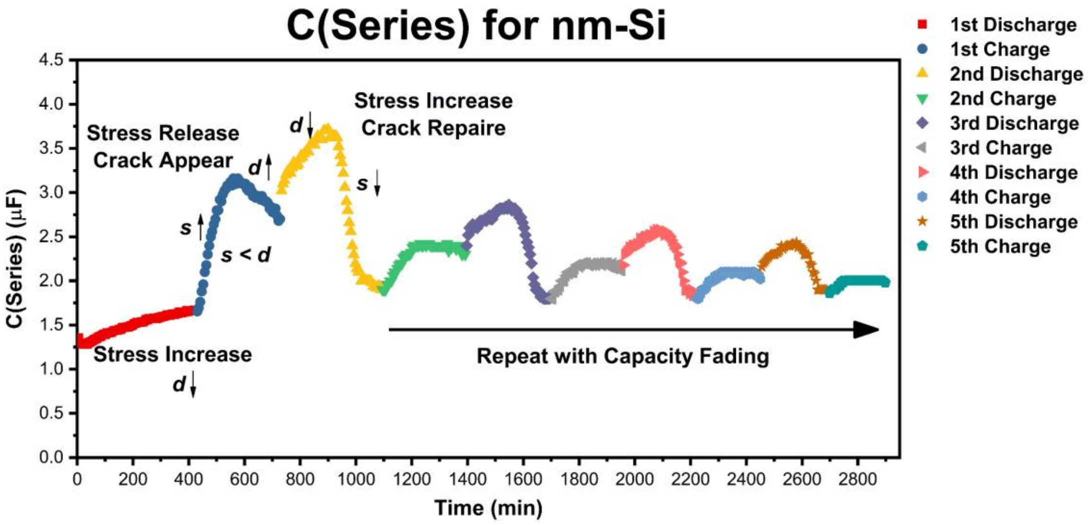

Figure 5.12 The first five capacitance curves of Si nanoparticles anode in coin cell from HFCC system at the current density of C/10.

5.3 Conclusion

In conclusion, the capacitance curves of three different cell were measured by the HFCC system. Both results demonstrated the expected behavior which corresponded to the features of each cell. Moreover, the feasibility of the Swagelok cell and HFCC system were confirmed.

Figure 5.13 display the schematic diagram of stress effect and pulverization for silicon anode during electrochemical cycling. At the first lithiation of silicon, the electrode would expand with a huge volume change, which could cause a large stress inside the coin cell, further pulverize the whole electrode. But the increase of surface area would not occur under this situation due to the space limitation of the coin cell. Contrarily, the thickness of separator would decrease due to the applied stress, as shown in results from Si microparticles in coin cell (**Figure 5.8**). When the delithiation of the silicon happened, the cracks of silicon start to be occurred inside electrode, causing a significant growth of the surface area. Both Si microparticles and Si nanoparticles-based coin cells demonstrated an increasement of the surface area, while Si microparticles-based Swagelok cell exhibited a dramatic increment of that due to the unconstrained space. After that, these cracks would be repaired because the volume of Si was increased again during the second lithiation of the silicon.

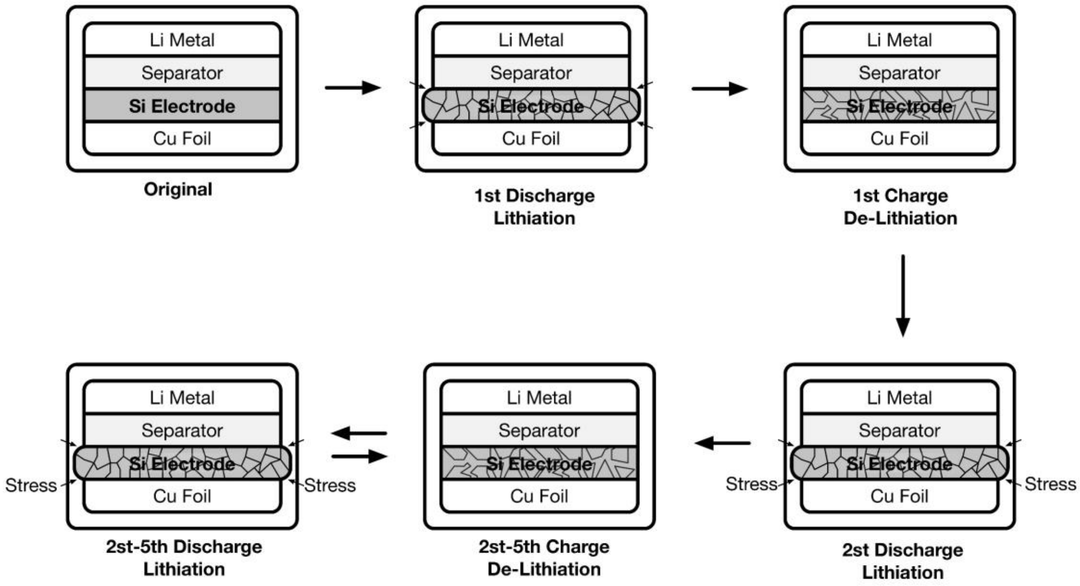

Figure 5.13 The schematic diagram of stress effect and pulverization for silicon anode during electrochemical cycling.

The phenomena of these processes could be further confirmed by the ex-situ SEM image of Si anode in the different states of lithiation and delithiation. In **Figure 5.14**, the surface of electrode becomes rough with the lithiation of silicon, which indicates the huge stress occurs and then squeezes the electrode inside coin cell. These compressive deformations would be relieved with the crack appearing on electrode during the delithiation of Si anode. This experiment confirmed the result of stress and pulverization effect in Si anode from HFCC system.

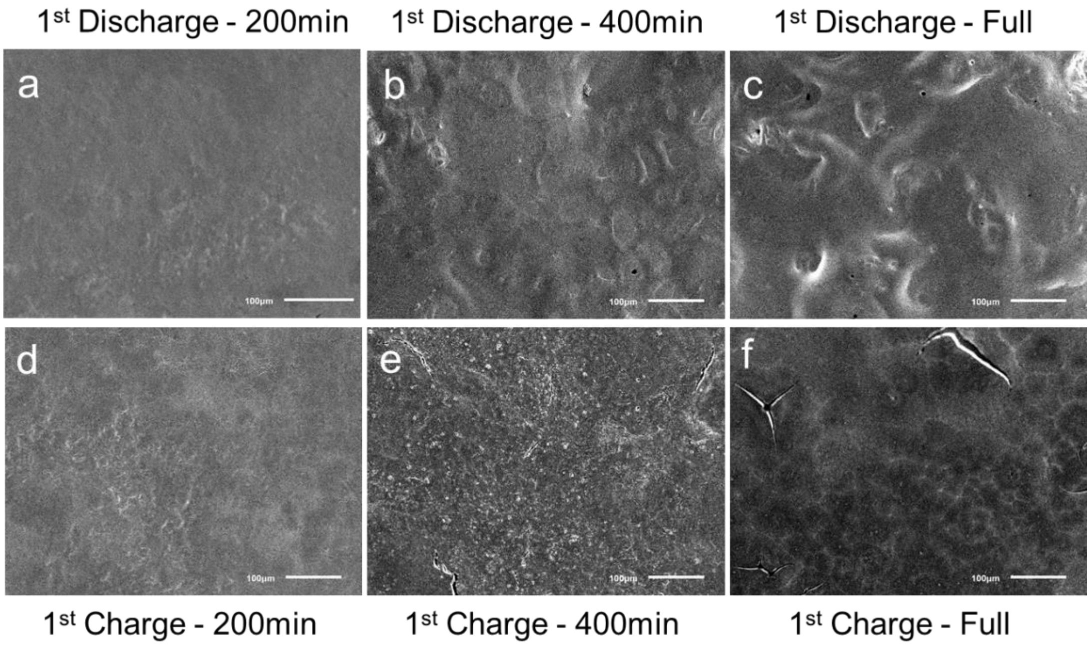

Figure 5.14 SEM images of the electrode surface in the first cycle of charge/discharge for coin cell silicon anode.

Chapter 6: Conclusion and Perspective

In summary, the thesis is mainly focused on the relieve and determinate the stress and pulverization effect of alloy anode in the LIBs. There are three approaches that have been developed to enhance and investigate the electrochemical performance of alloy anode materials. To release the stress effect inside the Si anode materials, a facile method to fabricate a flexible alloyed Cu/Si core-shell nanoflowers (NFs) structure located on three-dimensional graphene foam (3DGF) was demonstrated. This combination provides flexible and free-standing structure and three-dimensional conductive network, allowing unique properties for current collection and transmission. The copper oxide nanoflowers are synthesized on the three-dimensional graphene foam by a simple electrodeposition and etching, which serves as an outstanding template to retard the stress effects during the lithiation/delithiation of silicon. After the silicon coating uniformly deposited on the copper oxide nanoflowers, a simple hydrogen annealing was applied to reduce copper oxide nanoflowers and form the copper/silicon alloy, remarkably enhancing the conductivity of silicon. Moreover, this structure can be directly assembled without any conductive additive or binder. The electrochemical performance of this anode reaches a high capacity of 1869 mAh g^{-1} at 1.6 A g^{-1}, with a high retention rates of 66.6 % after 500 cycles. Even at a high current density of 10 A g^{-1}, this anode exhibits a superior high capacity retention >63% over the 500 cycles (compared with the highest capacity of 679 mAh g^{-1}).

Furthermore, a 2D materials enhanced germanium oxide anode materials has been introduced. By using the GeO_3^{2-} as the precursor, $NaBH_4$ as the reduction agent, a one-pot in situ synthesis of GeO_x nano particles coated MXene nanosheet composite was achieved in Chapter 4. This novel nanostructure not only provides a fast pathway for Li-ions interaction with superior electrical conductivity but also demonstrates a stable electrochemical performance due to the mechanical capacity of MXene. These excellent features result in a good rate performance and stable reversible capacity during lithiation/delithiation cycles. To further investigate the effect of solvent hydrophile in the preparation of slurry, we prepared two different types of electrode. One is prepared with Li-PAA binder and DI-water solvent, another is prepared with PVDF binder and NMP solvent. Two types of electrode demonstrated different electrochemical features, revealed the choice of solvent and binder could significantly influence the electrode properties in the LIBs.

The determination of the pulverization and stress effect was also investigated in this thesis. A high-frequency capacitance characterization (HFCC) system was introduced to in-situ measure the high-frequency capacitance change of silicon composite electrode, which capacitance could be related to the stress evolution and pulverization of silicon composite electrode due to the structure of coin type LIBs. The capacitance curves of three different cell were measured by the HFCC system, both of these results demonstrated the expected behavior which corresponding to the features of each cell. To confirm the validity of the HFCC system, the ex-situ SEM image of Si anode in the different state of lithiation and delithiation processes was performed. The results are consistent with the HFCC system.

Along with the development of the alloying type anode materials in LIBs, the electrochemical performance has been significantly improved because of the employ of advanced technology and materials. The ultimate goal is using these materials to replace the commercial graphite anode and further improve the electrochemical performance of the LIBs. To realize that objective, some issues need to be solved, including the following points: (1) Although creating considerable void space is an effective strategy to accommodate the volume expansion of the anode materials, the formation processes of that are complex and challenging; (2) In many cases, the researchers were focused on the improvement of electrochemical stability by providing numerous void space, which leads to the offered void space exceeds the expanded volume of anode materials. This redundant space distribution further reduces the volume density of the whole electrode; (3) Several experiments involved using the coin cells to assemble the batteries, rather than punch cells or cylindrical cells. The coin cells could exhibit relative electrochemical performance, but it still has some differences with the large batteries, which are common in commercial products. The well-designed composition structure with adjustable void space is a possible solution to these problems. The formation processes of this electrode should be as simple as possible and be able to realize the mass-production in the factory. Moreover, the composition of anode materials not only increases the electrical conductivity of the anode but also reduces the volume expansion for the whole electrode because of the existence of other elements.